Aalto-yliopisto
Aalto-universitetet
Aalto University

Master’s Programme in European Mining, Minerals and Environmental Programme (EMMEP)

Mechanical separation and acid leaching: potential to decrease the environmental impact of the graphite tailings by recovering sulfide sulfur and heavy metals

Case Aitolampi tailings

Sauli Johannes Rytkönen

Master’s Thesis
2022

Aalto-yliopisto
Aalto-universitetet
Aalto University

Author Sauli Johannes Rytkönen

Title of thesis Mechanical separation and acid leaching: potential to decrease the environmental impact of the graphite tailings by recovering sulfide sulfur and heavy metals

Programme Master's Programme in European Mining, Minerals and Environmental Programme (EMMEP)

Major European Mining Course (EMC)

Thesis supervisor Prof. Mari Lundström

Thesis advisor Prof. Simon P. Michaux

Collaborative partner Geological Survey of Finland (GTK)

Date 24.11.2022 **Number of pages** 94 + 11 **Language** English

Abstract

The electrification of the world and the green transition are expected to increase the demand for energy storage technologies such as lithium-ion batteries. This will increase the demand for raw materials used in batteries, such as graphite. Further, due to geopolitical risk and the need for sustainable sources, graphite mining is also of interest in Europe and nations like Finland. During the concentration and/or refining of ore, an enormous amount of waste is produced due to the low concentration of the desired element. Some of the material of interest ends up in these side streams, as for example, in the tailings. However, the waste can potentially be used as a secondary source of raw materials.

In this work the potential processing scenarios of graphite mine tailings were investigated. The studied tailings samples originated from pilot metallurgical test work done in Canada with Aitolampi graphite ore. According to the analysis results, the tailings contain high concentrations of sulfidic sulfur and heavy metals, posing a potential risk of acid mine drainage. In this work, the potential strategies for harmful elements removal were studied and advantages and disadvantages were evaluated. This thesis work included magnetic and gravity separation test work done for tailings samples. Additionally, leaching experiments with varying acid molarity, temperature, and solid-to-liquid ratio were conducted.

Based on the results, with a low-intensity magnetic separator, 58–64% of sulfidic sulfur could be recovered. Additionally, the magnetic product is theoretically suitable to be used in sulfuric acid production. Further, with gravity separation, the grade of Ni, Co, Cu, and Zn could be increased by a ratio of two to three. By leaching experiments, the leaching orders of the sulfide minerals pyrrhotite, sphalerite, chalcopyrite, and pyrite were confirmed. However, the concentrations of Co, Ni, Cu, and Zn in the tailings were too low, and Fe was too high to be economically attractive, so that recovery utilizing only leaching would be economical. This suggests that low grade tailings will still require technological innovations to achieve concentrates suitable for state-of-the-art refining.

Keywords Circular economy, graphite, tailings, sulfur, metal recovery

Aalto-yliopisto
Aalto-universitetet
Aalto University

Tekijä Sauli Johannes Rytkönen

Työn nimi Mekaaninen erottelu ja happoliuotus: mahdollisuus vähentää grafiittirikastusjätteen ympäristövaikutuksia ottamalla talteen sulfidirikkiä ja raskasmetalleja

Koulutusohjelma Master’s Program in European Mining, Minerals and Environmental Programme (EMMEP)

Pääaine European Mining Course (EMC)

Työn valvoja Professori Mari Lundström

Työn ohjaaja Professori Simon P. Michaux

Yhteistyötaho Geologian tutkimuskeskus (GTK)

Päivämäärä 24.11.2022 **Sivumäärä** 94 + 11 **Kieli** englanti

Tiivistelmä

Sähköistyvän maailman ja vihreän siirtymän odotetaan kasvattavan tarvetta energian varastointi menetelmille, kuten litiumioniakuille. Tästä syystä akkujen raaka-aineiden, kuten grafiitin, kysynnän odotetaan kasvavan. Geopoliittisen riskin ja kestävien raaka-ainelähteiden tarpeen vuoksi kiinnostus tehdä kaivostoimintaa Euroopassa ja Suomen kaltaisissa maissa on kasvussa. Malmin rikastamisen ja/tai jalostuksen aikana syntyy valtava määrä jätettä johtuen arvomateriaalien alhaisesta pitoisuudesta. Osa kiinnostavasta materiaalista päätyy sivuvirtoihin, kuten esimerkiksi rikastusjätteeseen. Kiertotalouden periaatteiden mukaan jätettä voidaan kuitenkin pitää sekundäärisenä lähteenä erilaisille raaka-aineille.

Tässä työssä tutkittiin grafiittikaivoksen rikastushiekkajätteen mahdollisia käsittelyprosesseja. Tutkitut näytteen olivat peräisin Aitolammen grafiittiprojektista. Analyysitulosten mukaan rikastushiekka sisältää korkeita pitoisuuksia sulfidirikkiä ja raskasmetalleja, mikä luo riskin happamalle kaivosvalumalle. Tässä työssä tutkittiin mahdollisia strategioita haitallisten alkuaineiden poistamiseksi. Osana työtä rikastusjätteille tehtiin magneetti- ja painovoimaerotuskokeita. Lisäksi suoritettiin liuotuskokeita, missä testattiin hapon molaarisuuden, lämpötilan ja kiintoaine-nestesuhteen vaikutusta.

Tulosten perusteella matalan intensiteetin magneettierottimella sulfidirikistä voidaan ottaa talteen 58–64 %. Lisäksi tämä erotustuote soveltuu teoriassa käytettäväksi rikkihapon tuotantoon. Painovoimaerotuksella voidaan rikastaa nikkelin, koboltin, kuparin ja sinkin pitoisuutta ylijäävästä fraktiosta. Sulfidimineraalien liukenemiskäyttäytyminen vahvistettiin liuotuskokeilla. Kohdemetallien pitoisuuksien todettiin olevan liian alhaisia rikastusjätteissä, jotta pelkkä talteenotto liuottamisella olisi taloudellista. Tämä viittaa siihen, että huonolaatuiset rikastushiekat vaativat edelleen teknisiä innovaatioita huippuluokan jalostukseen sopivien rikasteiden aikaansaamiseksi.

Avainsanat Kiertotalous, grafiitti, rikastushiekka, rikki, metallien talteenotto

Contents

Preface

This master's thesis was completed at the Geological Survey of Finland (GTK) and the Department of Chemical and Metallurgical Engineering at Aalto University's School of Chemical Engineering. This thesis was done for and funded by the BATCircle 2.0 project and GTK. The leaching experiments for this paper were carried out in the Laboratory of Hydrometallurgy and Corrosion (Hydromet) at Aalto University's Department of Chemical and Metallurgical Engineering in the School of Chemical Engineering. Magnetic and gravity separation tests were carried out at GTK Mintec in Outokumpu. The author also likes to acknowledge the collaboration with the Business Finland supported BATCirlce 2.0 project (grant number 44886/31/2020). This research also made use of the RawMatters Infrastructure (RAMI), based at Aalto University and funded by the Academy of Finland.

I want to thank my advisors, Simon Michaux and Mika Sahlman, for their support, guidance, and encouragement. Additionally, I want to thank my supervisor, Mari Lundström, who has always been willing to take time and be available to answer questions.

Tero Korhonen deserves special recognition for the commitment he put into the experimental test work. I also would like to thank GTK and Hydromet personnel for their helpful suggestions and assistance with my work.

This thesis project was the culmination of my studies at Aalto University. During my time here at Otaniemi, I have been able to meet many interesting and great people, which I will always remember. I would like to thank Vuorimieskilta and the people at Rantakahvila and Salt Mines for all the unforgettable experiences.

Finally, I want to thank my family and all my friends for their support. A special thanks to my better half, who has been there for me the whole time.

Glück auf!

Otaniemi, 24 November 2022

Sauli Rytkönen

Abbreviations

AAS	Atomic absorption spectrometry
ABA	Acid base accounting
AMD	Acid mine drainage
ANC	Acid neutralizing capacity
AP	Acid potential
ART_E	Aitolampi rougher tails East
ART_W	Aitolampi rougher tails West
BAM	Battery anode material
CDF	Cumulative distribution
EAF	Electric arc furnace
EC	Electrical conductivity
EDS	Energy dispersive spectroscopy
EU	European Union
EV	Electric vehicle
GFAAS	Graphite furnace atomic absorption spectrometry
GSH	Gravity separation – heavy product
GSL	Gravity separation – light product
GSM	Gravity separation – middling's product
GTK	Geological Survey of Finland
HGMS	High gradient magnetic separator
ICP-AES	Inductively coupled plasma atomic emission spectroscopy
ICP-MS	Inductively coupled plasma mass spectroscopy
ICP-OES	Inductively coupled plasma optical emission spectroscopy
IEA	International Energy Agency
ISO	International Organization for Standardization
LCO	Lithium-cobalt oxide
LFP	Lithium-iron phosphate
LIB	Lithium-ion battery
LIMS	Low intensity magnetic separator
LMO	Lithium-manganese oxide
M1-3	Magnetic product 1-3
MIMS	Medium intensity magnetic separator
MPA	Maximum potential acidity
MRE	Mineral resource estimation
NAF	Non-acid forming
NAG	Net acid generation
NAPP	Net acid production potential
NCA	Lithium-nickel-cobalt-aluminium oxide
NG	Natural graphite
NM1-3	Non-magnetic product 1-3
NMC	Lithium-nickel-manganese cobalt oxide
NNP	Net-neutralization potential
NP	Neutralization potential
NPR	Neutralization potential ratio
PAF	Potentially acid forming

PLS	Pregnant leach solution
PSD	Particle size distribution
SACF	Supreme Administrative Court of Finland
SDS	Sustainable development scenario
SEM-MLA	Scanning electron microscope – mineral liberation analyzer
SG	Synthetic graphite
SHE	Standard hydrogen electrode
STEPS	Stated policies scenario
T	Tesla
TGC	Total graphitic content
TSF	Tailings storage facility
TUKES	Finnish Safety and Chemical Agency
UC	Uncertain acid potential
US	United States
WFD	EU water framework directive
XRD	X-ray diffraction
XRF	X-ray fluorescence

1 Introduction

A rapidly growing population and rising living standards are pushing up raw material demand. Additionally, the electrifying world, including end usages like consumer electronics, energy storage batteries, and renewable energy technologies, requires a wide variety of different metals and minerals. Electrification is usually mentioned together with climate neutrality, where the idea is to achieve net zero greenhouse gas emissions (Aalto, 2021; UN, 2021). According to Aalto (2021), electrification refers to the electrification of energy systems, including production, distribution, and consumption. An example of the energy system would be that electricity is produced with a windmill, the energy is then transferred via powerlines to electric vehicle charging points, where the electric vehicle (EV) is charged, and energy is consumed. Furthermore, electrification takes into account indirect electrification, in which electricity is used to produce, for example, synthetic fuels. Batteries are required because electrical energy must be stored somewhere. As a result, as electrification becomes more dominant in daily life, the demand for batteries is expected to rise (Bogdanov, et al., 2021). The most important electrochemical energy storage systems are lithium-ion batteries (LIB) (Velázquez-Martínez et al., 2019). LIB's basic structure consists of an anode, a cathode, a separator, an electrolyte, and a cell housing. The structure is complex, and materials such as aluminum, copper, carbon, lithium, manganese, and nickel are required depending on the type of LIB (Diekmann et al., 2016; Jiang & Zhang, 2015). The LIBs are discussed in more depth in section 2.1.

Graphite plays an important role in LIBs as an anode material. Graphite also has other applications, such as in refractories and electric arc furnaces (Fernley, 2020). There are two different types of graphite: synthetic and natural, where the latter is obtained through mining. According to Benchmark (2022), demand for lithium-ion batteries is expected to grow six-fold by 2032. Therefore, as a result, just for material demand for LIBs, 6,100,000 tons of natural flake graphite are needed. When this number is converted into mines, almost 100 flake graphite mines with 56,000-ton production per year are needed. There is, however, ongoing research into how to control graphite demand. As an example, graphite can be recycled from end-of-life LIBs (Abdollahifar et al., 2022) and the amount of graphite in LIBs can be decreased using silicon (Elkem, 2018). Further, the use of synthetic graphite influences the total demand for natural graphite.

Globally, a large part of the world's graphite production originates from China, which raises concerns in terms of regional sustainability and geopolitical risk (USGS, 2022). Therefore, end consumers are now focusing on sources in more civilized countries, for example, in Europe (Ritoe et al., 2022). In Finland, both graphite deposits with known grade-tonnage data occur in graphite schist. Furthermore, based on the metamorphism stage of

Finland, there is good potential for additional discoveries of graphite deposits (Törmänen & Tuomela, 2021). Finland also has a strong battery value chain, which includes raw materials, processing knowledge, and a tradition in machine building and ICT technology, all of which add value to an attractive business environment (MEAE, 2021). Different raw materials can be recovered from primary or secondary sources. The use of secondary raw materials is important as in that way the material usage can be maximized, and the amount of waste can be minimized. The secondary sources are usually thought of as recycling of end-of-life products like used batteries, but they also include waste that is created during the processing or manufacturing stages, like mine waste (Sajn et al., 2022).

Any mining operation produces waste. In Finland, for example, the mining industry generated 96 million tons of waste in 2018, accounting for more than 75% of total waste generated in whole country (Vesa, 2021). The generated waste can contain various gangue materials such as sulfide minerals and heavy metals, causing environmental issues such as acid mine drainage (Blowes, et al., 2014; Lottermoser, 2010). The risk, however, can be partially mitigated with a circular economy approach if waste can be valorized in a technologically and economically feasible way to be used as a secondary source of raw materials (EU, 2022; Kinnunen et al., 2022; Lottermoser 2010). Therefore, there is a need to study processing options so that the graphite mine waste can be utilized. In this study, the main challenges in the valorization of the raw material are related to the high sulfidic sulfur and the presence of heavy metals in the tailings. As there are multiple elements present, to limit the scope, the focus is on the recovery of sulfidic sulfur and metals like cobalt, nickel, copper, and zinc.

The possibility of using the tailings, which are produced when natural graphite is removed from the ore, as a secondary supply of raw materials is being investigated using various processing techniques. The used techniques include two mechanical separation methods: magnetic and gravity, which give more insight about the raw material's magnetic and gravity behavior. Additionally, leaching experiments are performed to study the dissolution behavior of metals present in the raw material. Magnetic separation utilizes three different field intensities ranging from low to high: 0.07 T, 0.3 T, and 0.5 T. In gravity separation, the feed is separated into three products using a shaking table: heavy, middling, and light. In leaching experiments, first the effect of the acid molarity is investigated, followed by a set of experiments where temperature and solid to liquid ratio vary. With experiments, the goal is to see if the sulfidic sulfur can be recovered as a saleable product and further utilized. Additionally, the possibility to recover valuable metals at a high enough level to be economically viable is clarified. The environmental impact of graphite mine tailings and the possibility of reducing the impact to a more sustainable level can be illuminated as the environmental impact is also being studied with acid mine drainage tests and by analyzing the total sulfur and carbon. Finally, with leaching experiments, more about the leaching behavior is learned, which can be later utilized.

2 Literature review

A literature review is presented in this chapter. This review is based on journal articles, conference presentations, websites, and private reports. The literature review is divided into the following sections: lithium-ion battery, graphite, the Aitolampi graphite prospect, environmental aspects, and mine waste characterization. The first section introduces the basic components and functionality of the lithium-ion battery, and subsections 2.1.1 and 2.1.2 go into greater detail about the raw materials and their criticality. In the second section and subsections 2.2.1-2.2.6, the focus is put on graphite, its manufacturing processes, the use as a battery raw material and the market situation. In the third section, the site where the studied raw material originates is introduced, and the deposit mineralization and metallurgical aspects are discussed, followed by the concerns related to the project. The fourth section discusses aspects related to mine waste, tailings storage facilities, sulfidic tailings, and the water framework directive. In the final section, mine waste characterization is introduced, including common characterization methods and threshold values for residual elements in extractive waste.

2.1 Lithium-ion battery

Lithium-ion batteries (LIBs) are the most important electrochemical energy storage systems powering wide range of consumer and industrial products. These products include electric vehicles (EVs) which are believed to be part of the solution to mitigate climate change (IEA, 2022; Velázquez-Martínez et al., 2019). The LIB structure is typically comprised of the following components: cathode, anode, electrolyte, separator, and cell housing. Depending on the battery technology, multiple different raw materials, like graphite and different metals, are needed for the LIB structure. The basic layout of the common LIB, the charging/discharging cycle, and examples of cell types are shown in Figure 1. Generally, cell types can be classified into A) cylinder, B) prismatic, and C) pouch cells.

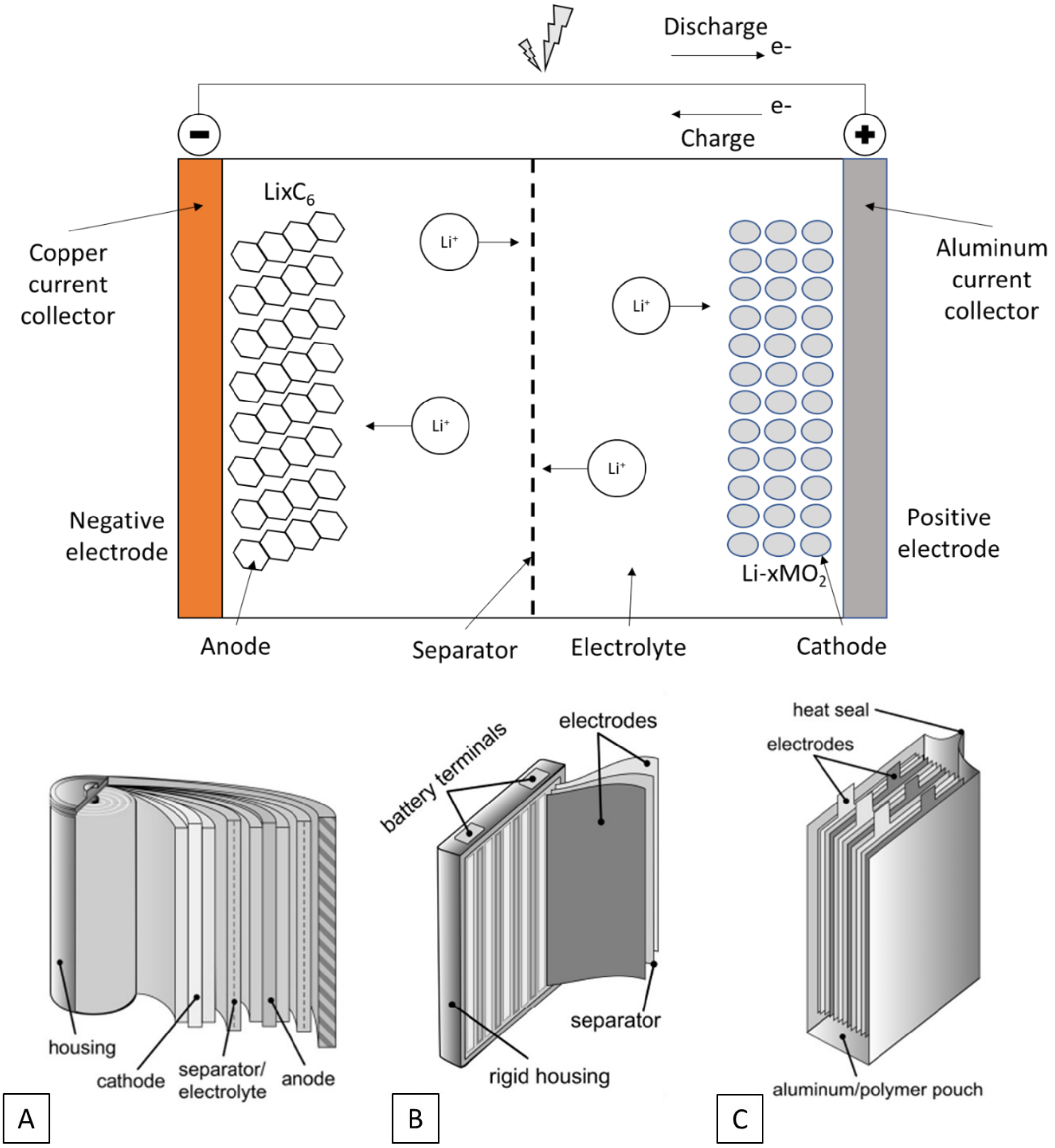

Figure 1. Schematic of LIBs with an overview of the basic components and charging/discharging cycle (based on Samsung SDI, 2022; Kaur & Gates; Jiang & Zhang, 2015). Below are examples of cell types: Cylinder cell (A), Prismatic cell (B), and Pouch cell (C) (Lighting Global, 2019).

In the LIB, an anode and a cathode can store lithium. When LIB is discharged, cell releases electric energy. As shown in Figure 1, lithium-ion (Li^+) is released from the graphite anode, which sets into the cathode, and when LIB is charged, the reverse occurs. To ensure the charging balance, for each Li^+ the same number of free electrons are released. The movement of Li^+ and free electrons occurs trough different routes. While electrons move through current collectors and the external circuit, the electrolyte transports Li^+ between the graphite present on the anode and the metal (Ni, Co, Mn, etc.) rich active material on the cathode trough separator (EERE, 2017; Jiang & Zhang, 2015).

The cathode consists of metal foil, commonly aluminum, which is coated with active material of different intercalation compounds of Li^+ in the form of $Li\text{-}xMO_2$, where M is, for example, Mn, Co, or Ni. The anode also consists of metal foil, commonly copper, that is coated with an anode active material like lithium intercalated graphite (Li_xC_6), titanium disulfide (TiS_2), or vanadium pentoxide (V_2O_5). Metal foils serve as current collectors in an anode and cathode (Kaur & Gates, 2022; Jiang & Zhang, 2015). The electrolyte is made up of lithium-ion salts that are dissolved in an organic carbonate-based solvent. The separator, which separates the anode and cathode, is a porous membrane structure made of synthetic resins such as polyethylene and polypropylene. The structure allows charged ions to flow between electrodes (Samsung SDI, 2022; Jiang & Zhang, 2015). Metals such as aluminum or steel are used for the housing, depending on the application. Furthermore, various polymers can be used (Chombo & Laoonual, 2020).

2.1.1 Raw materials

Both metallic and non-metallic raw materials are used, and a common LIB can contain over 20 different elements. To give some insight into the elemental composition of commercial products, Figure 2 presents the generic composition of an EV battery system, excluding peripherical components (Diekmann, et al., 2016). It should be noted that the information is from 2016, thus it may no longer be a typical composition in terms of cathode active materials, in which Ni content has been significantly increased on average and Co content has been decreased (Buechel et al., 2021).

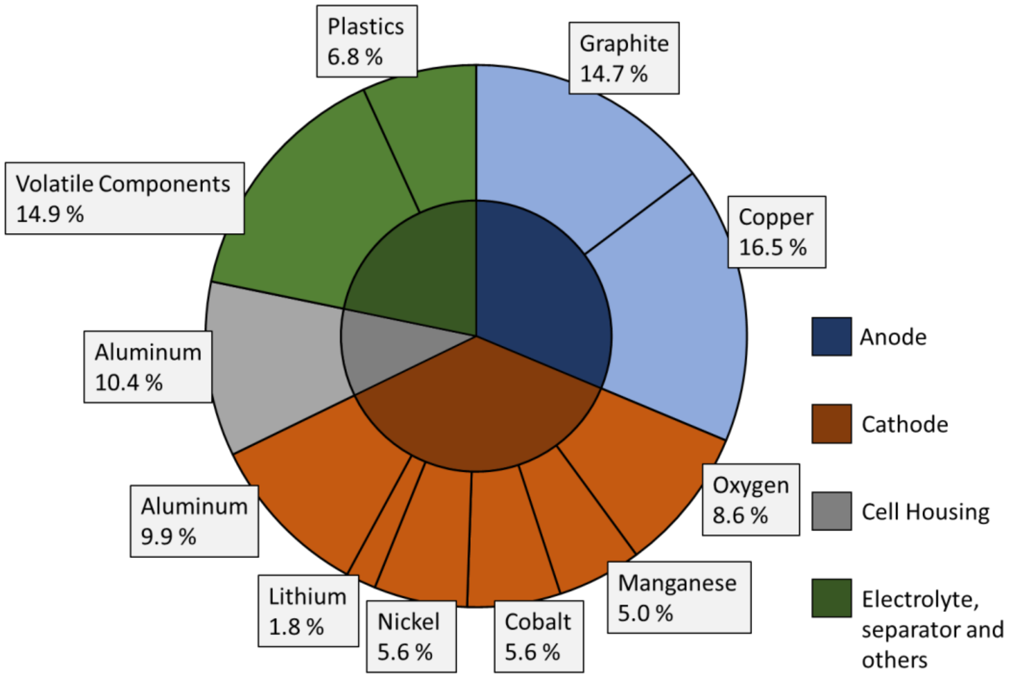

Figure 2. Composition of common EV battery (Modified from Diekmann et al., 2016)

Anodes mainly consist of copper collector foils, which are coated with graphite. On the other hand, the cathode consists of an aluminum collector that is coated with transition metal oxide, such as lithium-nickel-cobalt-manganese oxide, as shown in Figure 2 (Diekmann, et al., 2016). There are different transition metal oxides used as cathode materials depending on the battery technology, in which the chemical composition varies as presented in Table 1.

Table 1. Cathode technologies (Zhang et al., 2021)

Cathode	**Combination**
LCO	$LiCoO_2$
LFP	$LiFePO_4$
LMO	$LiMn_2O_4$
NMC	$LiNi_{1-y-z}Co_yMn_zO_2$
NCA	$LiNi_{1-y-z}Co_yAl_zO_2$

These cathode technologies (see Table 1) have suitable qualities in different fields, such as high-volumetric-capacity Lithium-Cobalt Oxide (LCO), cheap Lithium-Manganese Oxide (LMO), stable Lithium-Iron Phosphate (LFP) and high-capacity Lithium-Nickel-Manganese-Cobalt Oxide (NMC) and Lithium-Nickel-Cobalt-Aluminum Oxide (NCA) (Zhang et al., 2021). Currently, the focus is on increasing the Ni content of NMC and NCA since higher nickel content allows higher energy density while costs are reduced, as Ni replaces Co. Furthermore, reliance on Co is reduced, which is important from an ethic point of view (Rudisuela, 2020). When it comes to the anode material and its electrochemical performance, graphite has been proven to be the best option, and therefore it dominates the markets with a 98% share, leaving lithium titanate (LTO) 2% share (Zhang et al., 2021). Other suggested candidates have been silicon (Si), silicon oxide (SiO_x), lithium metal, sulfides, and oxides. Currently, the SiO_x and Si-graphite composite anode materials can be found in commercial products, though research is continuing (Su et al., 2022; Andersen et al., 2019). As the technology as well as chemical composition varies, different amounts of materials are required. Table 2 compares the material intensity in kilograms of material per kilowatt-hour of energy storage (kg/kWh) of various cathode technologies for lithium, nickel, cobalt, manganese, and aluminum. Different subtypes of NMC are presented as a number following 'NMC', representing the ratio of Ni:Mn:Co (Leader & Gausta, 2019).

Table 2. The material intensity of cathode technologies in kg/kWh (Leader & Gausta, 2019; Yugo & Soler, 2019)

Material intensities in kg/kWh							
Element	**LCO**	**LFP**	**LMO**	**NCA**	**NMC (111)**	**NMC (622)**	**NMC (811)**
Li	0.1- 0.15	0.1	0.05 - 0.15	0.05 - 0.15	0.1 - 0.15	0.1 - 0.15	0.1 - 0.15
Ni	0	0	0	0.45 - 0.75	0.2 - 0.4	0.4 - 0.7	0.45 - 0.75
Co	0.7 - 1.2	0	0	0.1 - 0.15	0.2 - 0.4	0.12 - 0.2	0.1
Mn	0	0	1 - 1.2	0	0.2 - 0.4	0.12 - 0.2	0.1
Al	0	0	0	0.05	0	0	0

As the anode is mostly graphite and coated copper foil, the material intensities of both elements are quite constant between different LIB types. For graphite, the estimated material intensity is about 1–1.2 kg/kWh and for copper, about 1.1–1.2 kg/kWh (Oxford Analytica, 2021; NMG, 2021; International Copper Association, 2017).

2.1.2 Material criticality in future

According to the International Energy Agency (2021), the global clean energy transition will cause a massive spike in demand for minerals over the next 20 years. The rate of demand is strictly connected to the overall price of raw materials. Furthermore, higher mineral prices may have an impact on the achievement of industry cost targets, which may have an impact on clean energy adoption rates. For example, in batteries, raw materials currently account for 50 to 70% of total costs. Cathode (25-30%) and anode (8-12%) materials represent the largest share of the material costs (IEA, 2021). The IEA (2021) has estimated material demand based on two different scenarios: the Stated Policies Scenario (STEPS) and the Sustainable Development Scenario (SDS). The main difference between the scenarios is that in SDS, all current net zero pledges are estimated to be achieved in full, while STEPS examines what must be put in place to achieve energy-related goals at a more granular, sector-by-sector level. Compared to 2020, in 2040 the total mineral demand from clean energy technologies doubles in the STEPS and quadruples in the SDS scenario. The growth in Li, graphite, Co, Ni, and Mn demand is shown in Figure 3. The growth is shown as an index number, where the 2020 level is the base level of one.

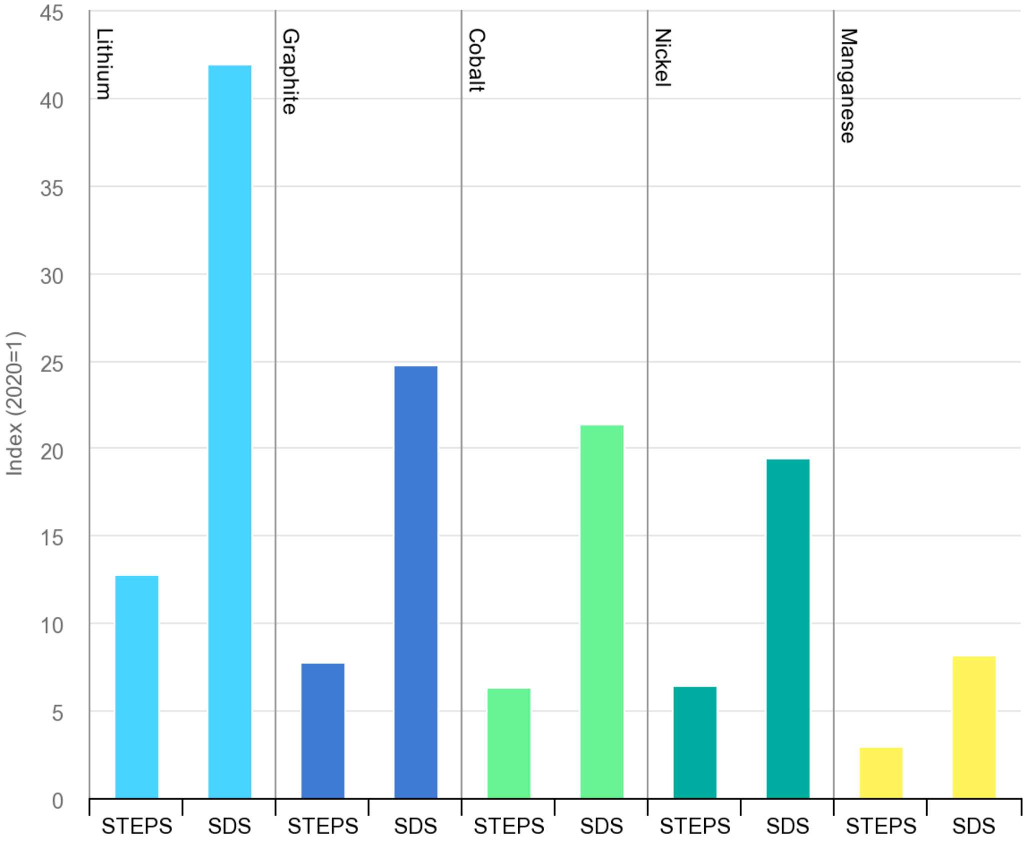

Figure 3. The growth in Li, graphite, Co, Ni, and Mn demand in 2040 relative to 2020 (IEA, 2021)

As shown in Figure 3, the demand for lithium is expected to increase the most. Graphite, cobalt, and nickel increases are quite similar, between 20 and 25, while manganese is expected to increase the least. Xu et al. (2020) made in their study some estimations for Li, graphite, Co, Ni, and Mn based on SDS and STEPS scenarios between 2020 and 2050. Based on their results, in the case of STEPS, Li demand would rise by a factor of 17–21, graphite by a factor of 6–17, Co by a factor of 7–17, Ni by a factor of 11–28, and Mn by a factor of 7–18. When it comes to the SDS scenario, the corresponding values were approximately 1.7–2 times higher. The total material demand from new EV sales by scenario is shown in Figure 4. The demand of mineral is presented in kilotons (kt) for year 2020, 2030 and 2040.

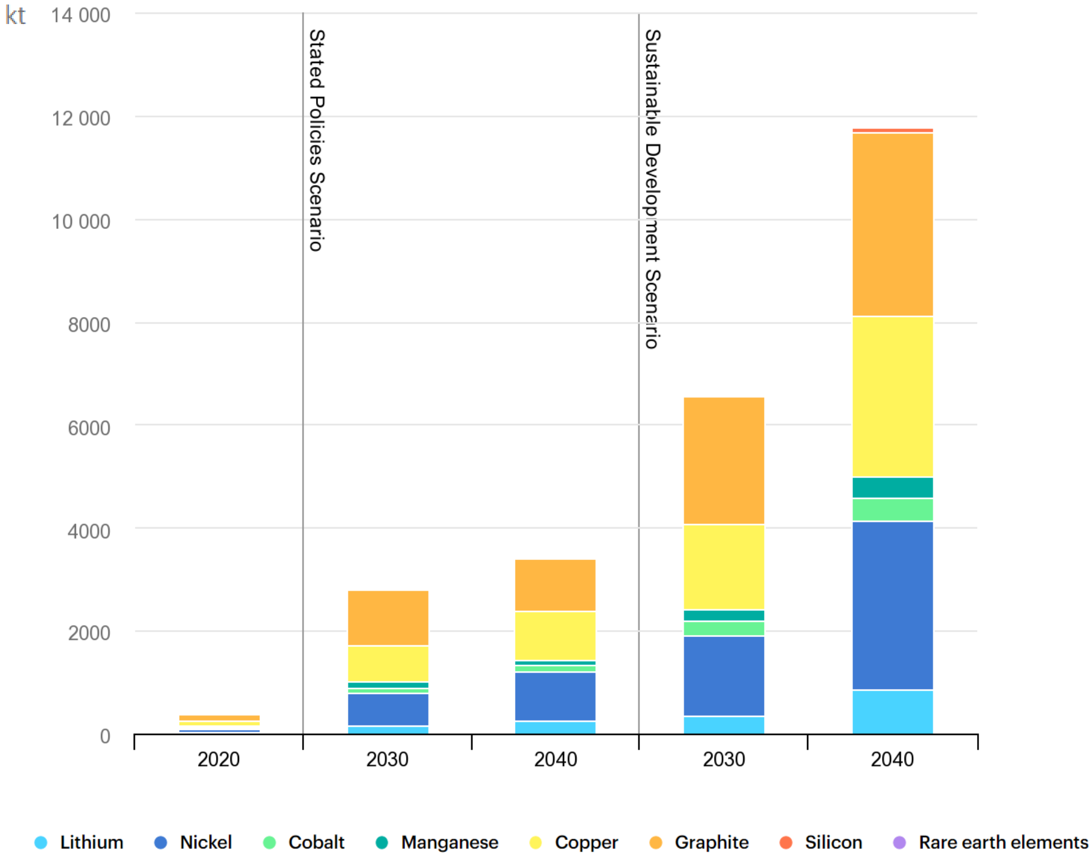

Figure 4. Total material demand from new EV sales in kilotons between 2020 and 2040 (IEA, 2021)

As shown in Figure 4, the demand is highest for graphite, copper, and nickel. Lithium is expected to have the fastest growth rate, and the demand for cobalt is expected to be mitigated by using higher nickel content battery chemistries (IEA, 2021). Xu et al. (2020) predicted that in 2050, the STEPS scenario's demand for Li, Co, and Ni could range from 620 to 770 kt, 250 to 620 kt, and 150 to 370 kt, respectively. When it comes to copper, graphite, and silicon, the corresponding values were estimated to be 150–400 kt, 170–450 kt, and 1800–5000 kt, respectively. In the case of SDS, the demand was predicted to be 1.7–2 times higher. As shown, there is some variation between the estimates. This is primarily due to the development of EV fleets and their battery capacity requirements, which affect favorable cell chemistries. Furthermore, closed loop recycling and EV and battery re-use will play an important role in reducing future primary material demand (Xu et al., 2021).

The increasing demand is going hand-in-hand with the criticality of raw materials and the simultaneous risk of supply to the EU to sustain Europe's economic and environmental ambitions (European Commission, 2021). According to Abdelbaky et al. (2022), cobalt is extremely critical as a major part is exported from the Republic of Congo, which imposes risk for export restrictions and therefore supply for the EU. Additionally, 95% of global cobalt is produced as a by-product of copper and nickel ore, from which 70% is produced as a by-product of African copper production (van den Brink et al., 2020). In case of lithium, there is a high risk in EU raw material supply, as most of the mining is concentrated in Australia, Chile, and China. Further, graphite and silicon pose similar risk because over 60% of both are produced in China (Xu et al., 2020). Steel production uses manganese, which drives up demand as a competing end-use industry. Similar circumstances apply to nickel, where the global steel sector utilizes approximately 73% of total mine output compared to the battery sector's 8% share (Abdelbaky, 2022; Lennon, 2021). It should also be noted that there are no exciting substitutes for lithium, nickel, and manganese used in LIBs, so those are still needed in the future, compared to cobalt, whose content can be decreased in batteries (Abdelbaky, 2022; Rudisuela, 2020).

2.2 Graphite

There are two different types of graphite: natural (NG) and synthetic (SG). In the future, there may also be recycled secondary sources for graphite; however, this is not currently industrial state-of-the-art. Due to graphite’s unique properties, including high electrical and thermal conductivity, it plays a major role in the electrifying world, especially as an anode material in LIBs (Zhao et al., 2022). Typical industrial uses of graphite are, for example, anodes, refractories, electric arc furnaces (EAF), casting molds, foundries, lubricants, nuclear reactors, and pencils (Mordor Intelligence, 2022; Michaux, 2019).

2.2.1 Natural graphite

NG is mined from deposits in metamorphic rocks such as marble, schist, and gneiss, as well as vein deposits. NG is formed from carbon-rich organics under long-term high temperature and pressure geological environments in sedimentary rocks (Zhao et al., 2022; Robinson Jr., Hammarstrom, & Olson, 2017). Commercial deposits occur in three different geologic categories: amorphous, flake, and lump/vein.

Amorphous graphite is a commercial term for earthy to compact fine-grained graphite that is typically formed during thermal metamorphism of coal seams. Amorphous graphite varies in size from 75 to 110 micrometer (μm) (Fahl, 2017; Taylor, 2006). Commercial deposits typically contain over a million metric tons of ore with a carbon grade of up to 75%. Amorphous graphite can be used to produce lubricants (Robinson Jr., Hammarstrom, & Olson, 2017).

Flake graphite is the commercial classification for well-developed crystal platelets with sizes between 40 μm and 4 centimeters (cm). These platelets are disseminated in beds of carbonaceous sediments and have been subjected to amphibolite-facies or higher-grade regional metamorphism. Commercial deposits typically contain over 200,000 tons of ore with a grade of more than 8%, although lower grade deposits are also known. This type of deposit can be found in belts of crystalline metamorphic rock from the Archean or late Proterozoic age. The flake graphite is classified into four different sizes, which are jumbo (>300 µm), large (180—300 µm), medium (150—180 µm), and fine (<150 µm). Flake graphite is used, for example, in the battery and refractory industries (INN, 2021; Robinson Jr., Hammarstrom, & Olson, 2017).

Lump or chip graphite, also known as vein graphite, is the commercial classification for interlocking aggregates of rough graphite crystals located in veins of fractures in igneous and crystalline metamorphic rocks from the Precambrian age. The vein graphite chip size can be larger than 300 µm and have over 90% carbon content. This type of deposit is rare, and only commercial mines operate in Sri Lanka and Mexico, though there is no reliable data on the tonnages available. Vein graphite is used in lubricants (Robinson Jr., Hammarstrom, & Olson, 2017; Taylor, 2006).

Because each deposit is unique in size and shape, different mining methods are used. Flake graphite is commonly found in deposits near the surface, and depending on the degree of weathering, it can be mined using either hard-rock or soft-rock mining techniques. Amorphous graphite is extracted using methods similar to those used in coal mining. Vein graphite can be extracted using open-pit or traditional shaft mining techniques. (Damm & Zhou, 2020).

2.2.2 Processing of natural graphite

Beneficiation and refining processes can include multiple different stages. However, only the most common techniques are discussed in this thesis. The techniques and processing set-ups vary depending on the deposit, flake size distribution, and specifications set for the final concentrate (e.g., crystallinity, texture, ash content, and level of impurities). The main idea of the processing is to upgrade the ore by getting rid of the gangue minerals and other impurities. In this thesis, beneficiation refers to the improvement of physical and chemical properties in preparation for the refining stage, wherein the residual impurities are removed. Based on this, the following beneficiation and refining methods are discussed, shown in Figure 5 (Damm & Zhou, 2020; Jara et al., 2019). It should be noted that the methods are unit processes, and the overall process may contain various processes in varying orders.

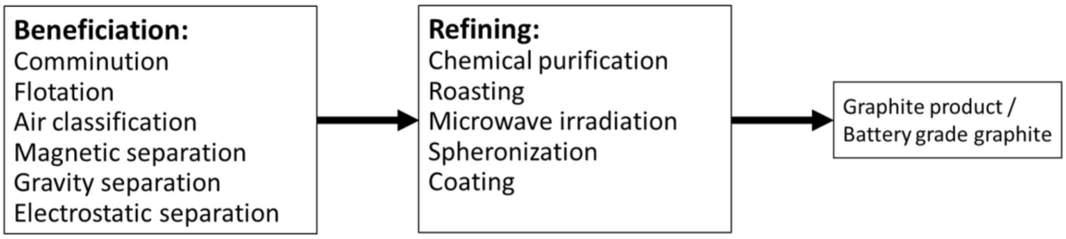

Figure 5. Beneficiation and refining stages of natural graphite

The comminution, which can include unit processes like crushing, milling, grinding, cutting, and vibrating screening, reduces the ore size to smaller and finer particles. The most important goals of comminution are the liberation of valuable minerals and the exposure of more surface area, which is beneficial in subsequent process steps such as leaching. Additionally, the reduction in size eases processing and handling, and market requirements for particle size specifications can be achieved (Jara et al., 2019).

Froth flotation can be used to concentrate graphite from the slurry body which is a by-product of the comminution step. Froth flotation is a selective method where hydrophobic minerals are separated from hydrophilic minerals in a water suspension. As the graphite is naturally hydrophobic, it attaches air bubbles and is moved to the top of the flotation cell where the concentrate can be recovered (Jara et al., 2019). Based on the flotation studies and industrial data, a graphite concentrate grade of 50–90% can be achieved with flotation, depending on the feed grade (Al-Ani et al., 2020; Robinson Jr. et al., 2017; Fahl, 2017; Florena, et al., 2016).

Air classification is a separation technique where different particles are separated based on their density, shape, and aerodynamic properties. With this unique operation, it is possible to separate the graphite from gangue minerals, utilizing the graphite's low density and flaky structure. In addition, the separation can be done between different sized graphite flakes. Air classification can be performed after the initial crushing stages (Volt Carbon Technologies, 2022; Jara et al., 2019). An example of air classification is a cyclone.

Magnetic separation is based on the different magnetic properties of minerals present in the feed. All minerals have one of the three magnetic properties, which are ferromagnetic (magnetite, pyrrhotite, etc.), paramagnetic (ilmenite, rutile, chromite, etc.) and diamagnetic (plagioclase, calcite, apatite, etc.) (Haldar, 2013). There are various separator types where the feedstock can be either wet or dry. For example, as pyrrhotite is ferromagnetic, it is attracted to magnets and can be separated from the stock feed, while graphite is not affected or is less affected by the magnetic field (Haldar, 2013).

Gravity separation is based on each mineral's unique relative density. In feed, there can be multiple different minerals present, and based on the densities, it is possible to separate the light minerals from the heavy ones. Gravity separation equipment comes in different forms, including spirals, shaking tables, and hydraulic classifiers (Metso, 2011). There can be light, medium, and heavy products, depending on the machine's capacity. For instance, pyrrhotite can be recovered into different products than graphite, which relative density is 2.3, because pyrrhotite's relative density is 4.6 (Mindat, 2022). In the graphite industry, gravity separation is used, for example, in Sri Lanka, where it is done for underflow from flotation to increase the graphite recovery (Ulukkulama et al., 2018).

Electrostatic separation is a processing method where a mixture of particles can be separated utilizing electrical forces on charged or polarized particles. Therefore, since every mineral's response to the electrical charge varies, it is possible to separate the feed material into different output fractions (Jara et al., 2019). This method is used more in the coal industry to improve the quality of coal (Liu & Wang, 2021). However, it could be a suitable method that could also be used for graphite beneficiation.

Figure 6 illustrates an example of a flowsheet for the beneficiation process for natural graphite at a mine site (Damm & Zhou, 2020), including beneficiation methods like comminution and flotation, shown in Figure 5. Typically, the product of the beneficiation process is graphite concentrate, which is then sorted and bagged based on flake size. The bagged product continues to the refining stage (see Figure 5).

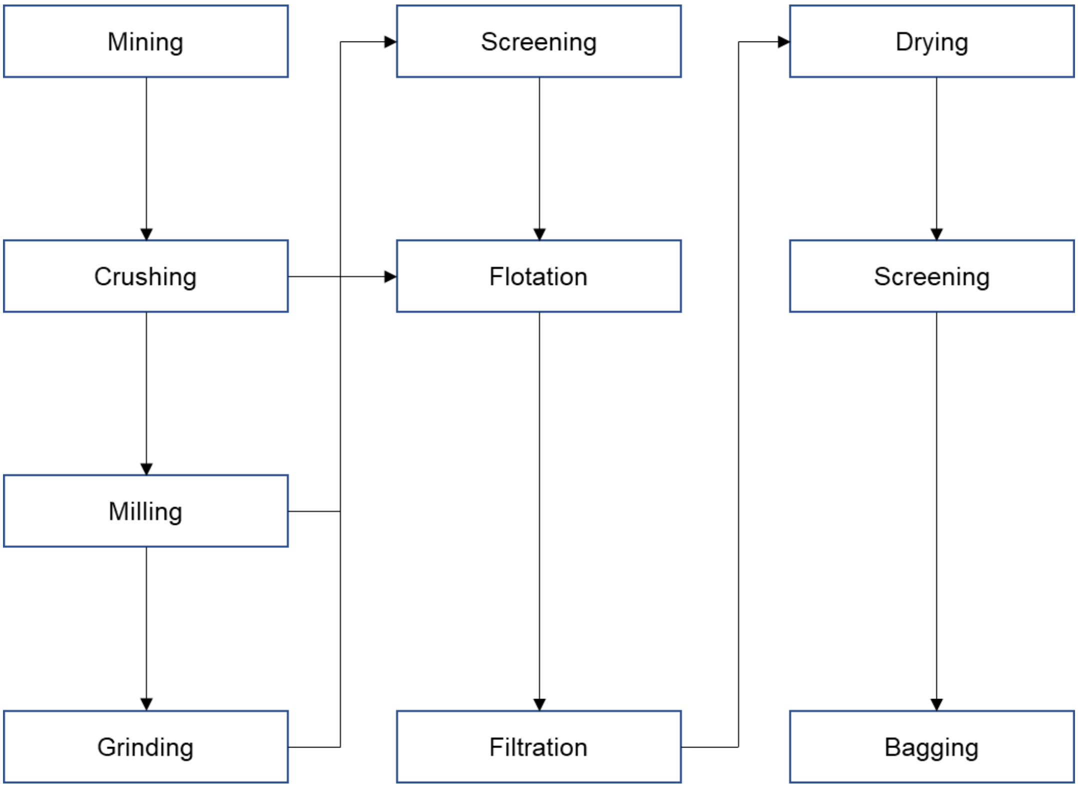

Figure 6. Example of beneficiation process for natural graphite on the mine site (Modified from Damn & Zhou, 2020)

The bagged product is then further refined (see Figures 5 and 6). Again, each of the discussed refining methods are unit processes, and the overall process may contain various methods in varying orders. Based on the final applications (battery anodes, EAFs, lubricants, etc.), different refining stages are needed. Chemical purification is one of the most common methods to produce high-grade graphite from graphite concentrates. Based on the mineralogical composition, different acids (e.g., HCl, HF, H_2SO_4, and HNO_3) can be used. From these acids, H_2SO_4 and HCl are both relatively efficient leaching agents, but not as effective as HF. Due to environmental concerns that HF causes and the relative cheap price of H_2SO_4, the latter mentioned is preferred. Leaching is usually performed after flotation, but there have been some studies where flotation has been performed for leaching residue. This has resulted in increased recoveries as the leaching has increased the hydrophobicity of the graphite (Jara et al., 2019; Chehreh Chelgani et al., 2015).

Additionally, roasting is an effective method to purify the graphite concentrates by extracting silicates and sulfides. The roasting process can include roasting, water washing, and alkali/acid leaching. With roasting at high temperatures of over 500 °C, the sulfides are thermal oxidized to SO_2. Additionally, NaOH treatment is done with roasting, where the impurities can be turned into water-soluble alkali silicates and extracted with water wash. Other products that are left can be treated with HCl or H_2SO_4 in acid leaching (Chehreh Chelgani et al., 2015).

Microwave irradiation is a not widely used but effective method in mineral refining. Microwaves have numerous advantages, including rapid and selective heating, fast on/off switching, high energy efficiency, and environmental sustainability. The microwave effect is caused by the conversion of electromagnetic energy to thermal energy. Each mineral has a unique ability to absorb energy and therefore can be selectively heated and decomposed. The microwave irradiation can be used as pre-treatment before any chemical leaching or comminution stage (Jara et al., 2019; Chandrasekaran et al., 2013). For example, as graphite is a weak absorber of microwave energy when compared to pyrite, there is a possibility to selectively heat pyrite. As the irradiation continues, the bonds in inorganic sulfur species like sulfate ion (SO_4^{2-}) can be broken and sulfur gases are released in gaseous form (Jara et al., 2019). There have been some studies where microwave irradiation was done for acid mixtures containing natural graphite. According to Li et al. (2013), the carbon content of graphite could be increased from 96% to over 99%.

Spheronization is an upgrading process where graphite concentrate is used as a feed material. This process is essential so that natural graphite can be upgraded and used as an anode material. In the first part of the process, the feed is micronized in a jet mill, where the flake size is reduced to 10-15 µm. Once the target size is achieved, the micronized graphite is rounded in impact mills (Northern Graphite, 2021). The product of this process is uncoated spherical graphite. Spherical graphite is transformed into coated spherical graphite during the coating process. Spheres are coated with a layer of pitch or asphalt and baked at temperatures above 1200 °C during the procedure. As a result, the spheres are coated with a hard carbon layer that protects the sphere from exfoliation and degradation (Yoshio et al., 2003; Northern Graphite, 2021).

2.2.3 Synthetic graphite

SG is a man-made substance made by the high-temperature processing of amorphous carbon materials like petroleum, needle coke, coal, and natural and synthetic organic materials. In some cases, SG can be precipitated from the pyrolysis of a carbonaceous gas like acetylene. SG can be produced in a variety of forms, including solid, granular, and powders, using a variety of different processes (Zhao, et al., 2022; Tamashausky, 2006). Synthetic graphite can be over 99.9 % pure, and therefore it is mainly used in high-end products where no impurities are allowed, like LIBs and EAFs. The structure has a higher porosity and therefore lower density and higher electrical conductivity, which results in a higher price than natural flake graphite. Synthetic graphite is available in particle sizes varying from 2 µm powders to 2 cm pieces (Robinson Jr., Hammarstrom, & Olson, 2017).

2.2.4 Graphite as battery raw material

In commercial LIB's, graphite is mainly used as a battery anode material (BAM) due to its abundance, low cost, long-life cycle, stable thermal and mechanical structure, non-toxicity, electrical conductivity, and prevention of dendrite formation in batteries. Not every type of graphite can be used, and an ultra-high graphite purity of over 99.95% is required. Also, high degree of crystallization and large flake size are preferred (Törmänen & Tuomela, 2021; Moradi & Botte, 2016). According to Zhao et al. (2022), in 2020, natural graphite accounted for 39% and synthetic graphite for 58% of the anode material market.

From natural graphite, only *vein* and *flake* graphite are suitable for batteries. As there is limited availability of vein graphite, it is not an abundant nor economical choice as a raw material for commercial LIBs. Therefore, natural *flake* graphite is the main source of primary graphite used in batteries (Moradi & Botte, 2016). The graphite concentrate produced in mines usually has a purity higher than 95%, but this is not enough for BAM. Further, the natural structure is complex and not suitable. The natural graphites are not isotropic, which means that the parallel and perpendicular directions to the basal planes are not the same (Moradi & Botte, 2016). This type of morphology affects the uniform distribution of the particles in the current collector. Additionally, natural graphite adheres to the current collector with the basal plane surface in the direction of current flow and the edge plane surface vertical to current flow (Jara et al., 2019). This type of orientation affects the lithium-ion intercalation into the graphite structure (Guo, et al., 2016). These problems are shown as poor rate capacity, and therefore upgrading processes are needed (Moradi & Botte, 2016). As discussed in the previous section, natural graphite refining can include purification steps like heat treatment and/or chemical treatment, spheronization, and coating (Northern Graphite, 2021; Jara et al., 2019; Moradi & Botte, 2016). When it comes to the total efficiency of the process, two to three tons of natural graphite are needed to produce one ton of battery grade graphite (Ritoe et al., 2022). The graphite demand is fulfilled with synthetic graphite, especially in countries where there is limited availability of natural flake graphite. Due to the really high temperature of 2500 °C, the SG process consumes a lot of energy, and the product is more expensive (Moradi & Botte, 2016).

Figure 7 presents China's dominance in the graphite and battery supply chains, accounting for about 60% of the production of NG anodes and 90% of SG anodes (Ritoe et al., 2022). Currently, NG anodes are produced from coated spherical graphite, and almost all the production takes place in China (BloombergNEF, 2021). Graphite, specifically SG production, causes a high CO_2 footprint as a result of an energy-demanding process combined with coal-based energy infrastructure in all of the main SG production countries: China, Japan, South Korea, the US, and Germany (see Figure 8) (Ritoe et al., 2022; World Bank, 2020; Blagoeva et al., 2019). The graphite market situation will be discussed in more detail in the next section. To gain a better understanding of the carbon intensity of energy production in different graphite-producing countries, Figure 8 shows primary energy generation by source for the most important countries involved in the natural, synthetic, and battery grade graphite supply chains.

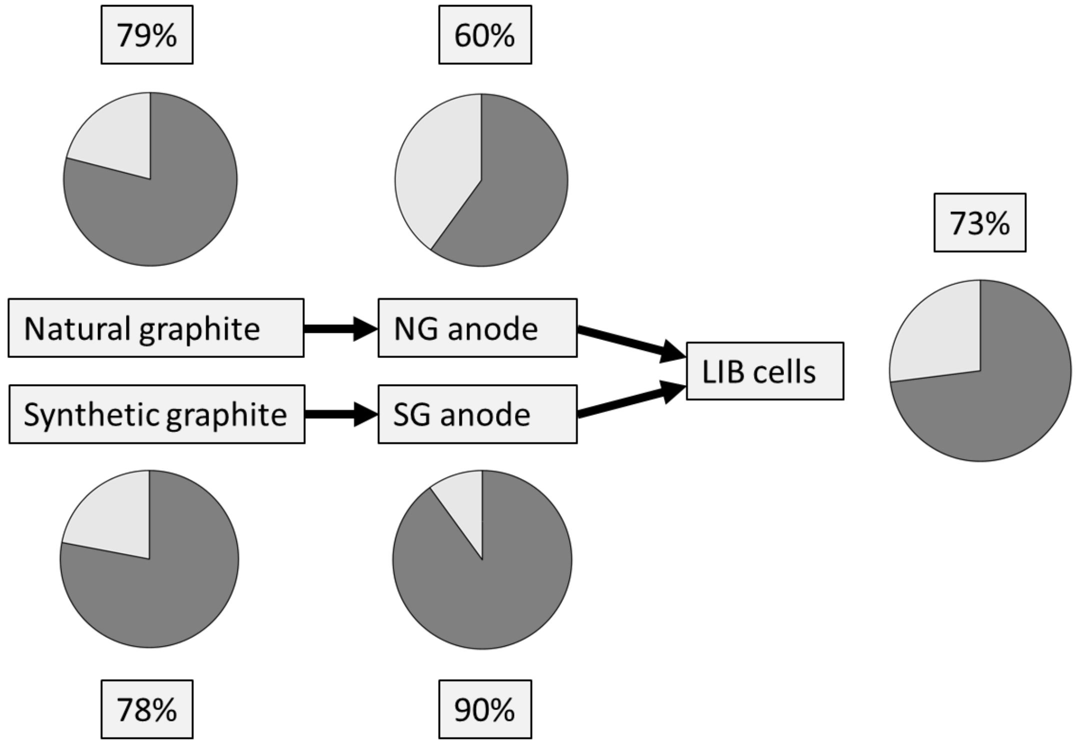

Figure 7. China’s dominance in graphite production and battery manufacturing (modified from Ritoe et al., 2022)

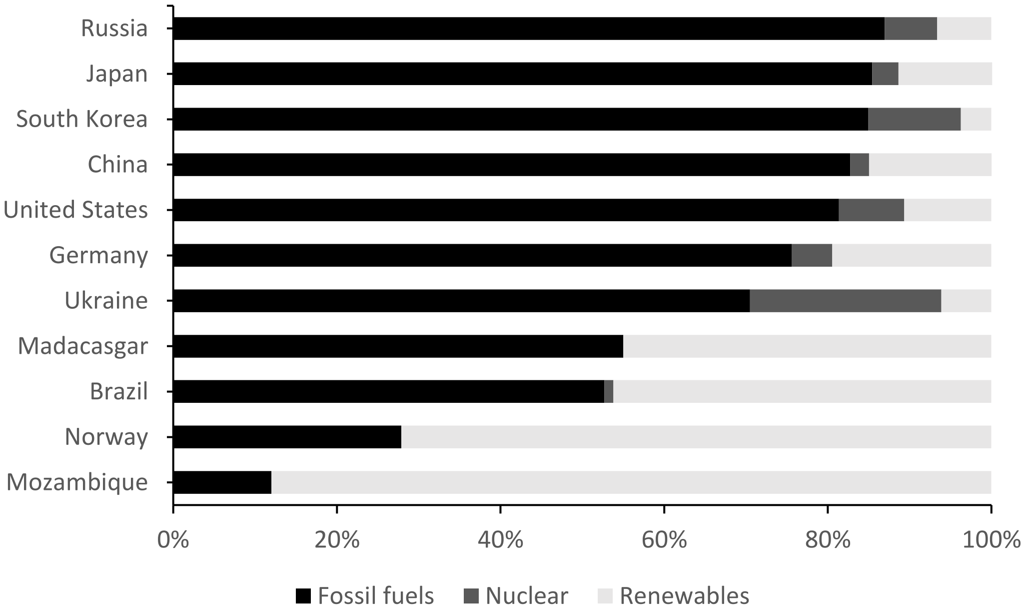

Figure 8. Primary energy generation by source (data from BP, 2022; IRENA, 2022)

The largest producers of NG (see Table 3) after China, with a production of over 10,000 tons per year, are Brazil, Mozambique, Russia, Madagascar, Ukraine, and Norway. In the NG BAM production chain, 40–50% of the energy consumption is accumulated in comminution, like crushing and milling (Gao et al., 2018; Jeswiet & Szekeres, 2016). For NG, the beneficiation stage is commonly done on the mine site. According to Figure 8, Brazil, Mozambique, Madagascar, and Norway have a substantially higher share of energy produced by nuclear or renewable sources than China. Therefore, NG mining and beneficiation in these countries would result in lower CO_2 emissions per kg of produced graphite product. Also, the potential for integrated upgrading processes such as the Renascor Resources Siviour project in Australia (Renascor Resources, 2021) could potentially provide benefits to the value chain. In the case of SG, the largest producers after China with over 20,000 ton of yearly production are Japan, South Korea, the US, and Germany (World Bank, 2020; Blagoeva et al., 2019). Of these countries, only the US and Germany have slightly (<10% units) lower carbon intensity in energy production (see Figure 8) when compared to China, whereas Japan and South Korea operate at a higher carbon footprint.

2.2.5 Market analysis

Graphite is an important mineral for multiple different industries. As discussed before, the demand is expected to increase significantly in the next 20 years. Most of this demand is coming from LIBs and electrodes used in steel production, as shown in Figure 9, where the projected demand by 2026 is presented (Fernley, 2020).

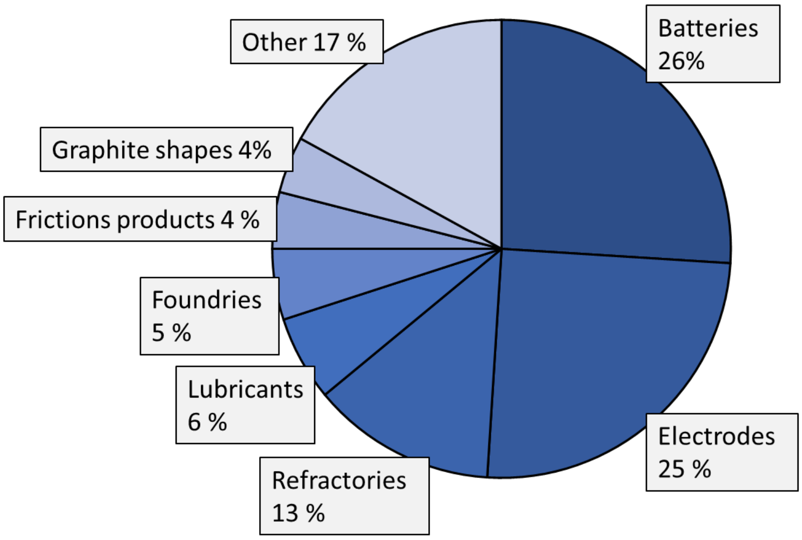

Figure 9. Graphite’s projected demand by 2026 (modified from Fernley, 2020)

The natural graphite production rates for the top 17 countries between the years 2018 and 2021 are presented in Table 3. The ranking is based on the production level, which is reported as metric tons. For the years 2018, 2019, and 2020, the data is confirmed; for 2021, it is estimated.

Table 3. Natural graphite production rates between 2018 and 2021 (USGS, 2020-2022)

Ranking (production in metric tons)	***Year of production***			
	2018	**2019**	**2020**	**2021 (estimate)**
China	693000	700000	762000	820000
Brazil	95000	96000	63600	68000
Mozambique	104000	107000	28000	30000
Russia	25200	25100	25000	27000
Madagascar	46900	48000	20900	22000
Ukraine	20000	20000	16000	17000
Norway	16000	16000	12000	13000
Korea, North	6000	6000	8100	8700
Canada	40000	11000	8000	8600
India	35000	35000	6000	6500
Vietnam	5000	5000	5000	5400
Sri Lanka	4000	4000	4000	4300
Mexico	9000	9000	3300	3500
Turkey	2000	2000	2500	2700
Austria	1000	1000	500	500
Germany	800	800	300	300
United States	0	0	0	0
Total	1102900	1085900	965200	1037500

Note: The data is a combination of USGS Mineral Commodity data (2020, 2021 and 2022). Only countries which are mentioned in all these statistics are included.

According to USGS (2022) and Table 3, China was the world's leading natural graphite producer in 2021, producing approximately 79% of the total world output. From this amount, approximately 24% was amorphous and 76% flake graphite. In 2021, China also processed most of the world's spherical graphite. China was also the only country that was able to increase its output during COVID-19. The growth rate has been remarkable; in 2018, China's share of total output was approximately 63%.

The next two top producers, Brazil, and Mozambique have not succeeded in maintaining the production levels so well. When comparing the 2021 to 2018 data, the production levels have decreased, in order, approximately 2% and 6.5%. Production has also decreased in Madagascar (-2%), Canada (-2.8%), and India (-2.6%). What should be noted is that Ukraine has maintained their stake well, but the ongoing Russo-Ukrainian war may have some impact on the outputs and their ratios. Additionally, most of the world's petroleum and coal-based coke is produced in China, so it also dominates SG production; in 2018, 78% of total output originated from there (Ritoe et al., 2022). What is clear is that countries in Europe are underdogs on a global scale. For example, Austria, Germany, and Norway contributed just 0.05%, 0.03%, and 1.3% of the total production in 2021, respectively (USGS, 2022).

The graphite market situation is currently in turmoil. According to Ritoe et al. (2022), the SG markets can become tighter in the future as in EAFs the SG is preferred. This can cause battery manufacturers to switch to NG as the other end applications of SG can increase its price. Further, as EVs are usually promoted as good for the environment, using unsustainable sources like Chinese SG or NG is not justified. Finally, China's position in the supply chain creates challenges for the EU and US, which have an interest in securing a supply of graphite as it is considered critical for clean energy technologies.

2.2.6 Circular economy in graphite mine tailings

The EU (2022) defines a circular economy as a model of production and consumption where the life cycle of any type of material is extended. In Table 4, circular economy concepts used in the mining industry are explained.

Table 4. Circular economy concepts in mining (adapted from Kinnunen et al., 2022; Lottermoser, 2010)

Concept	Meaning
Remining	Mineral recovery from old mine sites.
Reuse	Reuse of mining waste without reprocessing. For example, backfilling.
Recycling	Conversion of waste into valuable products by using physical, thermal, biological, and chemical methods.
Reprocessing and treatment	Using waste as feedstock to produce valuable products while reducing toxicity and total volume of waste.

As it will be discussed in section 2.4.3, the mine tailings are mostly gangue material, like sulfidic tailings, where acid mine drainage can be a risk. Furthermore, tailings are the largest waste stream in terms of both metal value and total volume (Kinnunen et al., 2022; Wang et al., 2014). Possible further utilization of these tailings may create potential for maximizing the use of resources and minimizing final waste. Sustainable operations can result in positive outcomes as environmental impacts can be reduced and waste can be used as a source for secondary metal production (Kinnunen et al., 2022). Some publications can be found focused on reuse (Maruthupandian et al., 2021; Lie et al., 2020) and reprocessing (Arachchige et al., 2021) of graphite mine tailings, however, the number is remarkably lower than in the case of base-metal tailings.

2.3 Aitolampi

In Finland, most of the NG deposits occur in graphite schist, a black schist containing graphite. In total, there are only two known deposits with grade-tonnage data: Aitolampi and Viistola, which are both in Eastern Finland (Törmänen & Tuomela, 2021). Both schist and gneisses are common in Finland. Additionally, Finland is covered by medium and high-grade metamorphism, which means that there is good potential for additional discoveries of flake graphite deposits (Törmänen & Tuomela, 2021). One of the known deposits, the Aitolampi graphite prospect, is owned by Beowulf Mining plc, which is a UK-registered exploration and development company. In 2016, a deposit was discovered 40 km southwest of Outokumpu at Heinävesi (Beowulf Mining, 2022). The location on the Finnish map is shown in Figure 10.

Figure 10. Aitolampi graphite prospect location (modified from MML, 2022)

The project is still in the exploration stage. In 2021, the Finnish Safety and Chemicals Agency (TUKES) authorized an extension for the previous exploration permit, and now ongoing exploration can continue until 2024. The 407.4 hectare exploration area (Pitkäjärvi, ML2016:0040) is shown in Figure 11 marked in red.

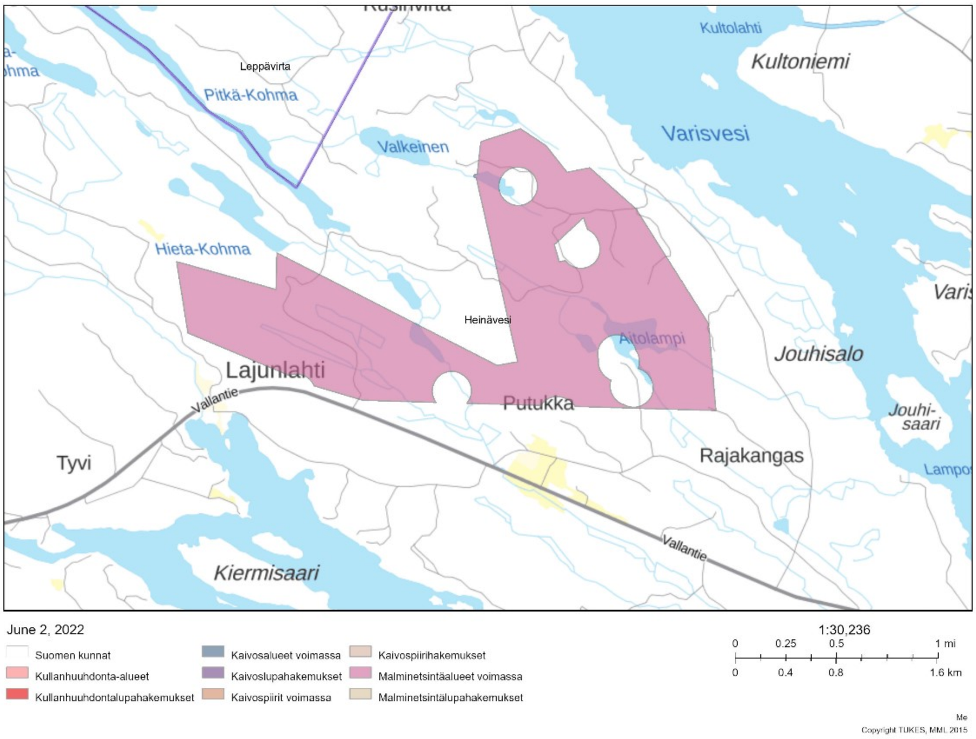

Figure 11. Aitolampi exploration area marked in red (TUKES; MML, 2015)

The latest mineral resource estimation (MRE) was conducted on August 28th, 2019. According to the global JORC Code (2012 edition), the indicated and inferred resource of 26.7 Mt at 4.8% Total Graphitic Carbon (TGC) for 1,275,000 tons of contained graphite was estimated. For the whole deposit, the estimated sulfur (S) content was 4.7% (Beowulf Mining, 2022).

2.3.1 Mineralization and metallurgy

The Aitolampi graphite schist occurs on a folding limb within a high-metamorphic quartz-feldspar-biotite gneiss. The graphite mineralization is found in two zones, which are referred to as the eastern and western lenses. The drill program has confirmed a strike length of at least 525 m for the eastern zone and 530 m for the western zone (Beowulf Mining, 2022). The mineralization zones with MRE data are presented in Figure 12.

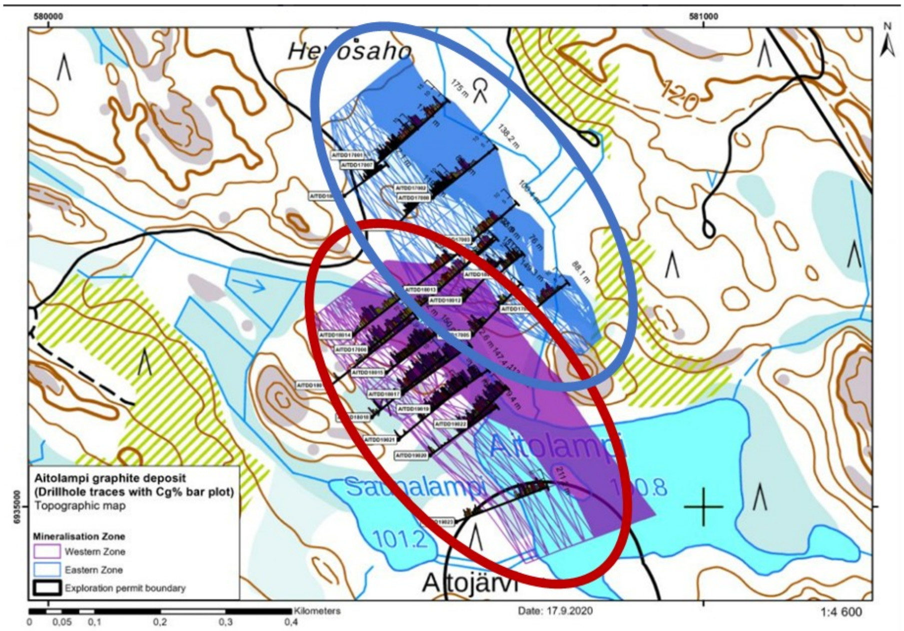

🟥 Western zone: Indicated + Inferred = 17.2 Mt @TGC 5.2%; S 4.8%

🟦 Eastern zone: Indicated + Inferred = 9.5 Mt @TGC 4.1%; S 4.5%

Figure 12. Aitolampi mineralization zones (modified from Beowulf Mining, 2022)

Metallurgical test work, including purification and characterization tests for three composited quarter drill core samples (MET-17001, MET-17002, and MET-17003), was conducted in 2017 by SGS Minerals Services in Canada. The characterization was performed by ProGraphite Gmbh in Germany (Beowulf Mining, 2022). The metallurgical test work result for drill core samples is shown in Table 5. The flake size is shown in µm and in Mesh, and the *C(t)* stands for total carbon grade.

Table 5. Metallurgical test results of Aitolampi ore (Beowulf Mining, 2022)

Flake type			***Fraction in %***		
Flake size	**Size in µm**	**Size in Mesh**	**MET-17001**	**MET-17002**	**MET-17003**
Jumbo	> 300	> 48	1.6	0.6	0.6
Large	180–300	80–50	17	12.2	13.4
Medium	150–180	150–80	30	26.8	29.2
Fine	< 106	< 150	51.4	60.4	56.8
C(t) concentrate (%)			96.8	97.2	97.5
Open Circuit Graphite Recovery (%)			87.3	77.8	91.4

Based on the results (see Table 5.) the graphite ore contains 0.6–1.6% jumbo sized flakes, 12.2–17% large flakes, and 26.8-30% medium sized flakes. The fines ranged from 51.4 to 60.4%. The overall recovery was 77.8-91.4% with a

96.8-97.5% carbon grade. According to Beowulf Mining (2022), there are multiple aspects which are benefiting the explored deposit in the markets. For example, with process optimization, the 99.95% purity, which is required for the LIB markets, may be possible to achieve. The studied graphite also shows high crystallinity, with a degree of graphitization of 98%, and the specific surface area is similar to that of high-quality flake graphite from China. In addition, Aitolampi graphite also has some other good features suitable for other applications like refractories, lubricants, and foundries.

2.3.2 Local community concerns

During the project, multiple concerns have been raised. As in the case of any project of this size, most concerns are related to how the mine affects the surrounding nature and local fauna. Non-governmental organizations Pro Heinävesi and the Finnish Association for Nature Conservation have summarized their concerns in statements against the mining project, which are presented in Table 6.

Table 6. Concerns related to Aitolampi graphite project (Leskinen, 2020; PRO Heinävesi, 2018; ISY-2004-Y210, 2005)

Concern	Challenges
Small particle pollution	Small particle pollution may have an impact on local fauna and the environment by causing heavy metal enrichment.
Noise, ground vibration and odor nuisance	People and fauna near the possible mine can become disturbed.
Beneficiation and tailings	Beneficiation by flotation will cause process waters and tailings containing sulfides and heavy metals, which can pollute local environment.
Asbestos	In similar kinds of deposits, tremolite and actinolite have been present.
Sulfidic sulfur	Acid mine drainage and lack of neutralization capacity. As example, consider the Särkiniemi mine (Leppävirta, Finland) (Leskinen, 2020).

2.4 Environmental aspects

As the target material grade is usually low in the known deposit, high volumes of waste are generated during different processing stages. The generated waste can cause multiple environmental problems, including acid mine drainage (AMD) and runoff waters containing dissolved metals (Blowes, et al., 2014). The risks are real before, during, and after the operations, of which there are multiple examples around the world like Brumadinho dam disaster in Brazil and case Talvivaara in Finland. It is hard to estimate the amount of waste created, but one estimate is that over 100 billion tons of solid waste are generated annually worldwide by the mining industry alone (Tayebi-

Khorami et al., 2019). The deposit where the studied tailings samples originate from occur in black schist, which is a common rock type in Finland. In addition to graphite, the host rock usually contains 5-10 wt.% sulfur, metals like zinc and nickel, and small amounts of copper and cobalt. Typically, the metal grades are less than 0.1 wt.%. The main sulfide minerals are pyrite and pyrrhotite, with some minor amounts of other sulfides like sphalerite (Törmänen & Tuomela, 2021).

2.4.1 Types of waste

Mining operations result in excavating large volumes of rock to get access to the ore. The ore is separated from the host rock depending on the economic cut-off grade. This results in the rock below the cut-off being categorized as waste and being dumped in waste rock piles (Blowes, et al., 2014). Another common waste type is called tailings, which, according to Lottermoser (2010), represents the largest volume of waste. Tailings are the materials that remain after the ore has been processed in the mill and the target minerals or metals have been liberated.

Usually, the first processing steps include crushing, grinding, and milling where the ore block size is reduced to a few millimeters or even microns. The goal of this process is to liberate the target minerals from the gangue phases (Lottermoser, 2010). In the second processing stage, the goal is to separate the target mineral from the gangue. This separation is usually done by utilizing different gravimetric, magnetic, electrical, or surface properties of ore and gangue. When the separation is finished, there are mainly two products: concentrate and tailings (Blowes et al., 2014; Lottermoser, 2010). The tailings usually consist of fine-grained sediment-water slurry. The solids are usually not valuable minerals like silicates, oxides, hydroxides, carbonates, and sulfides. The residual tailings are discharged to tailings storage facilities as a slurry of water and finely ground rock (Blowes, et al., 2014; Lottermoser, 2010).

2.4.2 Tailing storage facilities

The tailings storage facilities (TSF) are large surface impoundments and sedimentation lagoons that are designed to store solids. The impoundments are secured by dams, which are constructed like conventional water storage dams (World Bank, 2021). TSFs' sizes can vary from a few hectares to a thousand hectares and represent the largest environmental impact, especially on the landscape (Blowes et al., 2014; Lottermoser, 2010). Typically, tailings slurry contains about 30% solids, and the discharge to the impoundments is done from an elevated dam, which causes some hydraulic sorting between coarser and finer fractions. In some cases, the slurry is thickened before depositing, so that the particle size distribution will be more even (Blowes, 2014). The slurry is pumped to the TSF using structured pipelines and slurry pumps.

The TSFs are complex engineered structures which main purpose is to isolate the processing waste and reduce the environmental impact. The dams are usually built and raised mainly by three different methods, which are upstream towards the tailings, downstream away from the tailings, and centerline design (World Bank, 2021). From these structures, the upstream TSF has the highest failure rate, as every 20th dam of this type fails. What is remarkable is that more than 50% of TSFs worldwide are built using this method (Lottermoser, 2010). Further, there are multiple different environmental concerns related to TSFs. As the impoundment size is huge, it has a significant impact on the surrounding land. Additionally, as the structure is manmade, the stability of the dam can cause worry for the local community. In addition to that, for working TSF, a lot of pipelines are needed, which can rupture. As time goes by, the water in the tailings slowly drains away. Therefore, the generated solids can generate dust and cause air pollution, which can lead to acidification of the surrounding topsoil. As the water drains as seepage, there is a risk that it contaminates ground and surface water bodies in the area. Further, if sulfidic tailings are exposed to water and air, there is a possibility of AMD generation (World Bank, 2021; Lottermoser, 2010).

2.4.3 Sulfidic tailings and AMD

Pyrite (FeS) and pyrrhotite ($Fe_{1-x}S$) are the most abundant sulfide minerals with acid-generating behavior. Also, sphalerite (ZnS) is important to mention as it can have acid generating behavior depending on the contained iron (Lottermoser, 2010; Blowes, et al., 2014). Typically, these minerals are associated with graphite deposits (Puronaho, 2018). During the excavation and beneficiation processes, the gangue minerals will either end up in a waste rock dump or TSF, which results in high sulfide content in waste. Most of the concerns are related to the oxidation of these sulfides, which can result in the release of other elements into the water flowing through mine waste or into nature as a result of TSF damage (World Bank, 2021; Blowes, et al., 2014).

The oxidation reaction can occur if the sulfidic tailings are expressed with an oxidant and water, which triggers AMD. The reaction can happen in oxygenated or anoxic systems and can involve chemical, biological, and electrochemical reactions (Blowes et al., 2014). The sulfide oxidation usually commences in the unsaturated zone where oxygen can be accessed, while sulfidic tailings below the water table are protected (Kauppila & Räisänen, 2019). The reaction can cause a series of acid-producing and acid-buffering reactions, the formation of secondary minerals and low pH pore waters, including high levels of dissolved elements. The oxidation and weathering can result in the release of harmful elements like metals, metalloids, acids, and salts into the tailings pore waters, which can reach surface and groundwater systems (Lottermoser 2010). The oxidation of the pyrite in aqueous system is shown in equation (1) (Blowes et al., 2014).

$$FeS_2(s) + \frac{7}{2}O_2 + H_2O \rightarrow Fe^{2+} + 2SO_4^{2-} + 2H^+ \qquad (1)$$

Based on equation (1), for every mole of oxidized pyrite, one mole of Fe^{2+}, two moles of SO_4^{2-}, and two moles of H^+ are produced. The released Fe^{2+} can be oxidized to Fe^{3+}, as shown in equation (2).

$$Fe^{3+} + \frac{1}{4}O_2 + H^+ \rightarrow Fe^{3+} + \frac{1}{2}H_2O \qquad (2)$$

The Fe^{3+} can precipitate, which results in the reaction shown in equation (3).

$$Fe^{3+} + 3H_2O + H^+ \rightarrow Fe(OH)_3 + 3H^+ \qquad (3)$$

This yields the overall reaction from equations (1) – (3).

$$FeS_2(s) + \frac{15}{4}O_2(aq) + \frac{7}{2}H_2O \rightarrow Fe(OH)_3 + 2SO_4^{2-} + 4H^+ \qquad (4)$$

Therefore, a total of four moles of H^+ are released per mole of pyrite oxidized. Pyrrhotite oxidation can proceed through oxidative and nonoxidative reactions where O_2 and Fe^{3+} act as oxidants. The oxidation of pyrrhotite when oxygen is the primary oxidant is shown in equation (5) (Blowes et al., 2014).

$$Fe_{1-x}S + (2 - \frac{1}{2}x)O_2 + xH_2O \rightarrow (1-x)Fe^{2+} + SO_4^{2-} + 2xH^+ \qquad (5)$$

As shown in equation (5), the production of hydrogen ions is linked to the mineral stoichiometry. The release of H^+ can also result from the oxidation of the dissolved Fe, as shown in equation (6).

$$Fe^{2+} + \frac{1}{4}O_2 + \frac{5}{2}H_2O \rightarrow Fe(OH)_3 + 2H^+ \qquad (6)$$

The oxidation rates of both pyrite and pyrrhotite at 25 °C with standard atmospheric oxygen indicate that pyrrhotite can react 20 to 100 times faster than pyrite (Janzen et al., 2000). For sphalerite, the overall reaction where all sulfur is oxidized to sulfate is shown in equation (7) (Blowes et al., 2014).

$$ZnS + 4H_2O \rightarrow Zn^{2+} + SO_4^{2-} + 8H^+ \qquad (7)$$

As it is shown in previous reactions, weathering on sulfide minerals can generate hydrogen ions and sulfates, which results in acid generation. The generated acid can reduce the pH of the bodies of water and oxidize minerals where in contact (Henderson, 2018). AMDs are usually referred to together with the release of sulfates and heavy metals like iron (Fe), copper (Cu), lead (Pb), zinc (Zn), cadmium (Cd), cobalt (Co), chromium (Cr), nickel (Ni), and mercury (Hg), metalloids like arsenic (As) and antimony (Sb), and other elements like aluminum (Al), manganese (Mn), silica (Si), cadmium (Ca), sodium (Na), potassium (K), magnesium (Mg), and fluorine (F). In addition, microorganisms present can catalyze the AMD generating process by breaking down the sulfide minerals (Kiventerä, 2019; Blowes et al., 2014).

2.4.4 The EU Water Framework Directive

The EU Water Framework Directive (WFD), adopted in 2000, is an EU-wide directive where the main goal is to make Europe's water cleaner by focusing on the following aspects (EU, 2019):

- Expanding the scope of water protection to cover all waters
- Achieving good water status
- Water management based on river basins
- Pricing as approach for sustainable usage of water
- Involving citizens
- Making legislation more straightforward

In WFD article 4, there are the environmental objectives for both surface and groundwater. In this article, two clear obligations are set, which are: 1) to prevent deterioration of the status of water and 2) to achieve a good status of water (Soininen & Belinskij, 2020; Council of the European Union, 2000). The directive showed its potential at national legislation level in 2015 when the Weser case was settled. In this case, the Court of Justice of the European Union stated that the member countries must refuse authorization or permitting for any project that can cause deterioration of water or cause problems for status objectives (Soininen & Belinskij, 2020; Puharinen & Belinskij, 2020). As stated in both the previous mentioned sources, the deterioration of a single quality factor is prohibited even if the status of the whole water body is not changed. For both surface and ground water, there are example prejudices, C-461/13 for surface water and C-535/18 for ground water. These two prejudices have given the WFD more power, which has also been shown recently in Finnish industrial permitting (Niemelä, 2022). Table 7 presents some recent cases from Finnish industry, where already granted permits were overturned.

Table 7. Example of the overturned permits in Finnish industry

Case	Background	Source
Finnpulp	In 2019, the Supreme Administrative Court of Finland (SACF) overturned an earlier decision granting an environmental permit for bioeconomy investment. Decision was based on article 4 of WFD and prejudice C-461/13.	KHO:2019:166
Sokli mine	In 2022, SACF returned the environmental permit for a mine prospect to the Regional State Administrative Agency for review. The decision was based on article 4 of WFD and prejudice C-461/13.	KHO:2022:38
BASF	In 2022, SACF returned the environmental permit for a battery materials plant to the Regional State Administrative Agency for review. The decision was based on article 4 of the WFD and prejudice C-535/18.	KHO:2022:19

Additionally, in WFD article 10, it is stated that the emission control should be based on the best available techniques, which basically means that all actions should take place to mitigate the impact on surrounding waters (Council of the European Union, 2000). Therefore, the mining industry is motivated to develop and use more complex and efficient processes in which most of the harmful pollution, such as heavy metals and sulfidic minerals, is treated in such a way that it does not pose a presence risk for water bodies (EU, 2019; Turunen & Pasanen, 2019).

2.5 Mine waste characterization

The characterization of the mine waste is crucial for the successful prediction, prevention, and management of the environmental impacts. The prediction of the waste potential to produce AMD and other harmful drainage should be done way before ongoing operations. This way, it is possible to classify the waste, use it, for example, in the construction phase, and select suitable methods for its processing, closure, and rehabilitation before actual mining activities begin. Extractive waste is waste that is a result of mining activity. This includes, for example, tailings (solid or liquid-solid mixture of gangue, a by-product of mineral processing), waste rock (uneconomic rock), soil (soil that must be moved to get access to the ore) and topsoil (Tornivaara, et al., 2020). According to the Finnish Government (2013), the extractive waste can be classified as inert if, among other criteria, the concentration of sulfide sulfur in the waste is not more than 0.1% or not more than 1% when the neutralization potential ratio (NP/AP) is greater than three. In addition, the aqua regia (AR) extraction rates (ISO 11466, 1995) of the metals and semimetals Sb, As, Hg, Cd, Co, Cr, Cu, Pb, Ni, Zn, and V should not exceed the threshold value or background concentration in areas where background concentration is higher than threshold values (Karlsson, Alakangas, & Kauppila, 2021; Luodes, et al., 2011; Finnish Government, 2007). The natural concentrations and threshold values for metals and semimetals are shown in Table 8.

Table 8. Natural concentrations and threshold values for metals and semimetals (Finnish Government, 2007).

Metals and semimetals	Natural concentration (mg/kg; ppm)	Threshold value (mg/kg; ppm)
Antimony (Sb)	0.02	2
Arsenic (As)	1	5
Mercury (Hg)	0.005	0.5
Cadmium (Cd)	0.03	1
Cobalt (Co)	8	20
Chrome (Cr)	31	100
Copper (Cu)	22	100
Lead (Pb)	5	60
Nickel (Ni)	17	50
Zinc (Zn)	31	200
Vanadium (V)	38	100

According to the Finnish Government (2007), if the concentration of one or more substances exceeds the threshold value, soil contamination and remedial needs must be evaluated. The characterization of mine waste can include multiple different methods, depending on the focus.

Soil contamination

The threshold values shown in Table 8. are based on the natural concentration, which is based on the analysis of fines in moraine by extraction with AR. The AR-test is the most widely used extraction analysis method used in Finland, which especially dissolves elements bound to sulfide phases, which are the most problematic and raise concerns in terms of extractive waste (Karlsson et al., 2021). The analysis is recommended to be performed for particles smaller than 2 mm / 2000 µm following standards ISO 11466 or EN 13657 and measuring the concentrations of elements with ICP-AES/OES/MS or GFAAS. Hg should be defined pyrolytically (Luodes, et al., 2011; Finnish Government, 2007).

Sulfide sulfur

In extractive waste, sulfur can be present as sulfide (S^{2-}) or sulfate (SO_4^{2-}) in minerals (Matsumoto et al., 2018). A sulfide sulfur limit of 0.1% is set to ensure that the inert waste does not develop any AMD in the waste deposit area (waste rock dump/uncovered TSF) or in applications (e.g., roads). As stated in the previous section, the major AMD risk is based on the oxidation of sulfide minerals. Because there are no global standards for determining sulfide sulfur, the analyses are based on total sulfur analysis (Luodes, et al., 2011). When defining total sulfur, one should take into account that the analysis can overestimate the samples' potential to create AMD if a major part of the samples' sulfur is in another form than sulfide (Luodes, et al., 2011). Different methods of sulfur analysis include bomb combustion (EN 14582), high temperature combustion (ISO 351 or ISO 15178), iodine method (EN 1744-1), and Schöniger apparatus (EN 14582). Of these methods, the bomb combustion method is the preferred one in Europe (Punkkinen et al., 2019). Luodes et al. (2011) states in their paper that the most "baseline" results are achieved with bomb combustion or the high temperature bomb combustion method.

ABA test

Acid base accounting (ABA) is a static test used for extractive waste (Downing, 2014). The ABA tests do not give any information about the acid production or neutralization rates and are rather used to get information about the acid generation and neutralization potential. Usually, the static tests are performed first, and when more information is needed, kinetic tests, which can be measured in months or years, are performed (Punkkinen et al., 2019; Luodes et al., 2011). The ABA tests include the determination of sulfide sulfur (S%), which is used to calculate the acid potential (AP). The neutralization potential (NP) is based on the amount of carbonate (C%) and other alkaline material present in the sample. The ratio of NP and AP (NP/AP: neutralization potential ratio, NPR) or subtraction NP-AP (net neutralization potential, NNP) is then used to estimate the risk of AMD. The results are presented in kg $CaCo_3$/ton. There are several variations of the ABA test, including ABA with the Sobek method, modified ABA with the modified Sobek method, and an upgrade of the most used method (EN 15875) (Punkkinen, et al., 2019).

NAG test

The net acid generation (NAG) test is a static test to determine the waste rock or tailings potential to generate AMD. The NAG test is suitable for use as a prediction tool and in combination with the ABA test. The NAG test is based on the samples' reaction with hydrogen peroxide, which works as an oxidizing agent for sulfide minerals. During the test, when hydrogen peroxide is added, both acid generation and acid neutralization can occur. After the test, the final pH is recorded (NAG pH) and the sample is back titrated with NaOH to pH 4.5 and 7, and the net acid generation (NAG, H_2SO_4/ton) capacity is calculated (Karlsson, 2019; Weber et al., 2006). If the final NAG pH is higher than 4.5 and NAG is 0, the sample can be classified as non-acid formin (NAF), and when the NAG pH is lower than 4.5 and NAG is higher than 0, the sample can be classified as potentially acid-forming (PAF) (Shaw, 2005).

NAPP

The net acid production potential (NAPP) can be used together with NAG pH to have more detailed results and to compare results with ABA tests (Karlsson, 2019). The NAPP can be calculated as a subtraction between maximum potential acidity (MPA) and acid neutralizing capacity (ANC);

NAPP = MPA – ANC (Karlsson, 2019; Weber et al., 2006). According to Amira International (2002), the ANC can be calculated from NP (ANC = NP/50*49) and MPA from the S% (MPA = S%*30.6). NAPP, ANC, and MPA are expressed in H_2SO_4 equivalent as kg H_2SO_4 /ton. Basically, NAPP tells how many kilograms of sulfuric acid can be generated by one ton of material.

3 Materials and methods

This chapter reviews the implementation methodology of this research, including the main aim of the research. In the first section, the used raw material and characterization test work done are reviewed. After that, in the second and third sections, mechanical separation, including magnetic and gravity separation, and leaching experiments are introduced.

The aim of this study was to see if valuable metals and sulfidic sulfur could be recovered at a high enough grade from the graphite mine tailings to be economically viable. In addition, the leaching behavior of tailings and the possibility of reducing tailings' environmental impact were investigated. Two sets of a batch leaching series were conducted for the graphite mine tailings in sulfuric acid at atmospheric conditions. In the first set of experiments (ART_W_1_1-3), the acid molarity was increased step by step to get a better understanding of the leaching order of the sulfide minerals, clarify how the different elements dissolve, and to get information about the selectivity of the process. In the second set (ART_W_2_1-4), the solid-liquid ratio and temperature were changed to see if it was possible to optimize the leaching process. In addition, two types of mechanical processing tests—gravity and magnetic separation—were performed to get more information about the tailing's behavior in these processes.

3.1 Raw material and characterization test work

Pilot metallurgical test work of the ore samples was performed in Canada by SGS Mineral Services in 2017. In February 2022, two tailing samples, rougher tails eastern and rougher tails western, were sent to GTK Mintec (Outokumpu, Finland) for sample preparation. The reason for this was to prepare a series of sub-samples which each were tasked with a specific separation test. A total of 4.5 kg of both bulk samples were sent to Aalto Hydromet (Espoo, Finland) for further leaching experiments, and the rest were left to Mintec for further magnetic and gravity test work. The samples are referred to in this study as Aitolampi *rougher tails East (ART_E)* and Aitolampi *rougher tails West (ART_W)*. The sample characterization methods and results are discussed in the following subsections.

3.1.1 Chemical assays

The geochemical assays were performed by CRS Laboratories Oy (Kempele, Finland) by using a four-acid digestion method and inductively coupled plasma mass spectrometry (ICP-MS) to get multielement analysis of the elements present in the samples. Four-acid digestion dissolves the most minerals with minimized loss of elements. In the test, the sample is digested with combination of nitric, perchloric, and hydrofluoric acids with a final dissolution stage using hydrochloric acid (ALS, 2021).

The bomb combustion method was used to analyze the total carbon (C) and total sulfur (S) present in the sample. The analysis was performed using Leco analyzer. In the analysis the sample is combusted in high temperature furnace with oxygen. The combustion oxidizes the S to sulfur dioxide (SO_2) and the C to carbon dioxide (CO_2) and quantities are measured with infrared detection (Leco, 2021; Punkkinen, et al., 2019). The results for both analyses are shown in Table 9 in parts per million (ppm).

Table 9. ICP-MS and Leco analysis of the studied raw materials

Concentration in ppm		
Element	**Rougher tails East (ART_E)**	**Rougher tails West (ART_W)**
Ag	7	3
Al	66985	69163
As	5	7
Ca	17227	18713
Cd	9	20
Co	36	57
Cr	125	144
Cu	103	353
Fe	69664	73659
K	19763	22044
Li	24	26
Mg	16153	19882
Mn	439	481
Ni	234	328
P	606	656
Pb	28	32
S	28376	32920
Ti	1645	2032
Zn	920	1768
Leco C	3370	4410
Leco S	41900	44500

3.1.2 XRF

The solid X-ray fluorescence (XRF) assays were performed by CRS Laboratories (Kempele, Finland). The XRF results for both raw materials are shown in Table 10 in ppm. The major oxides are presented in Figures 13 and 14. It should be noted that not all elements are associated with oxygen, which is used as an equivalent component for elemental analysis. XRF is a non-destructive method used to determine the elemental composition of a material. Each mineral has a unique fluorescent x-ray, and with this x-ray, different elements can be recognized (ThermoFisher, 2020). With XRF, it is possible to detect major oxides and trace elements from the sample.

Table 10. XRF analysis of the studied raw materials

Concentration in ppm		
Element	**Rougher tails East (ART_E)**	**Rougher tails West (ART_W)**
Cu	100	330
Ni	280	340
Co	180	120
Zn	750	1540
Pb	60	70
Ag	10	10
As	0	0
Sb	110	100
Bi	20	20
Te	0	0
Y	34	30
Nb	14	9
Mo	7	55
Sn	30	20
W	0	0
Cl	120	100
Th	15	16
U	0	0
Cs	10	30
La	100	130
Ce	120	170
Ta	0	10
Ga	15	16
Si	295000	286000
Ti	3230	3380
Cr	150	190
V	430	730
Fe	71000	72800
Mn	320	340
Mg	18600	22800
Ca	17700	18700
Ba	560	560

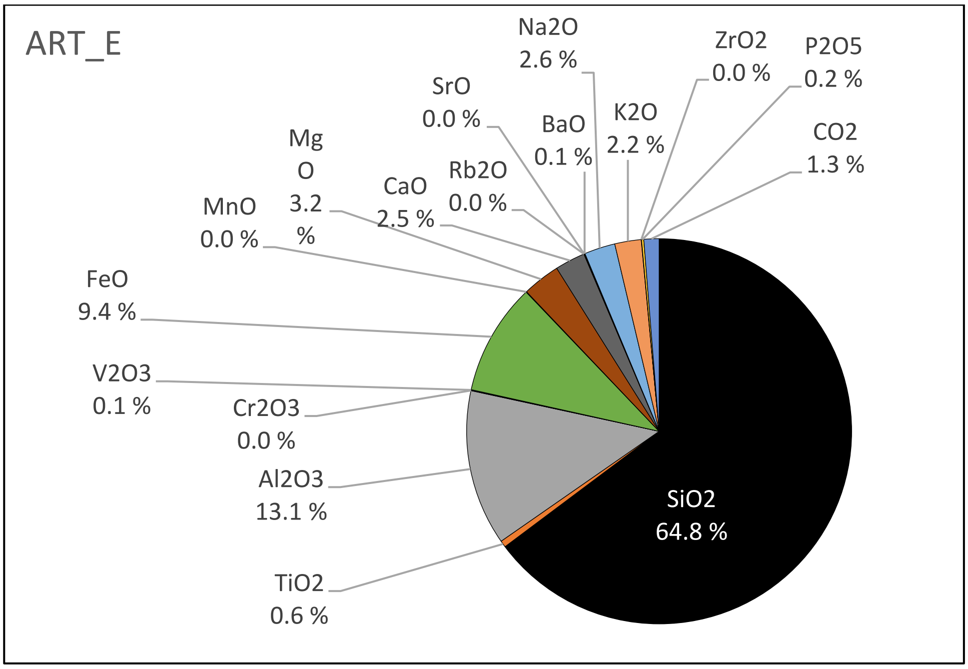

Figure 13. Major oxides of rougher tails East (ART_E)

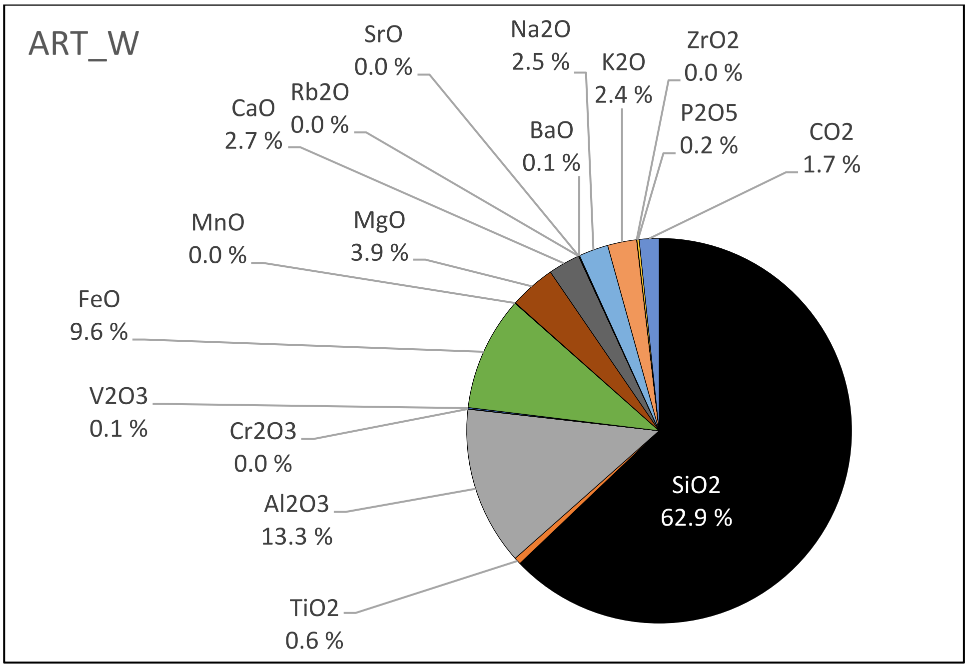

Figure 14. Major oxides of rougher tails West (ART_W)

3.1.3 Semi quantitative mineralogical analysis by XRD

X-Ray Diffraction (XRD) analyzes were conducted by X-ray Minerals Services (Wales, UK). XRD is a quantitative analysis method to determine minerals present in soils. The methods depend on the unique structure of the crystals of the minerals which response to the x-ray is measured (X-Ray Minerals Services Ltd, 2021). The XRD results for ART_E and ART_W are presented in Figure 15. The XRD diffractograms can be found in Appendix 1. What should be noted is that a major part of the pyrrhotite present is in monoclinic 4C form.

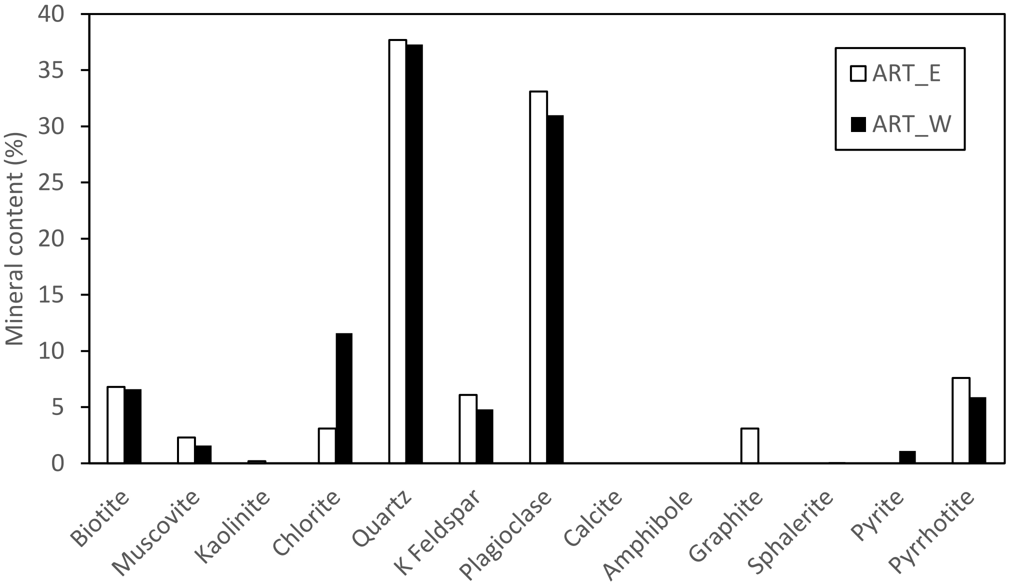

Figure 15. XRD of the studied raw materials ART_E and ART_W

3.1.4 Particle size distribution

The particle size distribution (PSD) was analyzed with a Malvern Mastersizer 3000 laser diffraction particle size analyzer. The PSD analysis was limited to the rougher tails East (ART_E). The measured d10, d50, and d90 values were 11 µm, 48 µm, and 256 µm. The frequency PSD (dashed line) and cumulative distribution (CDF, black line) are shown in Figure 16.

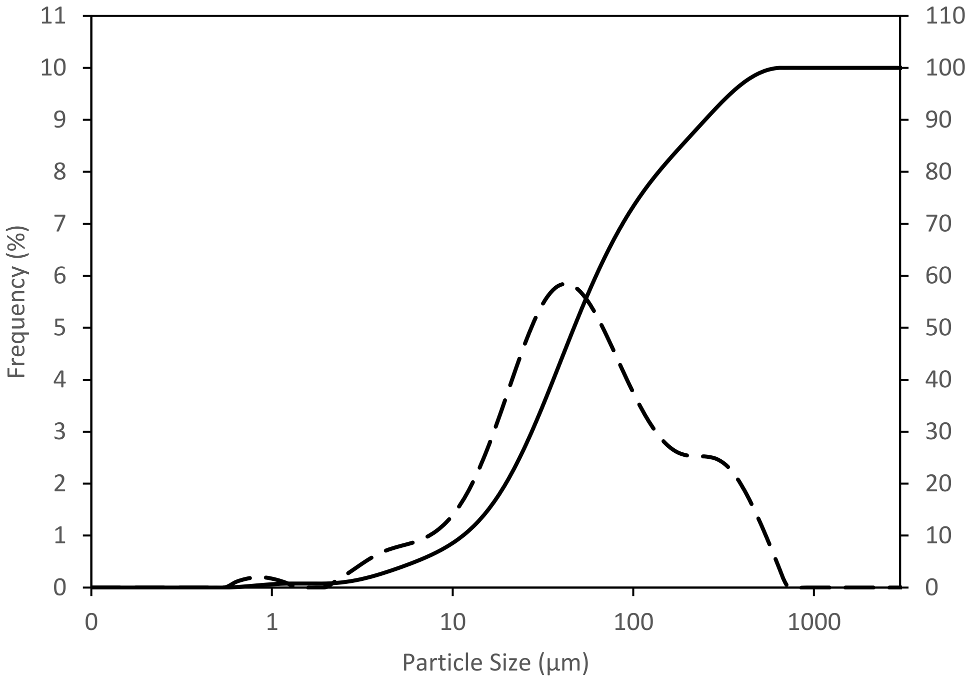

Figure 16. The observed particle size distribution of rougher tails East (ART_E)

3.1.5 SEM-MLA

The SEM-MLA (Scanning Electron Microscope – Mineral Liberation Analyzer) were conducted in GTK (Espoo, Finland) with JEOL JAS 7100F Schottky field emission SEM. SEM-MLA is an automatic analysis that identifies minerals and quantifies multiple mineral characteristics like abundance, grain size and liberation (Karlsson, 2019). Polished epoxy-resin blocks are used for the samples. As only a small amount of sample is used, it is important to prepare the sample so that it will represent the bulk sample. Additionally, it is important to note that a minimal amount of mixed size fractions should be present in prepared samples (Karlsson T. , 2019).

For the analysis, studied samples were sieved for <75 µm fraction. The dry sieving was performed since a major part of the material is between 60 and 80 µm and therefore the larger part might make the analysis more complex. The summary of SEM modal mineralogy analysis results is shown in Table 11 for both ART_E and ART_W as weight percentages. The raw data can be found in Appendix 2.

Table 11. Modal mineralogy of the studied raw materials

Mineral	wt% ART_E	wt% ART_W
Quartz	31.4	30.2
Plagioclase	26.1	15.1
Biotite	12.2	6.8
Pyrrhotite	10.3	12.9
K-Feldspar	6.8	7.9
Albite	4.5	8.8
Muscovite	2.5	3.6
Feldspar, Mixed	1.4	2.0
Clinochlore	1.0	3.8
Pyrite	0.8	1.8
Tremolite	0.6	1.4
Apatite	0.4	0.3
Chamosite	0.4	0.9
Rutile	0.3	0.6
Sphalerite	0.3	0.6
Others	1.2	3.2

3.1.6 Energy dispersive spectroscopy (EDS)

Point identification analysis was performed with an Oxford Instruments X-max SDD 80 mm^2 EDS in GTK (Espoo, Finland). Chemical identification and quantification can be accomplished using EDS, as most SEM instruments include an EDS analyzer. In the system, secondary and backscattered electrons are used in image formation for morphological analysis, and x-rays are used for chemical identification (Nasrazadani & Hassani, 2016). The main target was to find suitable candidate mineral phases for Ni, Co, Zn, Cu, and Sb. A summary of the EDS results is presented in Figures 17–20, including the chemical composition of each point analysis. It should be noted that from both samples, similar structures were found, and the following figures are used as the best examples.

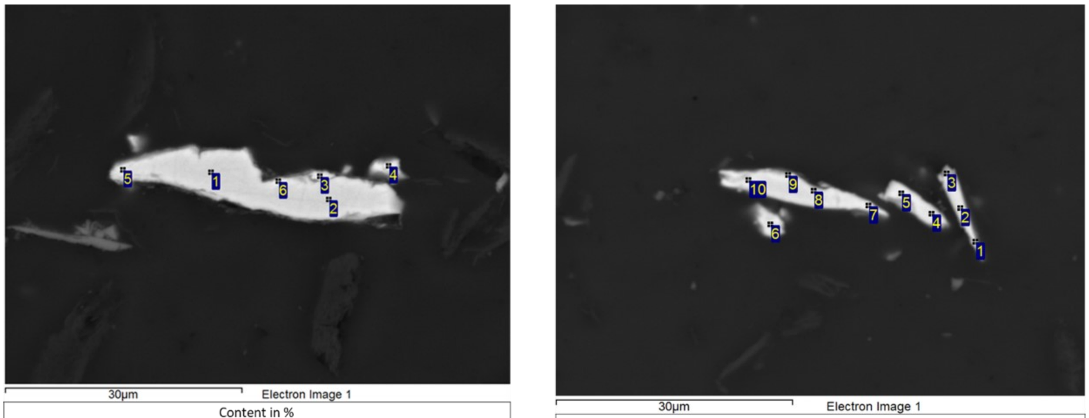

Content in %

Spectrum	O	Al	Si	S	Fe	Co	Ni
1				41.4	58.6		
2				41.1	58.9		
3	6.1			39.6	54.3		
4	7.1			39.1	53.8		
5				42.4	57.6		
6	8.6	0.4	1	34.9	32.3	4.6	18.3

Content in %

Spectrum	O	Al	Si	S	Cl	Fe	Ni	Cu
1	23.4	1.7	2.6	28.3	0.5	43.3		
2	4.6			38.8		56.2	0.5	
3	10.2			35	0.9	53		0.9
4				42.4		57.2	0.4	
5				41.8		58.2		
6				42.1		57.9		

Figure 17. EDS images – set 1: Both pictures represent pyrrhotite with some Co and Ni interlockings. Both images are from ART_E

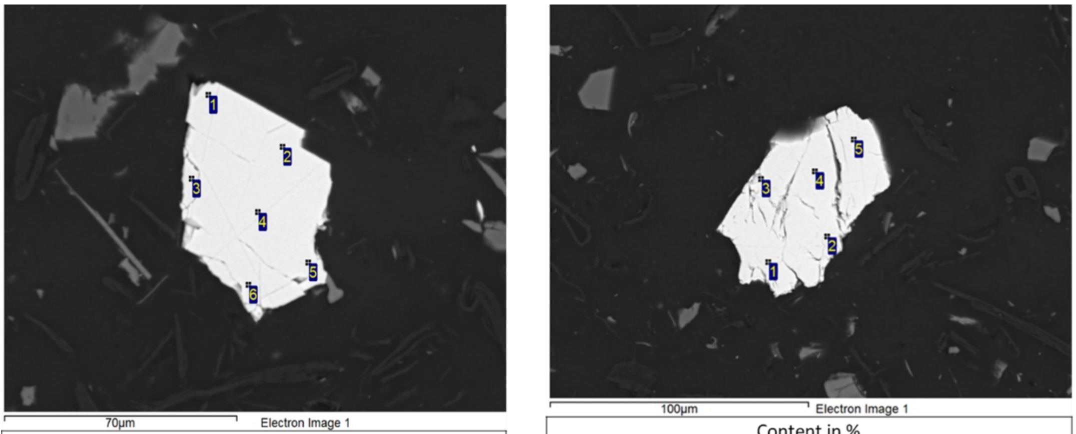

Content in %

Spectrum	O	S	Mn	Fe	Zn	Cd
1		34.2		7.3	57.6	1
2		33.7	0.3	7	58	1
3		34.3		7.5	57.3	1
4	0.7	33.1		6.9	58.4	0.8
5		34.4		5.4	60.2	
6		34.1		6.4	59.5	

Content in %

Spectrum	O	S	Mn	Fe	Zn
1		34.3		7.4	58.3
2		34.5	0.3	7.5	57.7
3	1.6	34.1		6.2	58.2
4		33.8		7.4	58.8
5		34.4	0.4	7.5	57.8

Figure 18. EDS images – set 2: Both pictures represent sphalerite. The left image is from ART_E, and the right image is from ART_W

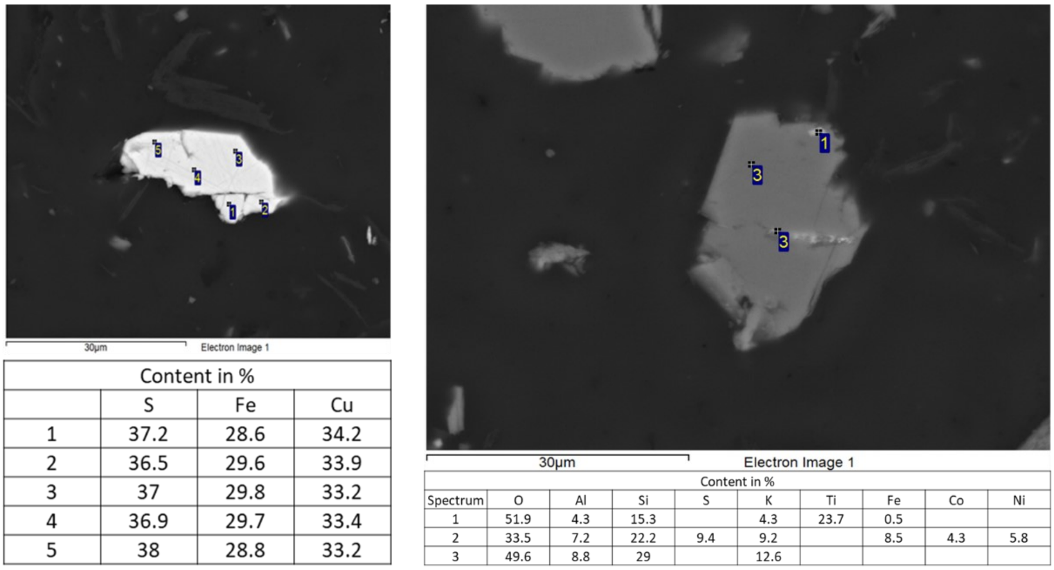

Content in %			
	S	Fe	Cu
1	37.2	28.6	34.2
2	36.5	29.6	33.9
3	37	29.8	33.2
4	36.9	29.7	33.4
5	38	28.8	33.2

Content in %									
Spectrum	O	Al	Si	S	K	Ti	Fe	Co	Ni
1	51.9	4.3	15.3		4.3	23.7	0.5		
2	33.5	7.2	22.2	9.4	9.2		8.5	4.3	5.8
3	49.6	8.8	29		12.6				

Figure 19. EDS images – set 3: Left: chalcopyrite in ART_W, right: biotite with interlocked sulfides in ART_W

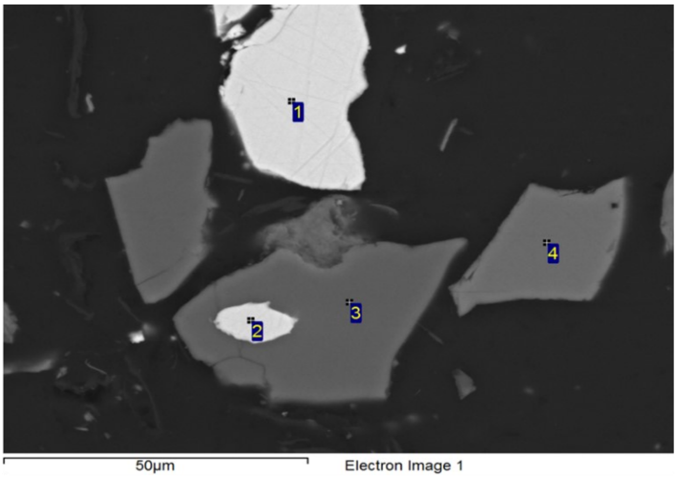

Content in %							
Spectrum	O	Na	Al	Si	S	K	Fe
1					40.9		59.1
2					41.3		58.7
3	55.2			44.8			
4	49.1	0.7	9.1	29.2		11.9	

Figure 20. EDS images – set 4: Silicate with pyrrhotite interlockings in ART_W

Both studied samples are somehow similar, so the following summary applies to both. According to Figure 17, Ni was mainly found as a solid solution with pyrrhotite. Pyrrhotite can contain up to 1% Ni and can contain pentlandite "flames", where the Ni content is higher (Brownscombe, et al., 2015). Additionally, some Co was found as a solid solution with pyrrhotite. Some Ni and Co were also found in biotite (see Figure 19). According to Figure 18, Zn was mainly present in sphalerite, which is the main candidate phase. Cu was mainly present as chalcopyrite (see Figure 19). Pyrrhotite was the dominant sulfide mineral phase, and the main source of Fe and S. Additionally, some sulfide mineral interlockings inside biotite and quartz were detected (see Figures 19 and 20). Based on SEM modal mineralogy results, Sb was found from plagioclase. However, when EDS analysis was done, it showed that no Sb was found. As in plagioclase, there is some calcium (Ca) as a trace element, and Ca's x-ray energy is really close to Sb's, so there is a possibility that Ca was misidentified as Sb.

3.1.7 AMD

The AMD tests were performed by Eurofins Environmental Testing Finland Oy. A summary of the AMD test results is shown in Table 12. The raw data with all the results and used methods can be found in Appendix 3.

Table 12. Summarized AMD test results for studied raw materials

Analysis	ART_E	ART_W	Unit
AP	130	130	$CaCO_3/t$
NP	2.6	9.9	$CaCO_3/t$
NPR	<0.1	<0.1	-
NAG-pH	2.3	2.4	-
NAPP	120	120	H_2SO_4/t
EC	305	278	mS/m

3.2 Mechanical processing

Two different mechanical processing tests were performed with raw materials ART_E and ART_W. To guarantee the uniform quality of the raw material, large enough quantities of raw material were used.

3.2.1 Magnetic separation

Three stage magnetic separation tests were performed with both ART_E and ART_W samples in GTK Mintec (Outokumpu, Finland). The general flowsheet is presented in Figure 21. The abbreviations are explained in Table 13.

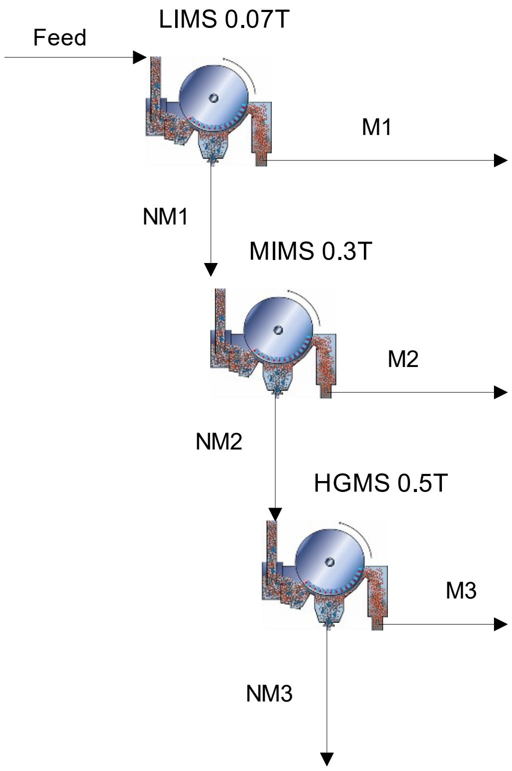

Figure 21. The general flowsheet of magnetic separation of ART_E and ART_W (flowsheet by Tero Korhonen)

Table 13. Magnetic separation abbreviations

Abbreviation	Meaning
LIMS	Low Intensity Magnetic Separator
MIMS	Medium Intensity Magnetic Separator
HGMS	High Gradient Magnetic Separator
M1-3	Magnetic product 1-3
NM1-3	Non-Magnetic product 1-3
T	Tesla, magnetic field intensity

The magnetic separation tests were done with approximately 1.5 kg feed batches. The measured finesses (d80) of the feed material were 171 µm for ART_E and 238 µm for ART_W. The feed material was mixed in bucket containing 15% solids and fed with peristaltic pump to the LIMS drum with 0.07T field. The non-magnetic product NM1 was cleaned with the MIMS drum with 0.3T field. Finally, the non-magnetic product NM2 was cleaned once with HGMS with 0.5T field. In Figure 22, the HGMS assembly in GTK premises is shown. As each mineral magnetic behavior differs, it is possible to extract different fraction from each other. In Table 14, a classification of minerals is shown based on their magnetic properties.

Table 14. Magnetic properties of minerals (Petrovskaya, 2019; Jirestig & Forssberg, 1992)

Strongly magnetic minerals	Pyrrhotite (monoclinic)
Medium magnetic minerals	Chlorite, Biotite
Weakly magnetic minerals	Sphalerite, Chalcopyrite
Nonmagnetic minerals	Quartz, Muscovite, Kaolinite, Feldspar, Plagioclase, Pyrite

According to Table 14, strongly magnetic minerals should be recovered with a lower magnetic field strength than others. In the magnetic separation flowsheet (see Figure 21), there are three different field strengths, so it is possible to estimate the content of each product. Pyrrhotite has a strong attraction towards magnets, so it should be recovered with LIMS. Medium magnetic minerals like chlorite and biotite should be recovered with MIMS, and sphalerite with HGMS. Therefore, a significant portion of the nonmagnetic product should be composed of nonmagnetic minerals. What should be noted is that not every mineral is pure, and there can be some magnetic interlocking inside that can affect the overall magnetic properties.

Figure 22. HGMS assembly in GTK Mintec (picture by Tero Korhonen)

In the separation process the material is mixed in the tanks and fed through the separating matrix canister. Different diameter flow restrictors can be used to adjust the separation process. In the tank the feed was mixed to 10% solids and the fed through the separating matrix canister. The used matrix in all tests was 3.5XRO (nominal top grain size 850 µm) and the flow restrictor diameter of 10 mm.

3.2.2 Gravity separation

Gravity separation tests with ART_E and ART_W were performed in GTK Mintec (Outokumpu, Finland) with small Deister shaking table concentrator. The basic flowsheet of the process is shown in Figure 23. The flowsheet abbreviations are explained in Table 15. The material was fed as dry with the vibrating feeder through the funnel on the shaking table. Approximately 3 kg batches were used for both samples. The feeding of the material and the shaking table is shown in Figures 24 and 25. The solids feed rate was about 8 kg/h with solids content of about 13%. Measured finesses (d80) of the feed material was 171 µm for ART_W and 238 µm for ART_E.

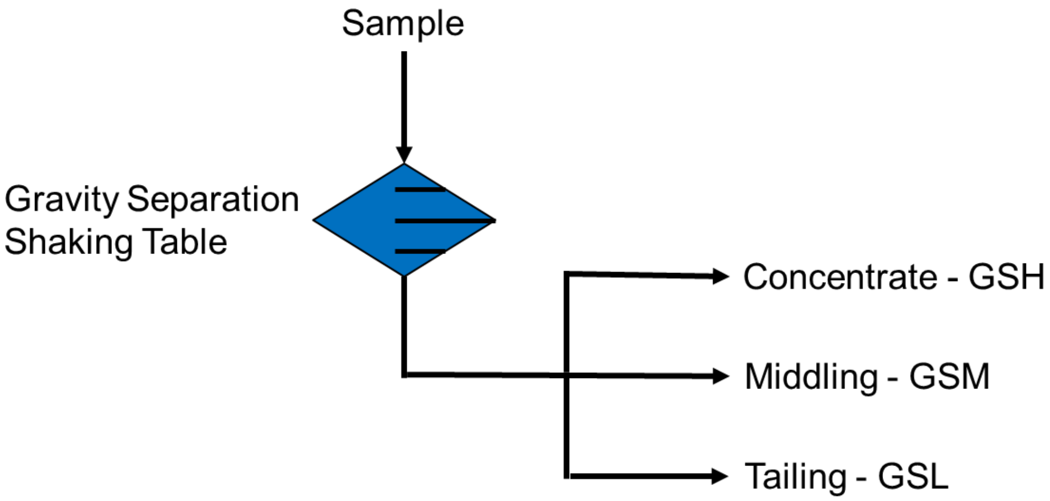

Figure 23. The general flowsheet of gravity separation for ART_E and ART_W

Table 15. Gravity separation abbreviations

Abbreviation	Meaning
GSH	Gravity Separation – Heavy Product
GSM	Gravity Separation – Middling's product
GSL	Gravity Separation – Light Product

As each mineral's relative density differs, it is possible to separate different fractions from each other. Relative densities of major gangue and sulfide minerals present in bulk samples are shown in Table 16.

Table 16. Relative densities of minerals (Mindat.org, 2022)

Mineral	Relative density
Kaolinite	2.6
K-Feldspar	2.6
Quartz	2.65
Plagioclase	2.6 - 2.8
Chlorite	2.6 - 3.3
Muscovite	2.8 - 2.9
Biotite	2.7 - 3.4
Sphalerite	3.9 - 4.1
Pyrrhotite	4.6
Pyrite	4.9 - 5.2

Heavy minerals such as sphalerite, pyrrhotite, and pyrite should be recovered into GSH, according to Table 16. Other minerals, where the relative density varies less, should be recovered as GSM and GSL products.

Figure 24. Feeding of the material to the shaking table (picture by Tero Korhonen)

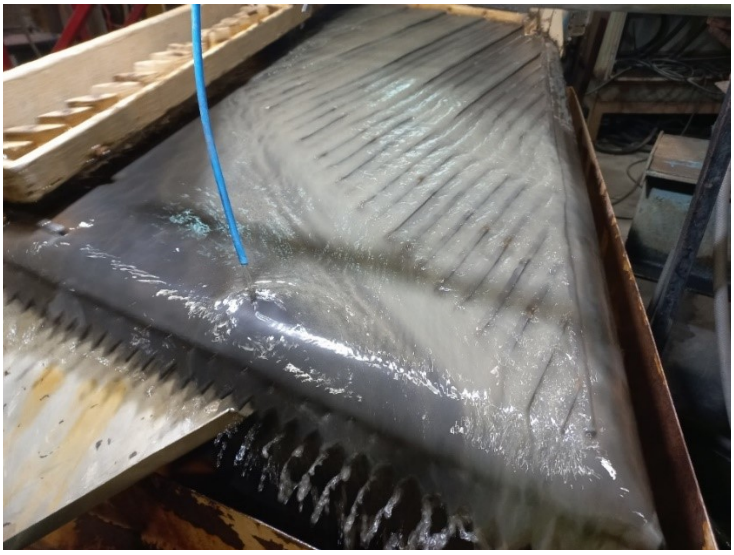

Figure 25. Gravity separation by the shaking table (Picture by Tero Korhonen)

3.2.3 Analysis and sampling

Each mass flow was collected and weighted. XRF and ICP-MS, and Leco were used for qualitative and quantitative analysis of the elemental composition of each mass flow. The data was used to calculate the recovery and grades for the studied elements. For comparison, both ICP-MS and XRF data were used in the calculations.

3.3 Leaching experiments

Leaching experiments were performed with an Aitolampi rougher tails West (ART_W) in Aalto Hydromet facilities. To guarantee uniform quality for each experiment, the bulk sample was divided into 80 g sub-batches using a sample divider. In the first set of experiments (ART_W_1_1-3), the concentration of the H_2SO_4 varied (0.02; 0.2; 2 mol/L). The parameters that were kept constant were agitation speed (400 rpm), leaching time (4 h / 240 min), oxygen flow (1 L/min), solid to liquid ratio (100 g/L), and temperature (90 °C). Suitable agitation speed was determined visually so that a perfect suspension was created for solids. In the second set of experiments (ART_W_2_1-4), the T and S:L varied from 45°C to 90°C and 50 g/L to 100 g/L, respectively. Additionally, the leaching time was cut in half to 120 minutes, and an H_2SO_4 concentration of 2 mol/L was used. Other parameters were kept the same as in the previous set. The list of experiments including used parameters is shown in Table 17.

Table 17. Leaching experiments and parameters for ART_W samples

Experiment	T (°C)	S:L (g/L)	H_2SO_4 (mol/L)	Time (min)	O_2 flow (L/min)
ART_W_1_1	90	100	0.02	240	1
ART_W_1_2	90	100	0.2	240	1
ART_W_1_3	90	100	2	240	1
ART_W_2_1	45	50	2	120	1
ART_W_2_2	90	50	2	120	1
ART_W_2_3	45	100	2	120	1
ART_W_2_4	90	100	2	120	1

The leaching solution (diluted sulfuric acid) was prepared from concentrated sulfuric acid (95% H_2SO_4, VWR Chemicals) and ion-exchanged water. Standard solution samples were preserved with nitric acid (Reag. Ph. Eur., ISO and 65% HNO3, Merck KGaA). A Sodium hydroxide solution was prepared from granules (NaOH, VWR Chemicals) and was used for acid-base titration to determine acid consumption during leaching. In titration, methyl orange was used as an indicator. Sodium hydroxide (2 mol/L) was used for the gas washing of hydrogen sulfide (H_2S). Oxygen gas (industrial grade, AGA) was added into the solution to boost the oxidative nature of the system. Reference standard solutions were utilized in the preparation of suitable standard solutions for atomic absorption spectroscopy (AAS) analysis.

Both pH (Mettler Toledo Seven Easy with InLab© Expert Pro-ISM probe) and redox potential (Mettler Toledo InLab© Redox electrode with 3 mol/L KCl electrolyte) were measured, but pH only in leaching experiments where the pH was higher than 0. Filtration of the solution samples was performed with syringe filters equipped with 1.2 µm pore size filters. After every leaching experiment, filtration of the pregnant leach solutions (PLS) was performed under vacuum using a Buchner funnel and a Whatman Grade 597 filter paper with a 4–7 µm pore size. The leaching set-up is shown in Figure 26.

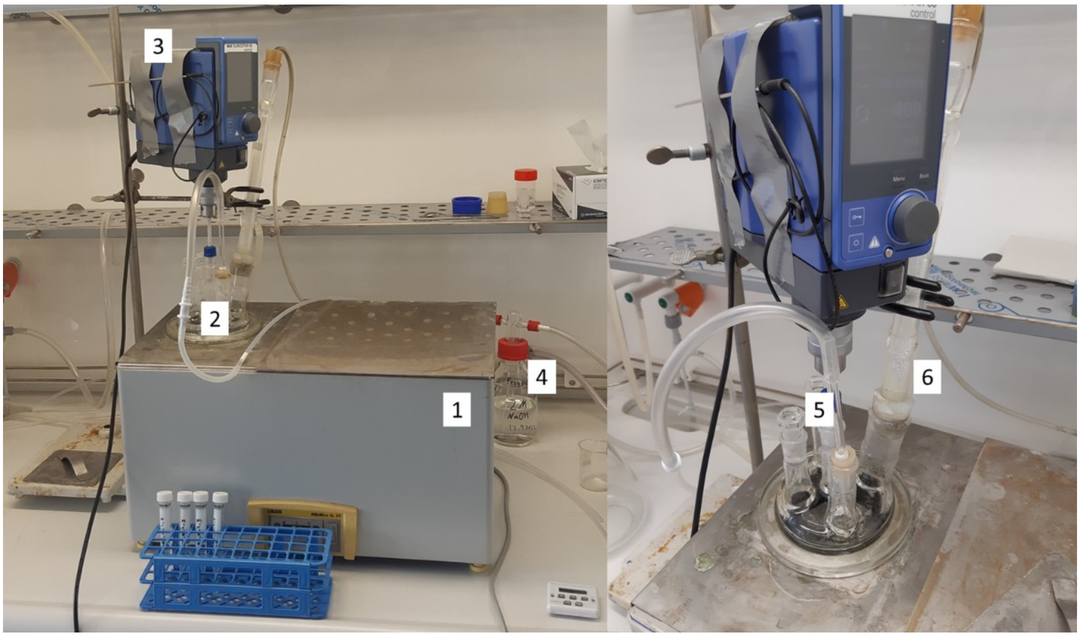

Figure 26. Batch leaching set-up for ART_W samples leaching, including 1) water bath, 2) glass reactor and cover, 3) overhead stirrer, 4) gas washing bottle, 5) glass sinter, and 6) condensing tube

3.3.1 Analysis and sampling

Redox potential and pH were measured at times of 5, 15, 30-, 60-, 120-, and 240-min. Solution samples were taken at the same time as the redox and pH measurements. The target volume of each sample was 10 mL, and each sample was filtered instantly after sampling. Co, Ni, Cu, Zn, and Fe concentrations were analyzed by AAS from each solution sample. Before AAS analysis, the samples were diluted to suitable concentrations with 2% nitric acid. After each experiment, the final residue slurry was filtered, and the volume of PLS was measured. Leaching residue (solids) was washed by heated water with a volume of approximately two times the filtration cake. Then the filtered and washed residue was dried in an oven (60 to 65 °C) for 48 hours. After drying, the mass of each residue was weighted. AAS data was used for a quantitative analysis of the elemental composition of each PLS. Additionally, the data was used to calculate the yields by comparing the PLS composition of target elements to the original raw material concentration determined with ICP-MS. From the total mass reduction, the leaching yield of solids was determined. The titration results were used to determine the acid consumption.

4 Results

This chapter focuses on the results of the characterization, mechanical processing, and leaching experiments. First, the characterization results are introduced. Second, mechanical processing results, including magnetic and gravity separation test work, are presented. Finally, the focus is put on the leaching experiment results.

4.1 Characterization of the raw material

In this section, the used characterization methods and results related to them are presented. Each method is discussed in its own subsection.

4.1.1 AMD risk

The geochemical data plot in Figure 27 displays the NAG pH vs. NAPP classification for the potential of net acid generation in tailings based on the AMD analysis results (see Table 12). In this plot, the marked quadrants represent the different classification categories: nonacid forming (NAF), potentially acid forming (PAF), and uncertain (UC) (Amira International, 2002). The ART_E is marked with a white dot and ART_W with a black dot. NAG pH is the lowest pH that the sample can reach, and NAPP is the total generation of acid in kg per ton of material. Based on the results, both raw materials, ART_E and ART_W, can be classified as potentially acid forming (PAF) and therefore possess a risk for generating AMD. The predictors of AMD are low NAG pH together with relatively high NAPP. Moreover, the predictors of AMD risk (see Table 12) are a low NPR and electrical conductivity (EC) values of 305 mS/m for ART_E and 278 mS/M for ART_W, which indicate inherent acidity and salinity in samples.

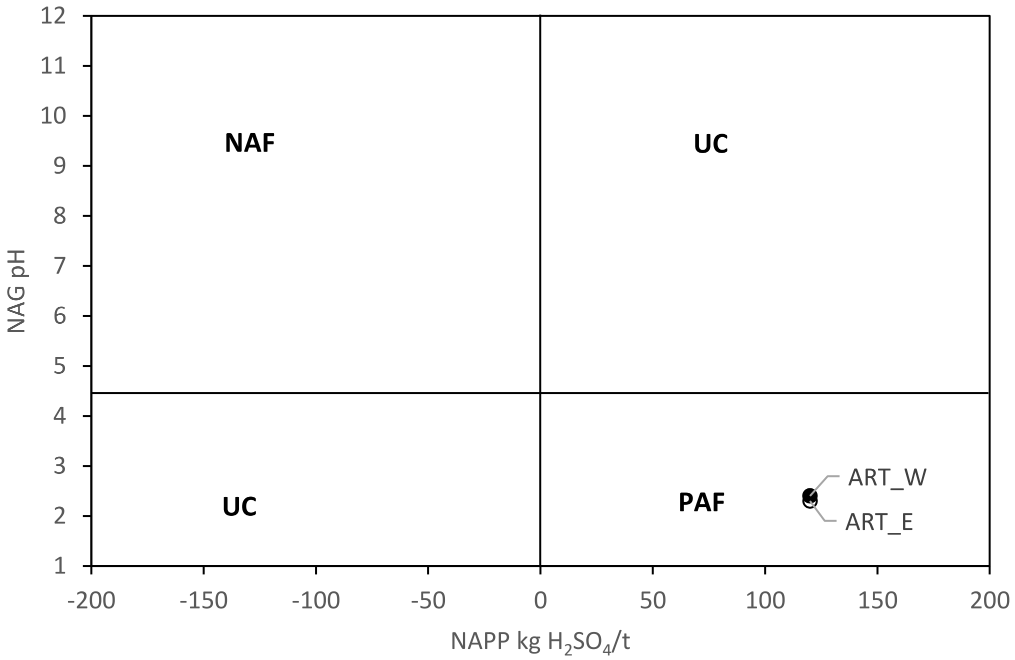

Figure 27. Geochemical data plot, NAG pH against NAPP (based on Amira International, 2002)

The main problematic sulfide minerals present in both samples are pyrrhotite, pyrite, and sphalerite. Based on the modal mineralogy data (see Table 11), in ART_W there are a higher number of sulfide minerals present. However, due to the higher presence of minerals with neutralization potential like albite and chlorite (Jambor et al., 2005), the overall NAG pH sets to a similar level with ART_E. The higher amount of sulfide minerals in ART_W is also shown in chemical assay data (see Table 9) where the Leco S value is higher when compared to ART_E.

4.1.2 Main contaminants

The comparison between the chemical analysis results (see Table 9. and Table 10.) and threshold values (see Table 8) determined by the Finnish Government (2007) was done with the Geochemical Abundance Index (GAI), using equation (8) (Müller, 1979). Results are shown in Table 18.

$$Log_2(\frac{C}{B}) \qquad (8)$$

In the formula, C represents the measured concentration and B the threshold value. The index of the enrichment is (Müller, 1979):

- 0: Unpolluted

- 1: Unpolluted / moderately polluted
- 2: Moderately polluted
- 3: Moderately / strongly polluted
- 4: Strongly polluted
- 5: Strongly polluted
- 6: Extremely polluted

Table 18. Geochemical Abundance Index of raw materials

Element	**GAI: ART_E**	**GAI: ART_W**
Sb	5.78	5.64
As	0.00	0.40
Hg	-	-
Cd	3.16	4.33
Co	0.86	1.50
Cr	0.33	0.53
Cu	0.04	1.82
Pb	< 0	< 0
Ni	2.23	2.71
Zn	2.20	3.14
V	2.10	2.87

Note: For other element than Sb and V, ICP data were used to calculate the GAI.

As shown in Table 18. Sb, Cd, Co, Cr, Cu, Ni, Zn and V possess a risk in terms of soil contamination. ART_W have higher index values in all studied elements and therefore the total contamination risk is higher than in case of ART_E. In both samples highest exceed (GAI >2) are in case of Sb, Cd, Ni, Zn and V.

4.2 Mechanical processing

In this section, the mechanical processing test results are presented. First, the focus is put on magnetic separation test work, and after that, gravity separation.

4.2.1 Magnetic separation

The magnetic separation test results for ART_E are shown in Tables 19 and 20. The "product" column displays each magnetic and non-magnetic product. Each target element's recovery rates and grades are displayed, and the "calculated feed" row summarizes the input mass and grades. Results based on both ICP-MS and XRF are shown, as there might be some variation due to the differences in nature between each analysis method. The complete results can be found in Appendix 4.

Table 19. ART_E: Magnetic separation results based on ICP-MS

Product	*Mass*		*S (Leco)*		*Fe (ICP-MS)*		*Cu (ICP-MS)*	
	g	**%**	**Grade (wt. %)**	**Rec. (%)**	**Grade (wt. %)**	**Rec. (%)**	**Grade (wt. %)**	**Rec. (%)**
M1	110.4	7.4	34.6	57.5	52.2	60.7	0.04	20.3
NM1	1382.7	92.6	2.0	42.5	2.7	39.3	0.01	79.7
M2	89.3	6.0	18.2	24.5	23.6	22.2	0.03	10.9
M1-M2	199.7	13.4	27.2	82.0	39.4	82.9	0.04	31.1
NM2	1293.4	86.6	0.9	18.0	1.3	17.1	0.01	68.9
M3	404.4	27.1	2.3	13.8	1.6	6.7	0.02	37.5
M1-M3	604.1	40.5	10.5	95.8	14.1	89.7	0.03	68.6
NM3	889.0	59.5	0.3	4.2	1.1	10.3	0.01	31.4
Calculated feed	1493.1	100.0	4.4	100.0	6.4	100.0	0.02	100.0
Product	*Mass*		*Ni (ICP-MS)*		*Co (ICP-MS)*		*Zn (ICP-MS)*	
	g	**%**	**Grade (wt. %)**	**Rec. (%)**	**Grade (wt. %)**	**Rec. (%)**	**Grade (wt. %)**	**Rec. (%)**
M1	110.4	7.4	0.2	60.6	0.01	46.6	0.02	3.7
NM1	1382.7	92.6	0.01	39.4	0.001	53.4	0.05	96.3
M2	89.3	6.0	0.1	23.2	0.01	15.4	0.1	12.6
M1-M2	199.7	13.4	0.1	83.8	0.01	62.1	0.1	16.2
NM2	1293.4	86.6	0.004	16.2	0.001	37.9	0.04	83.8
M3	404.4	27.1	0.01	6.8	0.001	15.6	0.1	38.7
M1-M3	604.1	40.5	0.1	90.6	0.004	77.7	0.1	54.9
NM3	889.0	59.5	0.004	9.4	0.001	22.3	0.03	45.1
Calculated feed	1493.1	100.0	0.02	100.0	0.002	100.0	0.04	100.0

Table 20. ART_E: Magnetic separation results based on XRF

Product	*Mass*		*S (Leco)*		*Fe (XRF)*		*Cu (XRF)*	
	g	%	Grade (wt. %)	Rec. (%)	Grade (wt. %)	Rec. (%)	Grade (wt. %)	Rec. (%)
M1	110.4	7.4	34.6	57.5	49.0	53.0	0.04	22.1
NM1	1382.7	92.6	2.0	42.5	3.5	47.0	0.01	77.9
M2	89.3	6.0	18.2	24.5	21.0	18.4	0.03	15.9
M1-M2	199.7	13.4	27.2	82.0	36.5	71.4	0.04	38.0
NM2	1293.4	86.6	0.9	18.0	2.3	28.6	0.01	62.0
M3	404.4	27.1	2.3	13.8	5.3	20.8	0.01	28.4
M1-M3	604.1	40.5	10.5	95.8	15.6	92.2	0.02	66.4
NM3	889.0	59.5	0.3	4.2	0.9	7.8	0.01	33.6
Calculated feed	1493.1	100.0	4.4	100.0	6.8	100.0	0.01	100.0
Product	*Mass*		*Ni (XRF)*		*Co (XRF)*		*Zn (XRF)*	
	g	%	Grade (wt. %)	Rec. (%)	Grade (wt. %)	Rec. (%)	Grade (wt. %)	Rec. (%)
M1	110.4	7.4	0.2	53.4	0.02	9.9	0.03	2.9
NM1	1382.7	92.6	0.01	46.6	0.012	90.1	0.09	97.1
M2	89.3	6.0	0.1	19.1	0.02	9.4	0.1	3.9
M1-M2	199.7	13.4	0.1	72.5	0.02	19.3	0.0	6.8
NM2	1293.4	86.6	0.008	27.5	0.012	80.7	0.09	93.2
M3	404.4	27.1	0.02	15.9	0.007	14.9	0.2	75.6
M1-M3	604.1	40.5	0.1	88.4	0.011	34.3	0.2	82.5
NM3	889.0	59.5	0.005	11.6	0.014	65.7	0.03	17.5
Calculated feed	1493.1	100.0	0.03	100.0	0.013	100.0	0.08	100.0

In Tables 21 and 22, the magnetic separation test results of ART_W are presented. The results are presented in the same manner as for ART_E.

Table 21. ART_W: Magnetic separation results based on ICP-MS

Product	***Mass***		***S (Leco)***		***Fe (ICP-MS)***		***Cu (ICP-MS)***	
	g	**%**	**Grade (wt. %)**	**Rec. (%)**	**Grade (wt. %)**	**Rec. (%)**	**Grade (wt. %)**	**Rec. (%)**
M1	131.5	8.5	32.4	64.1	47.1	41.4	0.05	13.8
NM1	1416.4	91.5	1.7	35.9	6.2	58.6	0.03	86.2
M2	68.6	4.4	10.1	10.4	15.4	7.1	0.07	10.4
M1-M2	200.1	12.9	24.7	74.5	36.2	48.5	0.05	24.1
NM2	1347.8	87.1	1.3	25.5	5.7	51.5	0.02	75.9
M3	426.2	27.5	2.1	13.8	5.4	15.4	0.05	44.7
M1-M3	626.3	40.5	9.4	88.2	15.3	63.9	0.05	68.8
NM3	921.6	59.5	0.8	11.8	5.9	36.1	0.01	31.2
Calculated feed	1547.9	100.0	4.3	100.0	9.7	100.0	0.03	100.0
Product	***Mass***		***Ni (ICP-MS)***		***Co (ICP-MS)***		***Zn (ICP-MS)***	
	g	**%**	**Grade (wt. %)**	**Rec. (%)**	**Grade (wt. %)**	**Rec. (%)**	**Grade (wt. %)**	**Rec. (%)**
M1	131.5	8.5	0.3	63.5	0.01	35.0	0.04	1.0
NM1	1416.4	91.5	0.02	36.5	0.002	65.0	0.31	99.0
M2	68.6	4.4	0.1	7.7	0.00	6.4	0.1	1.5
M1-M2	200.1	12.9	0.2	71.1	0.01	41.4	0.1	2.6
NM2	1347.8	87.1	0.015	28.9	0.002	58.6	0.32	97.4
M3	426.2	27.5	0.01	9.2	0.002	19.0	0.4	40.3
M1-M3	626.3	40.5	0.1	80.3	0.004	60.4	0.3	42.9
NM3	921.6	59.5	0.015	19.7	0.002	39.6	0.27	57.1
Calculated feed	1547.9	100.0	0.04	100.0	0.003	100.0	0.28	100.0

Table 22. ART_W: Magnetic separation results based on XRF

Product	*Mass*		*S (Leco)*		*Fe (XRF)*		*Cu (XRF)*	
	g	**%**	**Grade (wt. %)**	**Rec. (%)**	**Grade (wt. %)**	**Rec. (%)**	**Grade (wt. %)**	**Rec. (%)**
M1	131.5	8.5	32.4	64.1	47.6	56.6	0.04	10.2
NM1	1416.4	91.5	1.7	35.9	3.4	43.4	0.03	89.8
M2	68.6	4.4	10.1	10.4	15.2	9.4	0.07	9.0
M1-M2	200.1	12.9	24.7	74.5	36.5	66.0	0.05	19.2
NM2	1347.8	87.1	1.3	25.5	2.8	34.0	0.03	80.8
M3	426.2	27.5	2.1	13.8	5.3	20.6	0.05	42.3
M1-M3	626.3	40.5	9.4	88.2	15.3	86.6	0.05	61.5
NM3	921.6	59.5	0.8	11.8	1.6	13.4	0.02	38.5
Calculated feed	1547.9	100.0	4.3	100.0	7.1	100.0	0.03	100.0
Product	*Mass*		*Ni (XRF)*		*Co (XRF)*		*Zn (XRF)*	
	g	**%**	**Grade (wt. %)**	**Rec. (%)**	**Grade (wt. %)**	**Rec. (%)**	**Grade (wt. %)**	**Rec. (%)**
M1	131.5	8.5	0.2	59.7	0.02	19.4	0.04	2.3
NM1	1416.4	91.5	0.02	40.3	0.007	80.6	0.16	97.7
M2	68.6	4.4	0.1	10.2	0.01	6.6	0.1	3.4
M1-M2	200.1	12.9	0.2	69.9	0.01	26.0	0.1	5.7
NM2	1347.8	87.1	0.012	30.1	0.006	74.0	0.16	94.3
M3	426.2	27.5	0.02	14.5	0.007	25.9	0.4	70.2
M1-M3	626.3	40.5	0.1	84.4	0.010	51.9	0.3	76.0
NM3	921.6	59.5	0.009	15.6	0.006	48.1	0.06	24.0
Calculated feed	1547.9	100.0	0.03	100.0	0.007	100.0	0.15	100.0

With ART_E (see Table 19), about 57.5% of the sulfidic sulfur with a grade of 34.6% was already recovered into M1 product with LIMS 0.07T. After the second stage, MIMS 0.3T, the cumulative sulfur recovery was 82% with a 27.2% grade. Finally, after the third separation stage, HGMS 0.5T, the cumulative sulfur recovery into magnetic products was 95.8% with a 10.5% grade. The sulfur content in the final non-magnetic product NM3 was 0.3%. Similar results were achieved with ART_W (see Table 21). About 64.1% of sulfur with a 32.4% grade was recovered with LIMS 0.07T. The cumulative sulfur recovery after MIMS 0.03T was 74.5% and after HGMS 0.5T was 88.2% with a 9.4% grade. The sulfur content in NM3 was 0.8%.

For Fe (see Table 19–22), depending on the raw material and analysis method, the corresponding results were 41.1–60.7% recovery with a 47.1–52% grade after LIMS, 48.8–8.29% recovery with a 36.2-39.4% grade after MIMS, and 63.9%–92.2% recovery with a 14.1–15.6% grade after HGMS. The Fe content of NM3 ranged from 0.9 to 5.9%. As presented in Tables 29–22, in M1, 10.2–22.1% of the total Cu, 53.4-63.5% Ni, 9.9–46.6% Co, and 1.0–3.7% Zn were recovered. In M2, the cumulative recoveries were 19.2-38%, 69.9-83.8%, 19.3-62.1%, and 2.6-16.2%; and in M3, 61.5-68.8%, 80.3-90.6%, 34.3-77.7%, and 42.9-82.5%. The Cu, Ni, Co, and Zn content in NM3 varied from 0.001 to 0.27%. Figure 28 represents the recovery of target elements in magnetic products as an example of the process's selectivity. The figure is based on ICP-MS results shown in Tables 20 and 22.

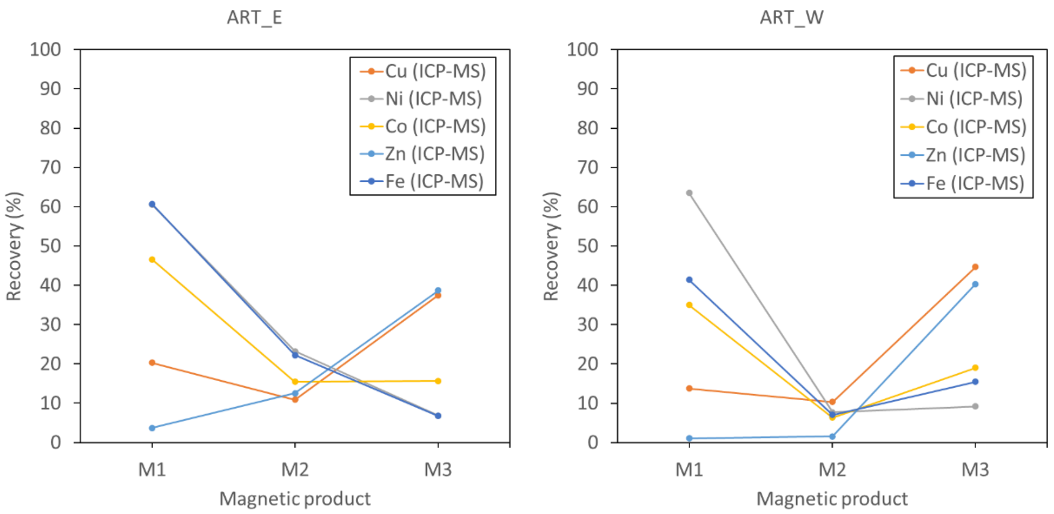

Figure 28. Recovery in magnetic products

To highlight the enrichment ratios of Cu, Ni, Co, Zn, S, and Fe, grade/mass feed comparisons were made. As an example, the results from Table 21 are summarized for ART_W in Figure 29.

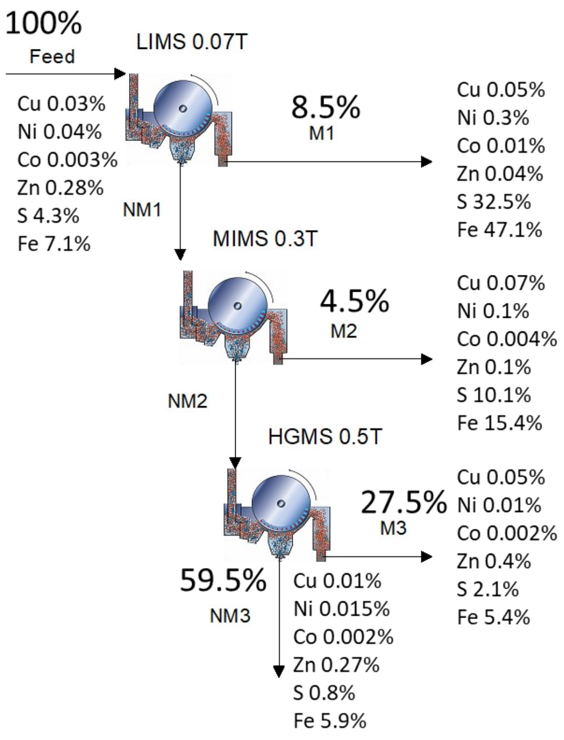

Figure 29. ART_W: Input and output mass flows and grades in magnetic separation

4.2.2 Gravity separation

Gravity separation test results for ART_E are shown in Tables 23 and 24. Gravity products are shown in the "product" column. Recovery rates and grades are shown for each target element, and the "calculated feed" row summarizes the input mass and grades. Results based on both ICP-MS and XRF are shown, as there might be some variation due to the differences in nature between each analysis method. The complete results can be found in Appendix 5.

Table 23. ART_E gravity separation results based on ICP-MS

Product	***Mass***		***S (Leco)***		***Fe (ICP-MS)***		***Cu (ICP-MS)***	
	g	**%**	**Grade (wt. %)**	**Rec. (%)**	**Grade (wt. %)**	**Rec. (%)**	**Grade (wt. %)**	**Rec. (%)**
GSH	244.1	8.1	27.0	54.6	38.0	43.8	0.04	20.8
GSM	2190.0	72.9	2.0	36.3	4.2	43.3	0.01	62.8
GSL	568.0	18.9	1.9	9.1	4.8	12.9	0.01	16.5
Calculated feed	3002.1	100.0	4.0	100.0	7.1	100.0	0.01	100.0
Product	***Mass***		***Ni (ICP-MS)***		***Co (ICP-MS)***		***Zn (ICP-MS)***	
	g	**%**	**Grade (wt. %)**	**Rec. (%)**	**Grade (wt. %)**	**Rec. (%)**	**Grade (wt. %)**	**Rec. (%)**
GSH	244.1	8.1	0.1	48.0	0.01	44.1	0.26	25.7
GSM	2190.0	72.9	0.01	39.6	0.001	42.4	0.06	50.7
GSL	568.0	18.9	0.02	12.3	0.001	13.5	0.1	23.6
Calculated feed	3002.1	100.0	0.02	100.0	0.002	100.0	0.08	100.0

Table 24. ART_E gravity separation results based on XRF

Product	***Mass***		***S (Leco)***		***Fe (XRF)***		***Cu (XRF)***	
	g	**%**	**Grade (wt. %)**	**Rec. (%)**	**Grade (wt. %)**	**Rec. (%)**	**Grade (wt. %)**	**Rec. (%)**
GSH	244.1	8.1	27.0	54.6	36.6	43.1	0.03	21.1
GSM	2190.0	72.9	2.0	36.3	4.2	44.1	0.01	58.7
GSL	568.0	18.9	1.9	9.1	4.7	12.8	0.01	20.3
Calculated feed	3002.1	100.0	4.0	100.0	6.9	100.0	0.01	100.0
Product	***Mass***		***Ni (XRF)***		***Co (XRF)***		***Zn (XRF)***	
	g	**%**	**Grade (wt. %)**	**Rec. (%)**	**Grade (wt. %)**	**Rec. (%)**	**Grade (wt. %)**	**Rec. (%)**
GSH	244.1	8.1	0.1	41.9	0.03	13.9	0.23	23.4
GSM	2190.0	72.9	0.02	44.9	0.016	71.1	0.06	53.9
GSL	568.0	18.9	0.02	13.1	0.013	15.0	0.1	22.7
Calculated feed	3002.1	100.0	0.03	100.0	0.016	100.0	0.08	100.0

In Tables 25 and 26, the gravity separation test results of ART_W are presented. The results are presented in the same manner as for ART_E.

Table 25. ART_W gravity separation results based on ICP-MS

Product	*Mass*		*S (Leco)*		*Fe (ICP-MS)*		*Cu (ICP-MS)*	
	g	**%**	**Grade (wt. %)**	**Rec. (%)**	**Grade (wt. %)**	**Rec. (%)**	**Grade (wt. %)**	**Rec. (%)**
GSH	244.1	8.1	24.7	42.6	33.8	33.2	0.07	16.4
GSM	2190.0	72.9	3.0	42.5	5.6	46.1	0.03	49.3
GSL	568.0	18.9	2.3	14.9	5.5	20.6	0.04	34.3
Calculated feed	3002.1	100.0	4.4	100.0	7.7	100.0	0.03	100.0
Product	*Mass*		*Ni (ICP-MS)*		*Co (ICP-MS)*		*Zn (ICP-MS)*	
	g	**%**	**Grade (wt. %)**	**Rec. (%)**	**Grade (wt. %)**	**Rec. (%)**	**Grade (wt. %)**	**Rec. (%)**
GSH	244.1	8.1	0.2	34.5	0.01	37.5	0.55	24.4
GSM	2190.0	72.9	0.02	45.2	0.002	41.6	0.12	43.3
GSL	568.0	18.9	0.02	20.3	0.002	20.9	0.2	32.3
Calculated feed	3002.1	100.0	0.03	100.0	0.003	100.0	0.17	100.0

Table 26. ART_W gravity separation results based on XRF

Product	*Mass*		*S (Leco)*		*Fe (XRF)*		*Cu (XRF)*	
	g	**%**	**Grade (wt. %)**	**Rec. (%)**	**Grade (wt. %)**	**Rec. (%)**	**Grade (wt. %)**	**Rec. (%)**
GSH	244.1	8.1	24.7	42.6	32.6	32.7	0.07	16.8
GSM	2190.0	72.9	3.0	42.5	5.6	47.0	0.02	46.7
GSL	568.0	18.9	2.3	14.9	5.3	20.4	0.04	36.5
Calculated feed	3002.1	100.0	4.4	100.0	7.6	100.0	0.03	100.0
Product	*Mass*		*Ni (XRF)*		*Co (XRF)*		*Zn (XRF)*	
	g	**%**	**Grade (wt. %)**	**Rec. (%)**	**Grade (wt. %)**	**Rec. (%)**	**Grade (wt. %)**	**Rec. (%)**
GSH	244.1	8.1	0.1	31.9	0.02	12.5	0.50	23.6
GSM	2190.0	72.9	0.03	46.7	0.015	65.5	0.11	43.8
GSL	568.0	18.9	0.03	21.4	0.011	22.0	0.2	32.5
Calculated feed	3002.1	100.0	0.04	100.0	0.015	100.0	0.16	100.0

With ART_E (see Table 23) about 54.6% of the sulfidic sulfur with a grade of 27.0% was recovered into shaking table concentrate, 36.3% with a grade of 2.0% into middlings, and 9.1% with a grade of 1.9% into tailings. Similar results were achieved with ART_W (see Table 25). Of the sulfidic sulfur, 42.6% with a grade of 24.7% was recovered into shaking table concentrate, 42.5% with a grade of 3.0% into middlings, and 14.9% with a grade of 2.3% into tailings.

For Fe (see Tables 23–26), depending on the raw material and analysis method, the corresponding results were 32.6-38.0% recovery with a 32.7–43.8% grade into concentrate, 43.3–47.0% recovery with a 4.2–5.6% grade into middling, and 12.8%–20.6% recovery with a 6.9–7.7% grade into tailings. Further, into the concentrate, 16.4–21.1% of the total Cu, 31.9–48.0% Ni, 12.5–44.1% Co, and 23.4–25.7% Zn were recovered. In middlings, the recoveries were 46.7–62.8%, 39.6-46.7%, 41.6-71.1%, and 43.3-53.9%, and in tailings, 16.5–36.5%, 12.2–21.4%, 13.5-22.0%, and 22.7–32.5%, respectively. Figure 30 represents the recovery of target elements from magnetic products as an example of the process's selectivity. The figure is based on ICP-MS results shown in Tables 23 and 25.

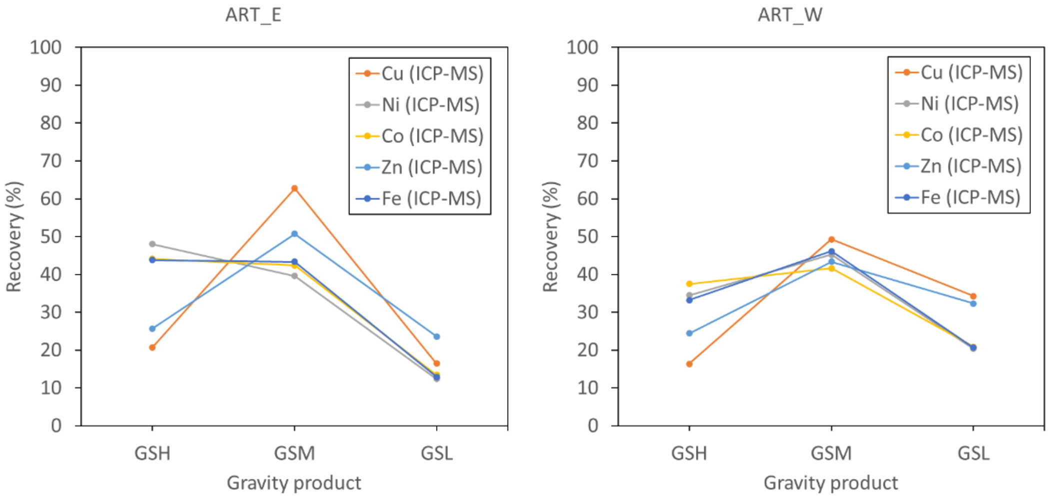

Figure 30. Recovery in gravity products

To highlight the enrichment ratios of Cu, Ni, Co, Zn, S, and Fe, grade/mass feed comparisons were made. As an example, the results from Table 25 are summarized for ART_W in Figure 31.

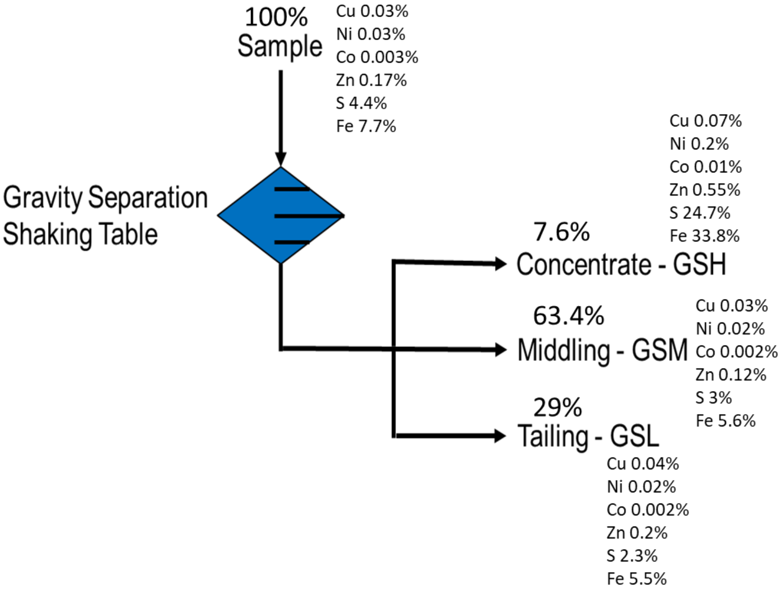

Figure 31. ART_W: Input and output mass flows and grades in gravity separation

4.3 General leaching behavior

As the tailings are complex mineral mixtures, some background on the leaching behavior is important to understand the results. In the leaching solution, the redox potential is mainly controlled by the dissolved oxygen. Therefore, if the amount of oxygen increases, the redox potential increases, and vice versa. The pH of the solution can be controlled by adding acid or base (Multani & Waters, 2018). In the studied samples, the target metals were found from sulfide phases. The *rest potential*, also known as leaching potential or open circuit potential, tells how easily different minerals or metals oxidize. In an electrolytic environment, rest potential is measured against a standard reference electrode such as a standard hydrogen electrode (SHE) or saturated calomel electrode (SCE) (Corrosionpedia, 2018).

Each mineral and metal have a unique lower limit potential, where less noble minerals have a lower limit potential (e.g., pyrrhotite: -0.28 V vs. SHE) and more noble ones higher (e.g., pyrite: 0.64 V vs. SHE). When metals and minerals with different rest potentials are present, e.g., in solution, the less noble undergoes corrosion and works as an anode and is oxidized, whereas the more noble works as a cathode. The material, which is less noble, therefore undergoes electrochemical dissolution and is so-called leached. This reaction between two materials is called galvanic interaction, which is presented in Figure 32 (Multani & Waters, 2018; Liu, et al., 2018; Becker, 2009).

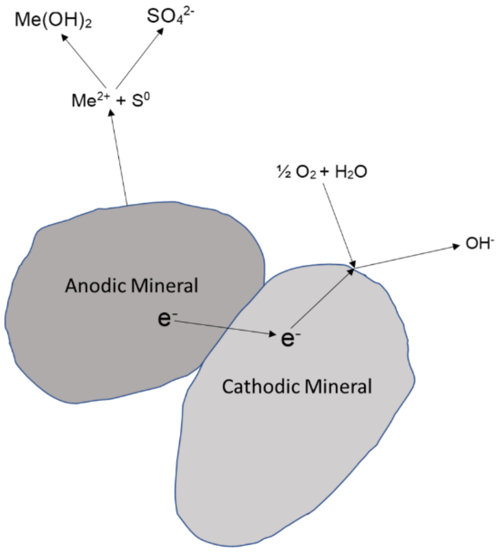

Figure 32. Galvanic interaction between less noble (anodic) and more noble (cathodic) mineral (Becker, 2009)

Table 27 summarizes the rest potential of various sulfide minerals. It should be noted that the measured rest potential varies between the publications because the measurement conditions vary and due to the differences in the unique mineralogy, but the relative ranking is similar (Becker, 2009).

Table 27. Different rest potentials of sulfide minerals (Arpalahti & Lundström, 2018; Becker, 2009; Kwang, 1975)

Mineral	Formula	Rest potential (V vs. SHE)
Pyrite	FeS_2	0.64
Chalcopyrite	CuFeS	0.52
Chalcocite	Cu_2S	0.44
Covellite	CuS	0.42
Galena	PbS	0.28
Sphalerite	ZnS	-0.24
Pyrrhotite	$Fe_{(1-x)}S$	-0.28

Note: rest potentials are measured in approx. 1M H_2SO_4 *solution.*

The leaching order for Aitolampi tailings was estimated to be (from first to last): pyrrhotite, sphalerite, chalcopyrite, and pyrite. The theoretical leaching reaction of metal sulfides in sulfuric acid is shown in equation (9). In the reaction, Me represents the metal (e.g., Ni, Co, Zn, Fe) (Xiao et al., 2021)

$$\mathrm{MeS} + 2\mathrm{H}^+ = \mathrm{Me}^{2+} + \mathrm{H}_2S(g) \qquad (9)$$

In next sections, the leaching experiments' results are presented. First, the focus is put on the total yields and acid consumption, followed by the results related to the first and second sets of experiments.

4.3.1 Leaching yield and acid consumption

In Table 28, leaching yields of the solids, volumes and molarities at the start and the end, and the total acid demand for each experiment are presented.

Table 28. Total solids yields and acid consumption of leaching experiments

Experiment	Molarity start (mol/L)	V start (mL)	Leaching yield of solids (%)	Molarity end (mol/L)	V PLS (mL)	Acid demand (100% H_2SO_4 - g/kg sample)
ART_W_1_1	0.0203	800	5.3	0.0025	670	17.9
ART_W_1_2	0.203	800	12.0	0.10	660	118.2
ART_W_1_3	2.03	800	17.0	1.45	620	888.8
ART_W_2_1	2.03	800	7.0	2.21	730	21.8
ART_W_2_2	2.03	800	19.0	1.91	725	582.2
ART_W_2_3	2.03	800	8.0	2.04	720	192.5
ART_W_2_4	2.03	800	15.9	1.73	730	447.2

Based on the results (see Table 28), the leaching yield of solids varied from 5.3-19%. An increase in molarity had an improving effect on the total leaching yield, which also affected the total acid consumption. Additionally, decreasing the temperature from 90 to 45 °C reduced the yield. Changing the S:L from 100 to 50 g/L had a positive effect on the yield at 90 °C but not at 45 °C. From all the experiments, ART_W_1_3 and ART_W_2_2 had the highest yields, 17% and 19%, respectively.

4.3.2 Leaching at various acid molarities

The results of the first set (ART_W_1_1-3) of experiments are presented in Figures 33–35. The leaching yields of the target elements and the redox potential as SHE in mV are presented as a function of time for each experiment. As shown in Figure 33, in the low molarity acid, the target elements were found to dissolve poorly. Most of the elements reach their maximum yield in the first 30 minutes and are reprecipitated after that. Only the Fe continues to dissolve until the end of the experiment. The redox potential appears to gradually decrease in the first 15 minutes, then stabilize for a moment before decreasing as a function of time.

More interesting results were achieved from 0.2M and 2M leaching experiments (see Figures 34 and 35). When comparing these two figures, Ni and Fe leaching behaviors look similar. In both experiments, Co seems to first dissolve with Fe and Ni. However, at medium acid molarity, the long-term behavior is quite like Zn. Zn has different leaching behavior than Ni and Fe. At medium molarity, the Zn dissolving seems to stop while Fe and Ni continue to dissolve. On the other hand, in high molarity acids, the Zn continues to dissolve, but the yield increases later than with the other elements.

In the first two experiments (see Figures 33 and 34), the redox potential behavior looks quite similar at the start. The main difference is that in the second experiment, the drop after 30 minutes is not as deep as in the first experiment. In the third experiment (see Figure 35), the redox level dropped gradually in the first 15 minutes, after which it increased, reaching 550 mV as more elements, especially Fe, were dissolved.

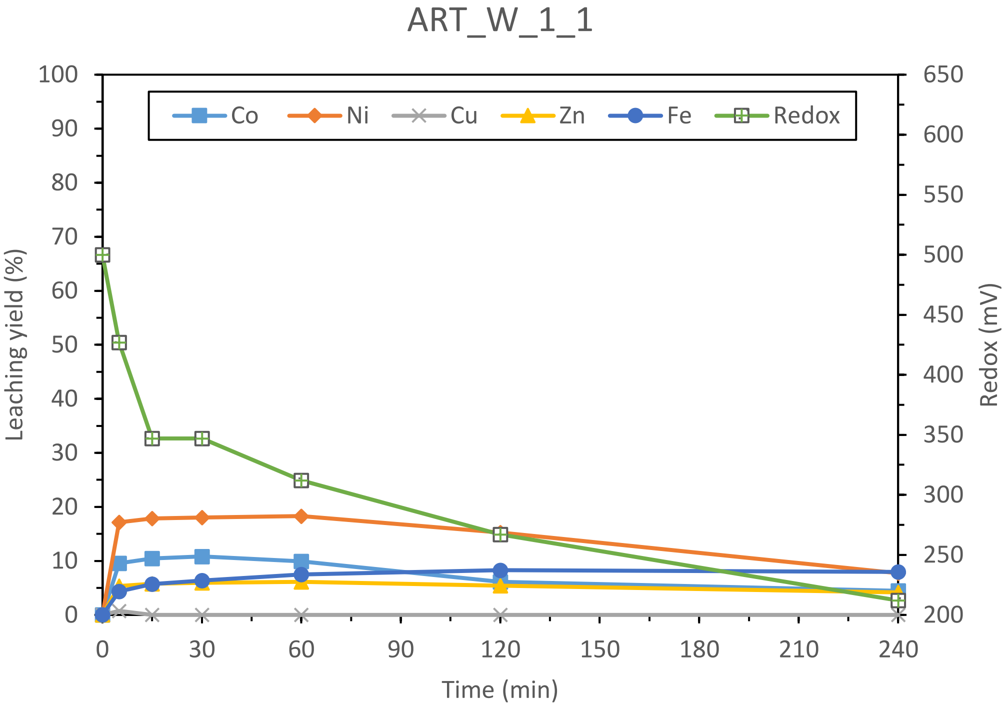

Figure 33. ART_W_1_1: Leaching yields and redox potential as a function of time

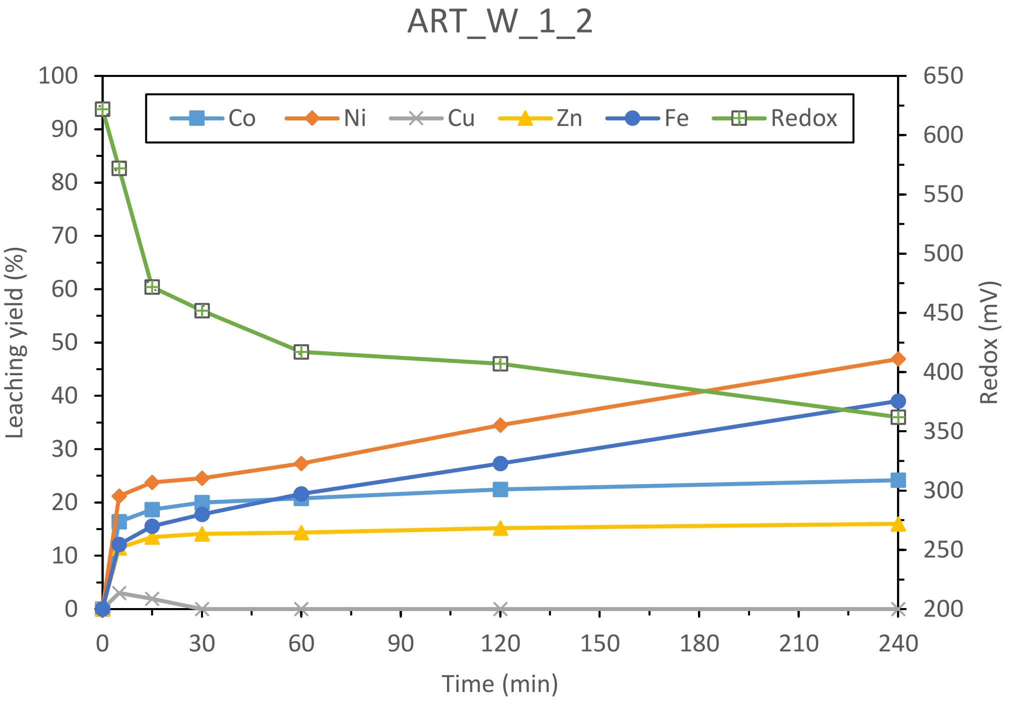

Figure 34. ART_W_1_2: Leaching yields and redox potential as a function of time

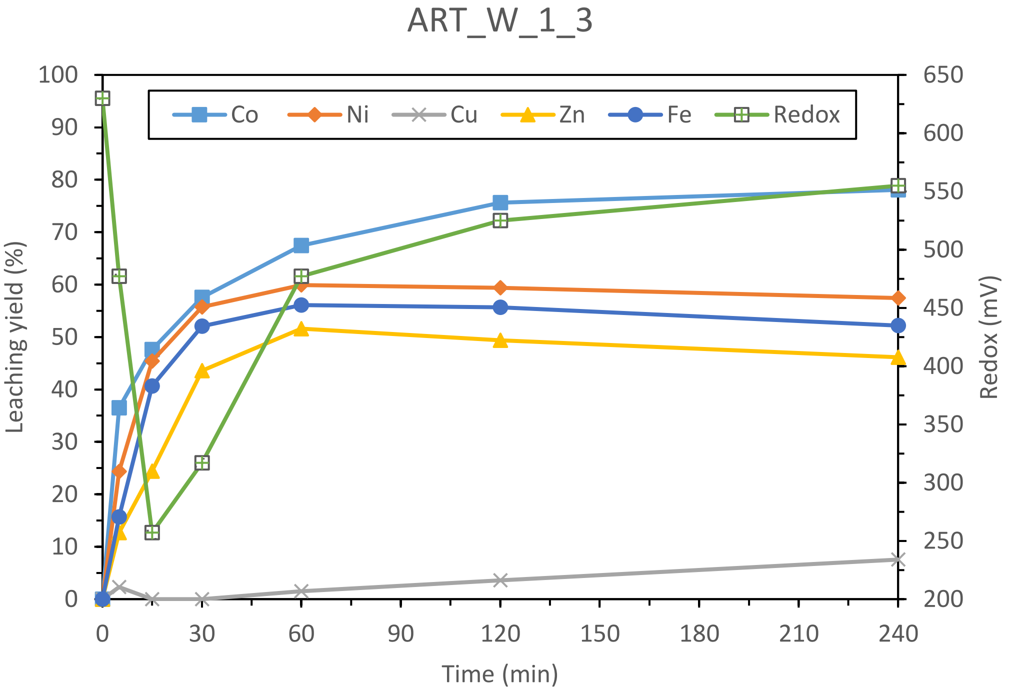

Figure 35. ART_W_1_3: Leaching yields and redox potential as a function of time

In Table 29, the achieved PLS compositions for each experiment are presented.

Table 29. ART_W_1_1–3: PLS composition

Concentration in mg/L			
Element	**ART_W_1_1**	**ART_W_1_2**	**ART_W_1_3**
Co	0.3	1.7	5.7
Ni	3.0	18.7	24.3
Cu	0.0	0.0	3.4
Zn	8.8	34.3	105.3
Fe	700.1	3484.3	4961.1

Based on Table 29, in the first two experiments, no Cu was dissolved, and in the last experiment, only 3.4 mg/L was dissolved. Other elements were found to dissolve in all molarities. The elements' final dissolving rates increased as the acid molarity increased, and the PLS content was dominated by Fe.

4.3.3 Optimization of leaching parameters

The results of the second set (ART_W_2_1-4) of experiments are presented in Figures 36–39. The leaching yields of the target elements and the redox potential as SHE in mV are presented as a function of time for each experiment. As shown in Figure 36, at low temperatures and S:L, the target elements were found to dissolve poorly. Most of the elements reach their maximum yield in 5 minutes. After that, Fe continued to dissolve, and Cu reprecipitated. After 30 minutes, Cu was found to dissolve again. The redox potential appeared to decrease in the first 5 minutes, and after that it stabilized at 625 mV. Different results were achieved by increasing the temperature to 90 degrees (see Figure 37). Fe, Ni, and Co reached their maximum yields in 60 minutes, while Zn continued to dissolve until the end of the experiment. The dissolving behavior of Cu was like in previous experiments, where it first dissolved and then reprecipitated, and afterward it was dissolved in small amounts. The redox potential decreased in the first 15 minutes, after which it increased, reaching 440 mV as more elements, especially Fe, were dissolved.

When comparing Figures 36 and 38, the leaching behavior in each experiment seems quite similar. The main differences are in redox potential. In the third experiment, redox potential first increases and then decreases until it reaches a value of 625 mV, while in the first experiment it stayed quite constant. The most interesting results were achieved from the last experiment (see Figure 39). In the first 5 minutes, the leaching behavior of Fe, Ni, Co, and Zn was similar. Leaching yields of Fe, Ni, and Co did not increase remarkably later. The total yields of Fe and Ni were significantly lower than in previous experiments. When it came to Zn, it continued to dissolve, reaching a maximum yield of 60%. The redox decreased gradually in the first 30 minutes, after which it increased, reaching 440 mV.

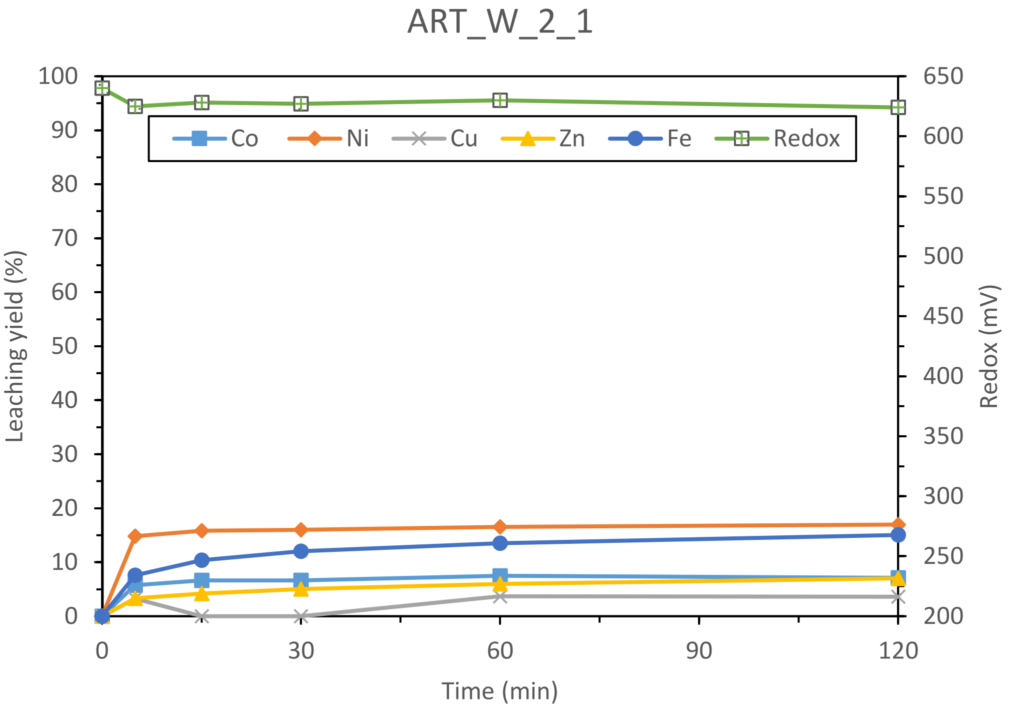

Figure 36. ART_W_2_1: Leaching yields and redox potential as a function of time

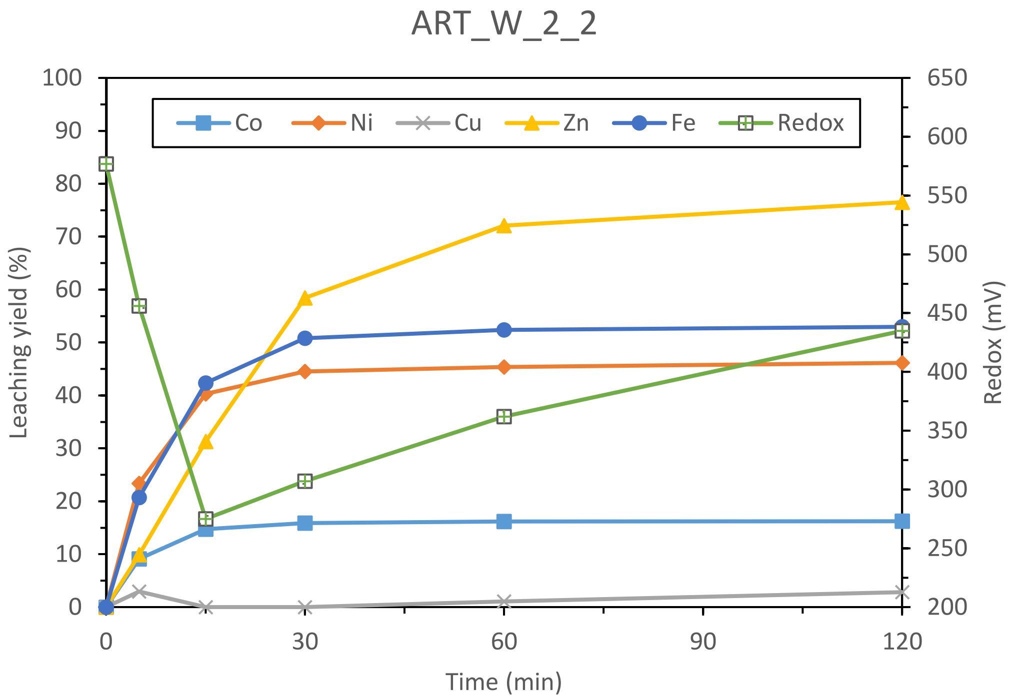

Figure 37. ART_W_2_2: Leaching yields and redox potential as a function of time

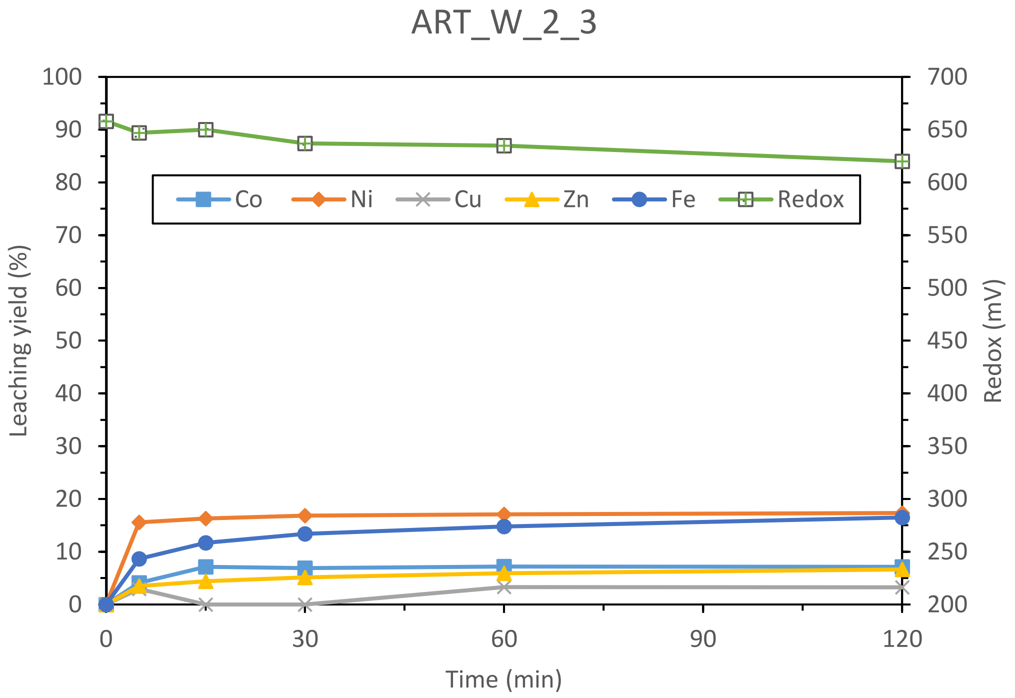

Figure 38. ART_W_2_3: Leaching yields and redox potential as a function of time

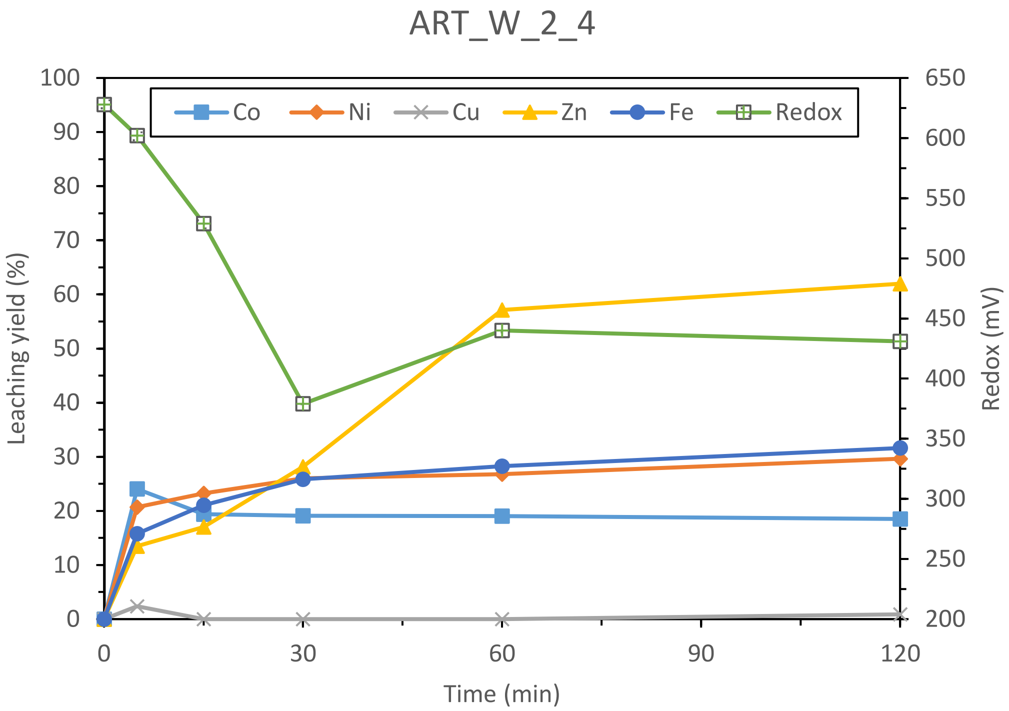

Figure 39. ART_W_2_4: Leaching yields and redox potential as a function of time

The achieved PLS compositions for each experiment are shown in Table 30.

Table 30. ART_W_2_1–4: PLS composition

	Element concentration in mg/L			
Element	**ART_W_2_1**	**ART_W_2_2**	**ART_W_2_3**	**ART_W_2_4**
Co	0.2	0.5	0.4	1.2
Ni	3.1	8.4	6.3	11.1
Cu	0.7	0.6	1.3	0.4
Zn	6.8	74.6	13.0	125.2
Fe	607.0	2152.3	1349.7	2661.5

Based on Table 30, all elements were found to dissolve in all experiments. The lowest concentrations of dissolved elements were found in the first and third PLS. The second and final experiments yielded the highest target element concentrations. For Co, Ni, Cu, Zn, and Fe, the highest values were, in order, 1.2, 11.1, 1.3, 125.2, and 2661.5 mg/L. The elements' final dissolving rates increased as temperature increased for all other elements than Cu.

5 Discussion and possible scenarios

This chapter focuses on discussing the presented results. The discussion is divided into three different subsections: first, the magnetic and gravity separation results are analyzed, and arguments for and against both methods are presented. After that, the leaching results are discussed in the same manner. At the end of each section, the data reliability and possible sources of error are summarized. Finally, possible processing scenarios for graphite mine tailings are reviewed.

5.1 Mechanical processing

The mechanical processing tests were done for both Aitolampi rougher tails East (ART_E) and West (ART_W). Because both raw materials have a somewhat similar bulk content, the discussion will not be done for individual raw materials.

5.1.1 Magnetic separation

Different minerals present in the tailings samples were expected to show different responses to the magnetic separation. As expected, the Fe and S content were highest in the M1 product, recovered by LIMS at 0.07T. This is in line with XRD results (see Appendix 1), where monoclinic magnetic pyrrhotite was detected. It can be concluded that the LIMS 0.07T products mainly consist out of ferromagnetic products like pyrrhotite, and other unliberated minerals like plagioclase and quartz. These other minerals accounted for the lower Fe content when compared to the Fe content of pyrrhotite, which can be as high as 60%. Based on the recovery analysis (see Figure 28), Ni and Co recoveries were found to correlate with Fe recovery. This is in line with EDS results, where Ni and Co were found in solution with pyrrhotite (see Figure 17). What comes to Cu and Zn, these were not recovered well with LIMS.

The lowest recoveries of all the target elements were in the case of MIMS 0.03T. This was primarily due to the recovery of pyrrhotite with Fe, S, and some Ni and Co using LIMS. Following that, MIMS was insufficient to recover minerals containing Cu and Zn. HIMS at 0.5T recovered Zn and Cu. This was due to the iron-rich composition of sphalerite and chalcopyrite. Because both minerals have similar paramagnetic properties and responses to magnetic fields, the Cu recovery trend was correlated with Zn (see Figure 28). SiO_2-containing minerals like quartz and plagioclase represented the major bulk content in both samples (see Figures 13 and 14). As expected, these were mainly recovered as non-magnetic products due to their diamagnetic nature. Some fractions were also recovered with HIMS 0.7T, which was probably due to some paramagnetic interlockings inside SiO_2 phases.

The findings of previous studies on the magnetic properties of sulfide minerals are consistent with the findings of this study's magnetic separation results. Jeong & Kim (2018) found in their study that pyrrhotite can be recovered well with a low-intensity magnetic separator, in their case at 0.2T. Based on Horng (2018), monoclinic pyrrhotite has a good magnetic response to field intensities of 0-0.03T. The high grades of Fe and S in M1 products (see Tables 19–22) confirmed the findings of previous studies. Jeong & Kim (2018) and Jirestig & Forssberg (1992) showed in their studies that sphalerite and chalcopyrite were recovered at similar magnetic intensities from concentrates containing sulfide minerals. Based on the results of Jeong & Kim (2018) both minerals were recovered at intensities higher than 0.4T. The results from magnetic separation tests in this study confirmed these findings. With the magnetic test work, it was confirmed that the Fe and S can be enriched well for small mass products and that the total sulfur can be reduced from the waste stream. Further, the target metals can be enriched, but as the feed grades are low and there are a lot of other gangues present, it is hard to enrich those inside low mass products.

Between ART_E and ART_W, there were some variations in recovery percentages, which are most likely due to the difference in nature between each raw material and the sample preparation. Additionally, when comparing the ICP-MS and XRF analysis results for individual raw materials (Tables 19–20 and 21–22), there are some variations. This could be because XRF is good for analyzing bulk elements. The presence of Fe can therefore cause errors in the detection of other elements with lower concentrations, as in this case for Cu, Ni, Co, and Zn. As the total calculations are based on the analysis performed for products M1, M2, M3, and NM3, even a small numerical change will influence the recovery and grade calculations. Because small amounts of samples are used in analyses (0.25–0.4 g in ICP and 5 g in XRF), sample preparation can also cause some errors. However, as ICP has lower detection limits and better sensitivity, the results obtained there seem more truthful.

5.1.2 Gravity separation

As shown in Table 16, the relative densities of sulfide minerals are higher when compared to other minerals, and therefore the gravity separation was expected to produce good separation results. Fe and S were recovered well, with a high grade in the GSH product. This was mainly due to the relatively high density of pyrrhotite and pyrite when compared to other minerals. As discussed in the previous section, Co and Ni follow Fe recovery. Cu and Zn recoveries were lower, which is due to the lower relative densities of chalcopyrite and sphalerite when compared to pyrite and pyrrhotite. As the GSH product total mass was small, moderate grades were achieved for target elements.

A major part of the total feed ended up going to GSM and GSL products. Even though the target elements' recoveries were highest in the GSM, the grades were lost as other bulk minerals ended up there. This might be due to the fact that a major part of the raw material is fine-grained, and therefore small metallic particles are mixed with non-metallic gangue. The same effect happened with GSL, but on a smaller scale (see Figure 31). From the results, it becomes clear that the shaking table did not have so much overall selectivity in the recovery and that a lot of potential was lost due to the mixture problem with bulk gangue.

5.2 Leaching experiments

The leaching order of sulfidic minerals was estimated to be (from first to last): pyrrhotite, sphalerite, chalcopyrite, and pyrite. Based on the results, this was confirmed. In all the experiments, Fe dissolved from the very beginning, which indicates that the pyrrhotite was leached first. Furthermore, the sharp decrease in redox potential, for example in Figure 35, indicates that pyrrhotite, a major oxygen sink, was oxidized and the redox potential of the solution was gradually decreased. The leaching of sphalerite started after pyrrhotite, which is shown as the dissolution of Zn, which starts later than Fe dissolution. The leaching of sphalerite was followed by chalcopyrite, which is shown as a slowly increasing dissolution of Cu. Even though the leaching order was as expected, the rest potentials of sulfide minerals were not the same as shown in Table 27. This is mainly since measurement conditions vary and due to the differences in the unique mineralogy (Becker, 2009).

Next, the dissolution of target metals is discussed. Based on the results, the Fe and Ni leaching behavior was similar (e.g., see Figures 34 and 35), which is because pyrrhotite was the primary source of both. Therefore, selective dissolution of Fe and Ni is not possible, and separation would have to occur at a later stage of the process. However, the dissolved Fe increased the oxidative power as Fe^{2+} was oxidized to Fe^{3+}, which is a strong oxidizing agent capable of gaining electrons and oxidizing noble minerals like chalcopyrite. The rest of the Fe and Ni that didn’t dissolve was expected to be in the form of pyrite, chalcopyrite, and other refractory minerals.

As it can be seen from Figure 34, Zn has different leaching behavior when compared to Fe, which is in line with SEM-EDS results where Zn was found mainly present in more noble sphalerite (see Figure 18). In the case of a 0.2 M lixiviant (see Figure 34), Zn dissolution does not increase when compared to Fe and Ni, which are mainly present in pyrrhotite. It can be concluded that at low molarities, there is a small amount of acid dissolvable Zn, but there is not enough oxidative leaching capable of leaching sphalerite at that pH.

As it was concluded in the results, Co does not seem to go hand in hand either with Ni or Zn. According to the EDS analysis, Co was found hosted in pyrrhotite and also in biotite (see Figures 17 and 19). The results indicate that most Co must be in biotite and therefore the leaching is not effective. At low acid levels, the leaching behavior is quite similar to Zn when it is not supported by the oxidative power as a function of time. This indicates that in low molarity acid, Co present in pyrrhotite is dissolved only. Cu did not dissolve well in low molar acid levels. This supports the results of EDS analysis (see Figure 19) that the Cu must be mainly present in refractory minerals like chalcopyrite. Therefore, Cu does not dissolve or dissolves in small amounts when other less noble minerals have dissolved and Fe^{3+} has entered the solution and works as a strong oxidizing agent.

According to the results of experiment ART_W_1_3, there is no significant increase in metal leaching yield after 120 minutes. It is reasonable to conclude that the majority of the leachable minerals, primarily sulfide minerals, are dissolved during that time. The total metal yields increased as the acid molarity increased, as expected. This was due to the concentration effect on an increasing amount of H^+, which caused further dissolution of minerals, as shown in equation (9). Additionally, when using 2M H_2SO_4, increasing the temperature and decreasing the solid to liquid ratio both had a positive effect on the leaching kinetics (see Table 28). The maximum solids leaching yield of 19% was obtained after 120 minutes of strong acid (2M H_2SO_4) leaching at 90 degrees with a solid to liquid ratio of 50 g/L.

Due to the poor grades of valuable metals in the raw material and the fact that everything cannot be dissolved, the Cu, Ni, Co, and Zn concentrations in PLS seem not to be high enough to be economical. As a result, leaching does not appear to be a suitable recovery method for bulk tailings in this study. Some variation in the leaching yield of some metals was observed between experiments where the only changed parameter was time (see Figures 35 and 39), i.e., the results should have been repetitive. As in any experimental work, there are always multiple sources of error. During the experiments, some solids adhered to the redox and pH probes, resulting in a notable error. Also, because of the harsh reaction conditions, the probes were not kept in the solution all the time to prevent degradation. During the experiment, some evaporation occurred, especially while sampling, which enriched the level of metals in the solution. Furthermore, the timing of the sampling was not constant between the experiments. When it comes to the handling of the solids, minor errors could originate from weighing and pouring.

Together with errors that can occur during leaching experiments, some errors could also originate from sample preparation and analysis. For example, the bulk sample was divided into sub-batches by using a sample divider, which does not ensure a 100% similar nature between batches. There might be some higher concentrations of different minerals and metals in other samples, which can create variations in the end results. The yield calculations were based on the bulk raw material ICP-MS results and AAS analysis results. As the individual sub-batches were not analyzed for chemical composition, concentrated fractions can show higher or lower yields of target elements.

5.3 Processing scenarios for Aitolampi tailings

In this section, the possible processing scenarios for Aitolampi tailings are discussed. In the tailings, the concentrations of sulfidic sulfur are remarkably higher than the trace metals. From both an environmental and circular economy point of view, it seems more beneficial to recover the sources of sulfidic sulfur, like pyrrhotite, first. Based on the results, magnetic separation seemed to be a more effective method to reduce sulfur content in the Aitolampi rougher tails in comparison to gravity separation (see Tables 20, 22, 24, and 26). The performance of LIMS 0.07T is the main key to good sulfur and iron recovery. Based on the results (see Tables 19 and 21), it is possible to produce high-grade concentrate with an Fe grade of 47.1 to 52.2% and an S grade of 32.4 to 34.6%. This type of concentrate is, in theory, a suitable feed material to be used in pyrite or pyrrhotite roasting to produce sulfuric acid. Examples of the concentrate types and existing roasting plants are shown in Tables 31 and Table 32.

Table 31. Types of concentrate suitable for roasting (Runkel & Sturm, 2009)

Type	Composition	Grain size
Pyrite concentrate	S 47-48 wt%; Fe 42-43 wt%	fine particles 55% < 45 µm
Coarse pyrite	S 47-48 wt%; Fe 42-43 wt%	coarse particles 0 - 6 mm
Pyrrhotite concentrate	S 34-38 wt%; Fe 50-54 wt%	fine particles 55% < 45 µm
Coarse pyrrhotite	S 28-29 wt%; Fe 47-50 wt%	coarse particles 0 - 4 mm

Table 32. Example of the roasting plants (Runkel & Sturm, 2009)

Location	Kalgoorlie, Australia	Bandrima, Turkey	Tongling, China
Roaster type	Circulating Fluid Bed Roasting	Stationary Fluid Bed Furnace	Stationary Fluid Bed Furnace
Raw material	flot. Pyrite	flot. Pyrite	flot. Pyrite and pyrrhotite
S content in Feed	33 wt%	48 wt%	37 wt%
Capacity	575 tons per day	650 tons per day	1130 tons per day
Acid production	-	750 tons per day	1200 tons per day
Power consumption of roasting	1000 kW	1250 kW	1400 kW

The main issue with gravity separation GSH products (e.g., see Tables 23 and 25) was that both target metals and sulfidic sulfur were concentrated there. Because of this, the grade of valuable metals decreased, and it did not seem like a good candidate for later metal recovery. The blending problem can now be mitigated because the Fe and S can be recovered selectively prior to gravity separation. Additionally, as in GSM and GSL, the trace element concentrations were low; a mixture of both seems like a good tailings' candidate. Figure 40 illustrates a flowchart of the possible process. The abbreviations are explained in Tables 13 and 15.

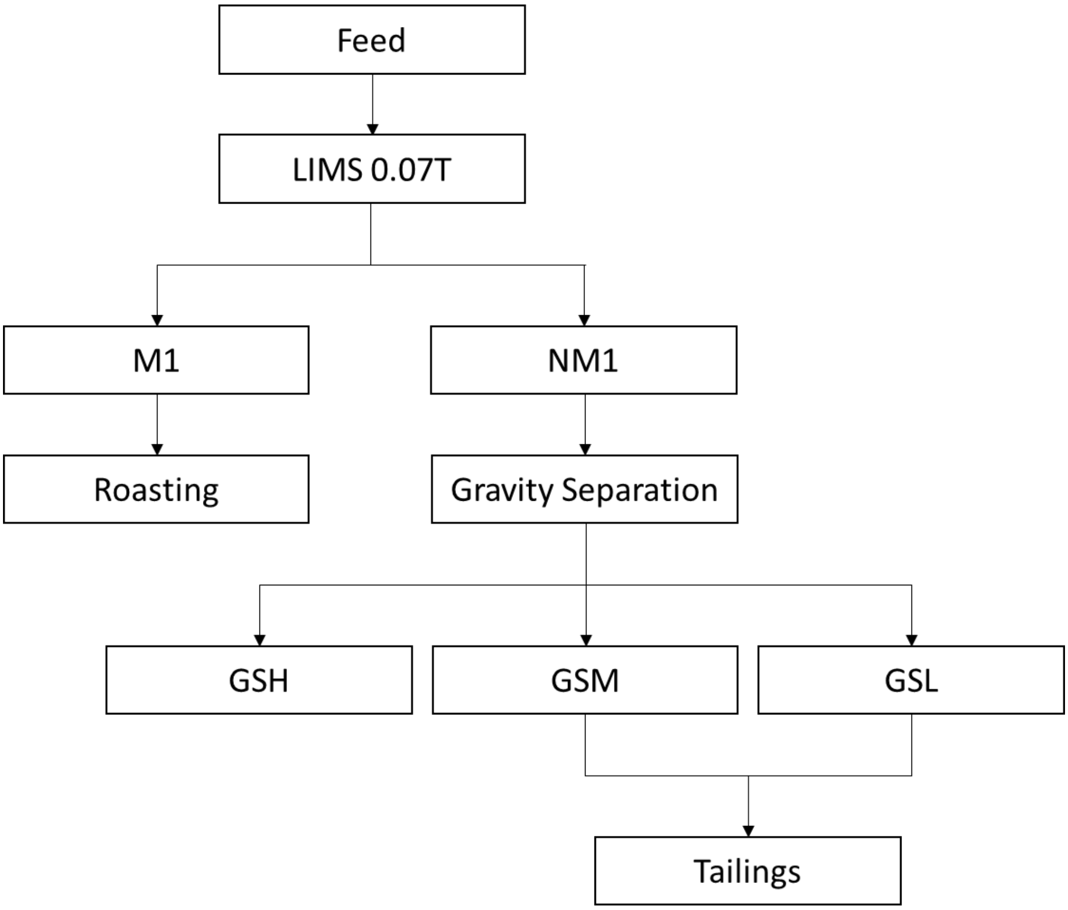

Figure 40. Flowchart of the combined process using magnetic and gravity separation

By implementing the achieved recovery percentages (see Tables 19–26), it is possible to calculate the theoretical recoveries of the process for each studied element when bulk raw material (see Tables 9 and 10) is used as feed. In Appendix 6, the theoretical grades and mass pull of each product are presented when bulk ART_E and ART_W are used as feed materials in the flowchart shown in Figure 40. The summaries for S, Fe, Cu, Ni, Co, and Zn are presented in Tables 33 and 34.

Table 33. ART_E: Possible grades in the process products shown in Fig. 40.

Product	% of the total feed	Leco S (wt%)	Fe (ICP-MS) (wt%)	Cu (ICP-MS) (wt%)	Ni (ICP-MS) (wt%)	Co (ICP-MS) (wt%)	Zn (ICP-MS) (wt%)
Feed	100	4.2	7.0	0.01	0.04	0.004	0.09
M1	7.4	32.6	57.2	0.03	0.4	0.02	0.05
NM1	92.6	1.9	3.0	0.01	0.02	0.00	0.10
GSH	7.5	12.9	15.9	0.02	0.1	0.01	0.3
GSM	67.6	1.0	1.8	0.01	0.01	0.001	0.1
GSL	17.5	0.9	2.0	0.01	0.01	0.001	0.1

Note that in calculations, feed material assay and recovery results based on ICP-MS analysis were used.

Table 34. ART_W: Possible grades in the process products shown in Fig. 40.

Product	% of the total feed	Leco S (wt%)	Fe (ICP-MS) (wt%)	Cu (ICP-MS) (wt%)	Ni (ICP-MS) (wt%)	Co (ICP-MS) (wt%)	Zn (ICP-MS) (wt%)
Feed	100.0	4.5	7.4	0.04	0.03	0.006	0.18
M1	8.5	33.6	35.9	0.06	0.25	0.02	0.02
NM1	91.5	1.7	4.7	0.03	0.01	0.004	0.2
GSH	6.9	9.8	20.6	0.07	0.06	0.02	0.6
GSM	58.0	1.2	3.4	0.03	0.01	0.003	0.1
GSL	26.6	0.9	3.3	0.04	0.01	0.003	0.2

Note that in calculations, feed material assay and recovery results based on ICP-MS analysis were used.

Based on the results (see Tables 33 and 34), S and Fe can be enriched well in M1 product with a high enrichment ratio i.e., product grade divided by feed grade. When it comes to Cu and Ni, those can be enriched by a ratio of approximately two in GSH product. Co and Zn, on the other hand, can be enriched by a factor of more than three in GSH product. This makes GSH an interesting candidate as a source for metals like Cu, Ni Co, and Zn. As it was shown in the leaching experiments, the sulfide minerals and, therefore, target metals were dissolvable with varying degrees of success. One of the main problems was that, together with valuable metals, Fe was dissolved. As the high amount of Fe can be recovered in previous stages before gravity separation, and the target metals can be enriched in GSH, leaching of this kind of product might give better outcomes.

Some tailings are always created as everything cannot be recovered. One of the focus points of this study was whether it was possible to decrease the environmental impact. In Figure 40, GSM and GSL are combined and deposited as tailings. To analyze the environmental impact, natural concentrations and threshold values for metals and semimetals (see Table 8.) determined by the Finnish Government were introduced in section 2.5. Additionally, the limits of sulfidic sulfur were introduced in the same section. To see what can in theory be achieved, a comparison was made between threshold values, studied raw materials ART_E and ART_W, and theoretical end tailings (GSM + GSL) when the tailings are processed (see Table 35).

Table 35. Processed tailings vs. threshold values determined by the Finnish Government (2009)

Based on Finnish Government (2009)			Raw material in mg/kg; ppm		GSM+GSL tailings in mg/kg; ppm		Percentage change	
Metals and semimetals	Natural concentration (mg/kg; ppm)	Threshold value(mg/kg; ppm)	ART_E	ART_W	ART_E	ART_W	ART_E	ART_W
Sb	0.02	2	110	100	114	102	3.6 %	2.2 %
As	1	5	5	7	4	5	-10.8 %	-25.3 %
Hg	0.005	0.5	0	0	-	-	-	-
Cd	0.03	1	9	20	7	17	-18.4 %	-13.9 %
Co	8	20	36	57	13	27	-64.9 %	-51.9 %
Cr	31	100	125	144	97	157	-22.6 %	9.1 %
Cu	22	100	103	353	76	301	-25.8 %	-14.8 %
Pb	5	60	28	32	26	28	-4.5 %	-12.8 %
Ni	17	50	234	328	56	93	-75.9 %	-71.7 %
Zn	31	200	920	1768	774	1564	-15.8 %	-11.5 %
V	38	100	430	730	477	814	11.0 %	11.4 %
Leco S	-	1000	41900	44500	9504	10866	-77.3 %	-75.6 %

Note: In terms of concentration in ART_E or ART_W, ICP-MS data were used for elements other than Sb and V

According to Table 35, three largest percentage decreases are in the cases of S, Ni, and Co. What is remarkable is that over 75% of the sulfidic sulfur could be recovered. For As, Cd, Co, Cr, Cu, Pb, and Zn, the percentage change varies from +9% to -25.8%. It should be noted that V is contracted to the tailings, primarily because it is not recovered with LIMS and enriches into GSM and GSL products. There is some uncertainty in the results for Sb, as with SEM, the host mineral phase or presence of Sb were not recognized, and thus it could be an XRF analysis error. When these aspects are considered, threshold values could be achieved, depending on the raw material, in the case of As, Co, Cr, Cu, and Pb. Table 36 shows the GAI (see section 4.1.2) calculated for the combined tailings product.

Table 36. The processed tailings' Geochemical Abundance Index

Element	GAI: ART_E	GAI: ART_W
Sb	5.83	5.67
As	< 0	< 0
Hg	-	-
Cd	2.87	4.11
Co	< 0	0.44
Cr	< 0	0.66
Cu	< 0	1.59
Pb	< 0	< 0
Ni	0.17	0.89
Zn	1.95	2.97
V	2.26	3.02

When comparing Tables 36 and 18. together, it could be possible to mitigate the risk of soil contamination. After processing in ART_E, only Sb, Cd, Ni, Zn, and V can pose a risk. In the case of ART_W, other elements than As and Pb can pose a risk. The risk of AMD can be theoretically estimated. From each product sulfur and carbon Leco analyzes, theoretical end values can be calculated (see Appendix 6). From the Leco carbon concentration, NP can be calculated by multiplying the carbon concentration by 83.34. Additionally, AP can be calculated by multiplying the sulfur concentration by 31.25. Therefore, with NP and AP, NPR can be calculated (see section 2.5) (Price, 2010; Kauppila, 2019). Theoretical NPR values for processed tailings accumulated from ART_E and ART_W are presented in Table 37.

Table 37. Theoretical NPR of processed tailings

Raw material	NP	AP	NPR
ART_E	0.30	0.30	1.00
ART_W	0.37	0.34	1.10

Based on the results (see Table 37), an NPR of one or higher can be achieved. When compared to unprocessed tailings where the NPR was lower than 0.1, the ratio can potentially tenfold, and processed tailings could be classified as uncertain (Price, 2010). The visualization of potential NPR improvement is presented in Figure 41.

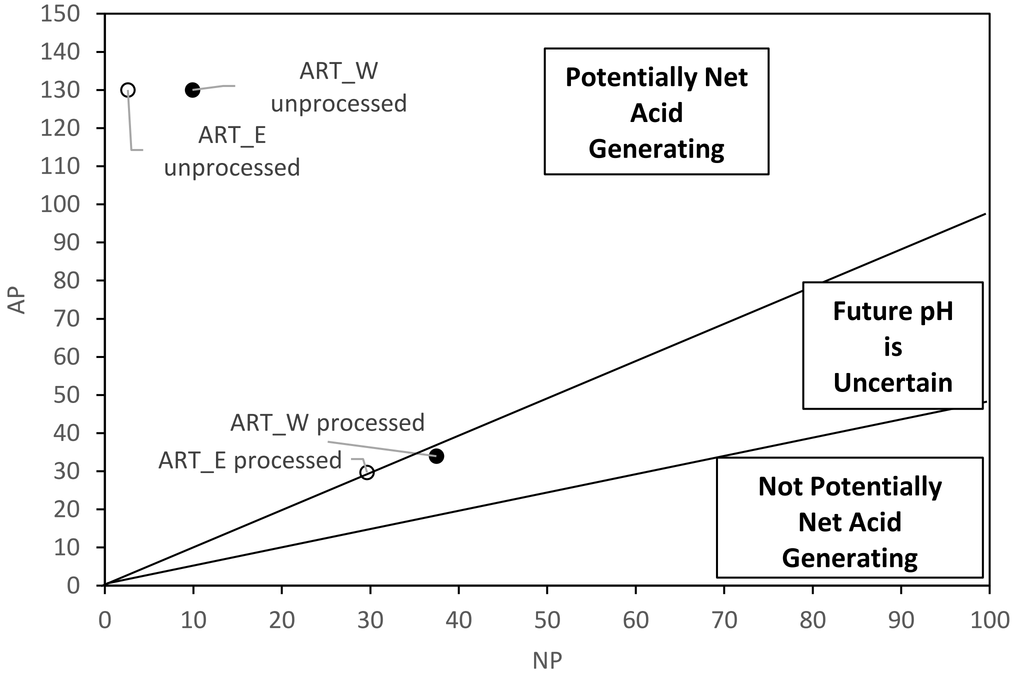

Figure 41. NPR and AMD classification of unprocessed and processed tailings (based on Price, 2010)

When it comes to leaching, it does not seem like the best option for target metal recovery from unprocessed tailings. In leaching, both leachate and residues are created, and for both products, there is a need for extra treatment. For example, when the sulfide minerals are leached, there is a formation of elemental sulfur, which creates an AMD problem in the leaching residues, and therefore there would be a need for extra neutralization and separation stages. Further, during the leaching, some H_2S gas is generated, which needs to be controlled. More about the leaching processes and elemental sulfur removal in the case of Cu and Zn sulfides is discussed in Jorjani & Ghahreman (2017). The low grades of valuable metals in raw materials lead to the conclusion that leaching of the unprocessed tailings is not economically viable. Therefore, more focus should be put on the processing stage, where product grades can be improved.

6 Conclusions and recommendations

The potential to decrease the environmental impact of graphite mine tailings and the possibility to use the tailings as a secondary source of raw materials, especially battery metals, were investigated. As it becomes clear from the literature review, the demand for battery raw materials, especially graphite, is expected to grow. Additionally, not all the graphite demand can be fulfilled by synthetic graphite, so natural graphite from mines is needed. Nevertheless, mining always raises concerns in the local community, which should be taken into account. In tailings, there can be multiple harmful elements present, like sulfidic sulfur, which can cause acid mine drainage and other environmental risks. By looking at these aspects from a circular economy point of view, the difficulties can be transformed into opportunities. For example, tailings can work as a secondary source of valuable metals. In this study, both tailing samples showed high potential to generate acid mine drainage. Further, sulfidic sulfur and metal and semimetal concentrations exceeded the threshold limits of inert waste.

To discover the opportunities, test work and experiments with tailings were carried out. The leaching order of the sulfide minerals pyrrhotite, sphalerite, chalcopyrite, and pyrite were confirmed by leaching experiments. However, the concentrations of Co, Ni, Cu, and Zn in the raw materials were too low and Fe was too high to be economically viable. Mechanical test work confirmed that monoclinic pyrrhotite, which is the main source of iron and sulfidic sulfur, can be recovered with a low-intensity magnetic separator. This enables the use of non-magnetic products as feed in gravity separation, where, for example, sphalerite and chalcopyrite can be concentrated with a better enrichment ratio, and the grade of valuables can be increased. The results also showed that, from an environmental point of view, the impact of tailings can be decreased as sulfidic sulfur can be recovered. Based on the findings, multiple opportunities for further investigation were identified, which are summarized below.

This work has the potential to be applied to future work in industrial site rehabilitation or studies involving similar mineralization or rock types such as black schist. The report and its results could be used as a starting point in planning how the valuable metals' recovery could be increased and how to recover minerals that have acid potential.

With a low-intensity magnetic separator, it is possible, in theory, to create a concentrate suitable to be used in roasting to produce sulfuric acid, and this should be studied more. Pyrite and pyrrhotite roasting are well-known processes, and for example, in Finland, Yara Siilinjärvi uses pyrite as a feed material in their acid production.

Based on the results of individual separation test work, the tailings concentration process using magnetic and gravity separation (see Figure 42) was simulated. Real-world combined test work should be performed to confirm these findings. An AMD test should be performed for the products that are classified as tailings.

Pyrometallurgy and/or hydrometallurgy are needed to recover the valuables. Therefore, more attention should be paid to processing test work to see whether the grade of metals of interest can be improved in products using various techniques.

More about the leaching behavior was learned. The knowledge can be used in future leaching experiments when the processing tests have given more promising results. Furthermore, the knowledge can be applied in leaching experiments with tailings that originate from similar types of mineralization or rock types (e.g., black schist).

Based on the literature survey (see section 2.2.2), the grade of graphite concentrate was, in some studies, increased when leaching was done prior to flotation. Therefore, some leaching experiments should be performed on ore samples prior to the beneficiation process to see how that affects the tailings quality.

References

Aalto, P. (2021). *Electrification: Accelerating the Energy Transition (1st ed.)*. Academic Press.

Abdelbaky, M., Peeters, J. R., den Eynde, S. V., Zaplana, I., & Dewulf, W. (2022). A Comparative Assessment of Resource-use Criticality in Advanced Lithium-ion Battery Technologies. *Procedia CIRP, 105, 7–12*. doi:https://doi.org/10.1016/j.procir.2022.02.002

Abdollahifar, M., Doose, S., Cavers, H., & Kwade, A. (2022). Graphite Recycling from End-of-Life Lithium-Ion Batteries: Processes and Applications. *Advanced Materials Technologies, 2200368*. doi:https://doi.org/10.1002/admt.202200368

Al-Ani, T., Leinonen, S., Ahtola, T., & Salvador, D. (2020). High-Grade Flake Graphite Deposits in Metamorphic Schist Belt, Central Finland—Mineralogy and Beneficiation of Graphite for Lithium-Ion Battery Applications. *Minerals, 10(8), 680*. doi:https://doi.org/10.3390/min10080680

ALS. (2021). Aqua Regia or 4 Acid Digestion.

Amira International. (2002). *ARD Test Handbook: Prediction & Kinetic Control of Acid Mine Drainage, AMIRA P387A*. Melbourne: Ian Wark Research Institute and Environmental Geochemistry International Ltd.

Andersen, H. F., Foss, C. E., Voje, J., Tronstad, R., Mokkelbost, T., Vullum, P. E., . . . Mæhlen, J. P. (2019). Silicon-Carbon Composite Anodes From Industrial Battery Grade Silicon. *Scientific Reports, 9(1)*. doi:https://doi.org/10.1038/s41598-019-51324-4

Arachchige, M. P., Rohitha, S., Dissanayake, K., Lakshitha, P., & Kusumsiri, R. (2021). Upgrading Low-Grade Graphite Tailing into High-Grade Graphite Using Agglomeration. *2021 Moratuwa Engineering Research Conference (MERCon)*. doi:https://doi.org/10.1109/mercon52712.2021.9525795

Arpalahti, A., & Lundström, M. (2018). The Leaching Behavior of Minerals From a Pyrrhotite Rich Pentlandite Ore During Heap Leaching. *Minerals Engineering, 199, 116-125*. doi:https://doi.org/10.1016/j.mineng.2018.01.025

Becker, M. (2009). The Mineralogy and Crystallography of Pyrrhotite From Selected Nickel and PGE Ore Deposits.

Benchmark. (2022). *More Than 300 New Mines Required to Meet Battery Demand by 2035*. Retrieved from https://www.benchmarkminerals.com/membership/more-than-300-new-mines-required-to-meet-battery-demand-by-2035/

Benchmark Mineral Intelligence. (2017). *China is Constructing Graphite Anode Megafactories for the Lithium Ion Battery Surge*. Retrieved from https://www.benchmarkminerals.com/china-is-constructing-four-graphite-anode-megafactories-for-the-lithium-ion-battery-surge/

Beowulf Mining. (2022). *Aitolampi - Graphite*. Retrieved March 14, 2022, from https://beowulfmining.com/projects/finland/aitolampi/#overview

Blagoeva, D., Pavel, C. C., Wittmer, D., & Huisman, J. (2019). Materials Dependencies for Dual-use Technologies Relevant to Europe's Defence Sector. doi:10.2760/570491

BloombergNEF. (2021). Global Graphite Outlook 2021-2030: China's Dominance Unchallenged.

Blowes, D. W., Ptacek, C. J., Jambor, J. L., Weisener, C. G., Paktunc, D., Gould, W. D., & Johnson, D. B. (2014). The Geochemistry of Acid Mine Drainage. doi:10.1016/B978-0-08-095975-7.00905-0

Bogdanov, D., Ram, M., Aghahosseini, A., Gulagi, A., Oyewo, A. S., Child, M., . . . Breyer, C. (2021). Low-cost Renewable Electricity as the Key Driver of the Global Energy Transition Towards Sustainability. *Energy, 227, 120467*. doi:https://doi.org/10.1016/j.energy.2021.120467

BP. (2022). *Raw Data on Energy Consumption*. Retrieved from https://www.bp.com/en/global/corporate/energy-economics/statistical-review-of-world-energy.html.

Brownscombe, W., Ihlenfeld, C., Coppard, J., Hartshorne, C., Klatt, S., Siikaluoma, J., & Herrington, R. (2015). The Sakatti Cu-Ni-PGE Sulfide Deposit in Northern FInland. *Mineral Deposits of Finland, 211–252*. doi:https://doi.org/10.1016/b978-0-12-410438-9.00009-1

Buechel, C., Bednarski, L., & Wietlisbach, S. (2021). As Lithium-ion Battery Materials Evolve, Suppliers Face New Challenges. *IHS Markit*. Retrieved from https://ihsmarkit.com/research-analysis/lithiumion-battery-materials-evolve-suppliers-face-new-challenges.html

Bund für Umwelt und Naturschutz Deutschland, C-461/13 (Court of Justice of the European Union 2015). Retrieved from https://curia.europa.eu/juris/liste.jsf?num=C-461/13

Chandrasekaran, S., Basak, T., & Srinivasan, R. (2013). Microwave Heating Characteristics of Graphite Based Powder Mixtures. *International Communications in Heat and Mass Transfer, 48, 22–27*. doi:https://doi.org/10.1016/j.icheatmasstransfer.2013.09.008

Chehreh Chelgani, S., Rudolph, S., Kratzsch, R., Sandmann, D., & Gutzmer, J. (2015). A Review of Graphite Benefication Techniques. *Mineral Processing and Extractive Metallurgy Review, 37(1),* 58-68. doi:https://doi.org/10.1080/08827508.2015.1115992

Chombo, P. V., & Laoonual, Y. (2020). A Review of Safety Strategies of a Li-ion Battery. *Journal of Power Sources, 478, 228649*. doi:https://doi.org/10.1016/j.jpowsour.2020.228649

Corrosionpedia. (2018). *Electrochemical Corrosion Potential (Rest Potential)*. Retrieved from https://www.corrosionpedia.com/definition/6498/electrochemical-corrosion-potential-rest-potential

Council of the European Union. (2000). Water Framework Directive, Directive 2000/60/EC. Retrieved from http://data.europa.eu/eli/dir/2000/60/oj

Damm, S., & Zhou, Q. (2020). Supply and Demand of Natural Graphite. *DERA Rohstoffinformationen*. Retrieved from https://www.deutsche-rohstoffagentur.de/DERA/DE/Downloads/Studie%20Graphite%20eng%202020.pdf?__blob=publicationFile&v=3

Diekmann, J., Hanisch, C., Froböse, L., Schälicke, G., Loellhoeffel, T., Fölster, A., & Kwade, A. (2016). Ecological Recycling of Lithium-Ion Batteries from Electric Vehicles with Focus on Mechanical Processes. *Journal of The Electrochemical Society, 164(1), A6184–A6191*. doi:https://doi.org/10.1149/2.0271701jes

Downing, B. W. (2014). Acid-Base Accounting Test Procedures. *Acid Mine Drainage, Rock Drainage, and Acid Sulfate Soils, 229–252*. doi:https://doi.org/10.1002/9781118749197.ch20

EERE (Office of Energy Efficiency & Renewable Energy). (2017). *How Does a Lithium-ion Battery Work?* Retrieved from https://www.energy.gov/eere/articles/how-does-lithium-ion-battery-work

Elkem. (2018). *Elkem Silicon in Lithium-ion Batteries*. Retrieved from https://www.elkem.com/sustainability/our-stories/elkem-silicon-in-lithium-ion-batteries/

EU. (2019). *Introduction to the EU Water Framework Directive*. Retrieved from https://ec.europa.eu/environment/water/water-framework/info/intro_en.htm

EU. (2022). *Circular Economy: Definition, Importance and Benefits*. Retrieved from https://www.europarl.europa.eu/news/en/headlines/economy/20151201STO05603/circular-economy-definition-importance-and-benefits

European Commission. (2021). *Strategic Dependencies and Capacities*. Retrieved from https://ec.europa.eu/info/sites/default/files/swd-strategic-dependencies-capacities_en.pdf

Fahl, S. (2017). Natural Graphite: Occurence, Mining and Processing. *Bachelor's Thesis, RWTH Aachen University*.

Fernley, M. (2020). Battery Materials Explained. *Battery Materials Review*, 8-10.

Finnish Government. (2007). Government Decree on the Assessment of Soil Contamination and Remediation Needs 214/2007. Finnish Government, Helsinki, FInland. Retrieved from www.finlex.fi/fi/laki/kaannokset/2007/en20070214.pdf

Finnish Government. (2013). Government Decree on Extractive Waste 190/2013. Finnish Government, Helsinki, Finland. Retrieved from https://www.finlex.fi/fi/laki/kaannokset/2013/en20130190_20150102.pdf

Finnpulp Oy, KHO:2019:166 (Supreme Administrative Court of Finland 2019). Retrieved from https://www.kho.fi/fi/index/paatokset/vuosikirjapaatokset/1576670299837.html

Florena, F. F., Syarifuddin, F., Hanam, E. S., Trisko, N., Kustiyanto, E., Enilisiana, E., . . . Arinton, G. (2016). Floatability Study of Graphite Ore from Southeast Sulawesi (Indonesia). *AIP Conference Proceedings*. doi:https://doi.org/10.1063/1.4941888

Gao, S., Gong, X., Liu, Y., & Zhang, Q. (2018). Energy Consumption and Carbon Emission Analysis of Natural Graphite Anode Material for Lithium Batteries. doi:https://doi.org/10.4028/www.scientific.net/MSF.913.985

Grafintec. (2021). *Anode Materials*. Retrieved from https://www.grafintec.fi/en/anode-materials/

Guo, Y., Smith, R. B., Yu, Z., Efetov, D. K., Wang, J., Kim, P., . . . Brus, L. E. (2016). Li Intercalation into Graphite: Direct Optical Imaging and Cahn–Hilliard Reaction Dynamics. *The Journal of Physical Chemistry Letters, 7(11), 2151–2156*. doi:https://doi.org/10.1021/acs.jpclett.6b00625

Haldar, S. (2013). Mineral Processing. *Mineral Exploration*, 223-250. doi:https://doi.org/10.1016/B978-0-12-416005-7.00012-X

Henderson, L. (2018). *Acid Mine Drainage: Chemistry, Effects and Treatment*. Macmillan Publishers.

Horng, C. S. (2018). Unusual Magnetic Properties of Sedimentary Pyrrhotite in Methane Seepage Sediments: Comparison With Metamorphic Pyrrhotite and Sedimentary Greigite. *Journal of Geophysical Research: Solid Earth, 123(6), 4601–4617*. doi:https://doi.org/10.1002/2017jb015262

IEA. (2021). Growth in Demand for Selected Battery-elated Minerals from Clean Energy Technologies in 2040 Relative to 2020 Levels by Scenario. Retrieved from https://www.iea.org/data-and-statistics/charts/growth-in-demand-for-selected-battery-related-minerals-from-clean-energy-technologies-in-2040-relative-to-2020-levels-by-scenario

IEA. (2021). The Role of Critical Minerals in Clean Energy Transitions. Retrieved from https://www.iea.org/reports/the-role-of-critical-minerals-in-clean-energy-transitions

IEA. (2022). *Global Supply Chains of EV Batteries*. Retrieved from https://www.iea.org/reports/global-supply-chains-of-ev-batteries

IEA. (2022). *Global Supply Chains of EV Batteries*. Retrieved from https://www.iea.org/reports/global-supply-chains-of-ev-batteries

IEA. (n.d.). Total Mineral Demand From New EV Sales by Scenario, 2020-2040. Retrieved from https://www.iea.org/data-and-statistics/charts/total-mineral-demand-from-new-ev-sales-by-scenario-2020-2040

INN. (2021). *Europe's Graphite Supply Chain – Key Facts*. Retrieved from https://investingnews.com/daily/resource-investing/battery-metals-investing/graphite-investing/europes-graphite-supply-chain/

INN. (2021). *Types of Graphite: Amorphous, Flake and Vein*. Retrieved from https://investingnews.com/daily/resource-investing/battery-metals-investing/graphite-investing/types-of-graphite-amorphous-flake-and-vein/

International Copper Association. (2017). Copper Intensity in the Electrification of Transport and the Integration of Energy Storage. Retrieved from https://copperalliance.org/wp-content/uploads/2017/05/2017.04-E-Mobility-Factsheet-4.pdf

IRENA. (2022). Energy Profile - Madagascar.

IRENA. (2022). Energy Profile - Mozambique.

Jambor, J. L., Dutrizac, J. E., & Raudsepp, M. (2005). Neutralizaiton Potentials of Some Common and Uncommon Rocks, and Some Pitfalls in NP Measurements. Retrieved from https://bc-mlard.ca/files/presentations/2005-3-JAMBOR-ETAL-neutralization-potentials.pdf

Janzen, M. P., Nicholson, R. V., & Scharer, J. M. (2000). Pyrrhotite Reaction Kinetics: Reaction Rates for Oxidation by Oxygen, Ferric Iron, and for Nonoxidative Dissolution. *Geochimica Et Cosmochimica Acta, 64(9), 1511–1522*. doi:https://doi.org/10.1016/s0016-7037(99)00421-4

Jara , A. D., Betermariam, A., Woldetinsae, G., & Kim, J. Y. (2019). Purification, Application and Current Market Trend of Natural Graphite: A review. *International Journal of Mining Science and Technology, 29(5),* 671-689. doi:https://doi.org/10.1016/j.ijmst.2019.04.003

Jeong, S., & Kim, K. (2018). Pre-Concentration of Iron-Rich Sphalerite by Magnetic Separation. *Minerals, 8(7), 272*. doi:https://doi.org/10.3390/min8070272

Jeswiet, J., & Szekeres, A. (2016). Energy Consumption in Mining Comminution. *Procedia CIRP, 48, 140–145*. doi:https://doi.org/10.1016/j.procir.2016.03.250

Jiang, J., & Zhang, C. (2015). Fundamentals and Applications of Lithium-ion Batteries in Electric Drive Vehicles.

Jirestig, J., & Forssberg, E. (1992). Magnetic Characterization of Sulphide Ores: Examples From Sweden. *Magnetic and Electrical Separation, 4(1), 31–45*. doi:https://doi.org/10.1155/1992/37528

Jorjani, E., & Ghahreman, A. (2017). Challenges with Elemental Sulfur Removal During the Leaching of Copper and Zinc Sulfides, and From the Residues; a Review. *Hydrometallurgy, 171, 333–343*. doi:https://doi.org/10.1016/j.hydromet.2017.06.011

Karlsson , T. (2019). *Net Acid Generation (NAG)*. Retrieved from https://mineclosure.gtk.fi/net-acid-generation-nag/

Karlsson, T. (2019). *SEM-MLA*. Retrieved from https://mineclosure.gtk.fi/sem-mla/

Karlsson, T., Alakangas, L., & Kauppila, P. (2021). A Test of Two Methods for Waste Rock Drainage Quality Prediction: Aqua Regia Extraction and Single-addition Net-acid Generation Test Leachate Analysis. *Mine Water and the Environment 40, p. 736–751*. doi:https://doi.org/10.1007/s10230-021-00784-0

Kauppila, M., & Räisänen, M. L. (2019). *Water Cover*. Retrieved from https://mineclosure.gtk.fi/water-cover/

Kauppila, P. (2019). *NP calculated based on carbonate content ("carbonate NP")*. Retrieved from https://mineclosure.gtk.fi/np-calculated-based-on-carbonate-content-carbonate-np/

Kaur, G., & Gates, B. D. (2022). Review—Surface Coatings for Cathodes in Lithium Ion Batteries: From Crystal Structures to Electrochemical Performance. *Journal of the Electrochemical Society, 169(4), 043504*. doi:https://doi.org/10.1149/1945-7111/ac60f3

Kinnunen, P., Karhu, M., Yli-Rantala, E., Kivikytö-Reponen, P., & Mäkinen , J. (2022). A Review of Circular Economy Strategies for Mine Tailings. *Cleaner Engineering and Technology,8, 100499*. doi:https://doi.org/10.1016/j.clet.2022.100499

Kiventerä, J. (2019). *Stabilization of Sulphidic Mine Tailings by Different Treatment Methods*. University of Oulu, Finland. Retrieved from http://jultika.oulu.fi/files/isbn9789526223964.pdf

Kochhar, A., & Timonthy, G. J. (2021). Patent No.: US 11,077,452 B2. US.

Land Nordrhein-Westfalen, C-535/18 (Court of Justice of the European Union 2020). Retrieved from https://curia.europa.eu/juris/liste.jsf?num=C-535/18

Leader, A., & Gausta, G. (2019). Critical Material Applications and Intensities in Clean Energy Technologies. *Clean Technologies, 1(1), 164-184*. doi:https://doi.org/10.3390/cleantechnol1010012

Leading. (n.d.). Retrieved November 29, 2019, from Wikipedia: https://en.wikipedia.org/wiki/Leading

Leco. (2021). *844 Series Combustion Analyzer*. Retrieved from https://www.leco.com/product/844-series

Lennon, J. (2021). The Nickel Market Outlook: The Hype vs. The Reality.

Leskinen, J. (2020). Särkiniemen Vanhan Kaivosalueen Avolouhoksen Veden Laatu ja Vesienkäsittelyn Testaus Teollisuuden Sivutuotteilla. Retrieved from https://www.theseus.fi/bitstream/handle/10024/333145/Leskinen_Jere.pdf.pdf?sequence=2

Li, Y. F., Zhu, S. F., & Wang, L. (2013). Purification of Natural Graphite by Microwave Assisted Acid Leaching. *Carbon, 55, 377–378*. doi:https://doi.org/10.1016/j.carbon.2012.12.059

Lighting Global. (2019). Lithium-ion Batteries Part I: General Overview and 2019 Update. Retrieved from https://www.lightingglobal.org/wp-content/uploads/2019/06/Lithium-Ion_TechNote-2019_update.pdf

Line length. (n.d.). Retrieved November 29, 2019, from Wikipedia: https://en.wikipedia.org/wiki/Line_length

Liu, C., & Wang, Q. (2021). Study on Electrostatic Preparation High-Ash Coal from China Using Roll-Type Electrostatic Separator and the Combustion Characteristics of the Cleaned Coal. *Processes, 9(7), 1139*. doi:https://doi.org/10.3390/pr9071139

Liu, H., Li, B., Xue, J., Hu, J., & Zhang, J. (2020). Mechanical and Electroconductivity Properties of Graphite Mine Tailings Concrete. *Advances in Materials Science and Engineering, 2020, 1–20*. doi:https://doi.org/10.1155/2020/9385097

Liu, Q., Chen, M., Zheng, K., Yang, Y., Feng, X., & Li, H. (2018). In Situ Electrochemical Investigation of Pyrite Assisted Leaching of Chalcopyrite. *Journal of The Electrochemical Society, 165(13)*.

Lottermoser, B. (2010). *Mine Wastes: Characterization, Treatment and Environmental Impacts* (3rd ed.). Springer.

Luodes, H., Kauppila, P., Karlsson, T., Nikkarinen, M., Aatos, S., Tornivaara, A., . . . Kaartinen, T. (2011). Kaivannaisjätteen Luokittelu Pysyväksi - Louhinnassa Muodostuvat Sivukivet. *Suomen Ympäristö 21/2011*.

Maruthupandian, S., Chaliasou, N. A., & Kanellopoulos, A. (2021). Recycling Mine Tailings for a Sustainable Future Built Environment. *Springer Proceedings in Energy, 163–169*. doi:https://doi.org/10.1007/978-3-030-63916-7_21

Matsumoto, S., Ishimatsu, H., Shimada, H., Sasaoka, T., & Kusuma, G. (2018). Characterization of Mine Waste and Acid Mine Drainage Prediction by Simple Testing Methods in Terms of the Effects of Sulfate-Sulfur and Carbonate Minerals. *Minerals, 8(9), 403*. doi:https://doi.org/10.3390/min8090403

MEAE. (2021). Ministry of Economic Affairs and Employment: National Battery Strategy. *Publications of the Ministry of Economic Affairs and Employment, 2021:6*.

Metso. (2011). Basics in Minerals Processing.

Michaux, S. (2019). Graphite Outlook - Opportunities and Challenges.

Michaux, S., Nad, A., Muñoz, E., & Korhonen, T. (2022). BATCircle WP3.1 Graphite Purification.

Mindat. (2022). *Mindat.org - Database of minerals*. Retrieved from https://www.mindat.org/

MML. (2022). Maanmittauslaitos: Karttapaikka. Retrieved from https://asiointi.maanmittauslaitos.fi/karttapaikka/

Moradi, B., & Botte, G. G. (2016). Recycling of Graphite Anodes for the Next Generation of Lithium Ion Batteries. *J Appl Electrochem 46, 123–148*. Retrieved from https://doi.org/10.1007/s10800-015-0914-0

Mordor Intelligence. (2022). *Graphite Market - Growth, Trends, Covid-19 Impact, and Forecast (2022 - 2027)*. Retrieved March 7, 2022, from https://mordorintelligence.com/industry-reports/graphite-market

Multani, R. S., & Waters, K. E. (2018). A Review of the Physicochemical Properties and Flotation of Pyrrhotite Superstructures (4C - Fe7S8/ 5C - Fe9S10) in Ni-Cu Sulphide Mineral Processing. *The Canadian Journal of Chemical Engineering, 96(5), 1185-1206*. doi:https://doi.org/10.1002/cjce.23099

Müller, G. (1979). Schwermetalle in den sediments des Rheins-Veranderungen seitt 1971. *Umschan, 79, 778-783*.

Nasrazadani, S., & Hassani, S. (2016). Modern Analytical Techniques in Failure Analysis of Aerospace, Chemical, and Oil and Gas Industries. *Handbook of Materials Failure Analysis with Case Studies from the Oil and Gas Industry, 39–54*. doi:https://doi.org/10.1016/b978-0-08-100117-2.00010-8

Natarajan, K. (2018). Bioleaching of Zinc, Nickel, and Cobalt. *Biotechnology of Metals, 151-177*. doi:https://doi.org/10.1016/b978-0-12-804022-5.00007-4

Niemelä, M. (2022). Väärässä paikassa. *Suomen Kuvalehti*. Retrieved from Suomen Kuvalehti: https://suomenkuvalehti.fi/paajutut/pitaisiko-naista-oppia-jotain-basf-finnpulp-sokli-kho-kaataa-hankkeita-jotka-on-viety-pitkalle-ilman-lainvoimaista-lupaa/

NMG. (2021). Graphite 101. Retrieved from https://nmg.com/wp-content/uploads/2021/06/NMG-Graphite-101.pdf

Northern Graphite. (2021). About Spherical Graphite.

Ojanperä, M. (2022). *Esimerkin voima - tapaus BASF*. Retrieved from Confederation of Finnish Industries: https://ek.fi/ajankohtaista/blogit/esimerkin-voima-tapaus-basf/

Oxford Analytica. (2021). Graphite market imbalance will grow in the 2020s. *Expert Briefings*. doi:https://doi.org/10.1108/OXAN-DB266286

Payant, R. (2010). The Self-Heating of Sulphide Mixtures.

Petrovskaya, N. (2016). Classification of Minerals on the Magnetic Properties.

Price, W. (2010). *Acid Base Accounting Criteria Used in the Prediciton of Drainage Chemistry*. Retrieved from https://www.imwa.info/docs/imwa_2010/IMWA2010_02_01_price_s.pdf

PRO Heinävesi. (2018). Heinäveden Grafiittikaivoksen Vaikutukista. Retrieved from https://www.sll.fi/app/uploads/sites/40/2018/12/Infopaketti.pdf

Puharinen, S.-T., & Belinskij, A. (2020). EU-tuomioistuimen tuomio kiristää pohjavesien suojelua. Retrieved from https://blogs.uef.fi/oikeuttakohtuudella/2020/07/09/eu-tuomioistuimen-tuomio-kiristaa-pohjavesien-suojelua/

Punkkinen , H., Karlsson, T., Juvankoski, M., Kaartinen, T., Laine-Ylijoki, J., Merta, E., . . . Wahlström, M. (2019). *Acid Generation Potential.* Retrieved from https://mineclosure.gtk.fi/acid-generation-potential/

Punkkinen, H., Juvankoski, M., Kaartinen, T., Laine-Ylijoki, J., Merta , E., Mroueh, U.-M., . . . Wahlström, M. (2019). *Acid-Base Accounting (ABA).* Retrieved from https://mineclosure.gtk.fi/acid-base-accounting-aba/

Punkkinen, H., Karlsson, T., Juvankoski, M., Kaartinen, T., Laine-Ylijoki, J., Merta, E., . . . Wahlström , M. (2019). *Sulphur Determinations.* Retrieved from https://mineclosure.gtk.fi/sulphur-determinations/

Puronaho, L. (2018). *Structural Interpretation of Graphite Bearing Black Schist in Aitolampi, Eastern Finland.* Åbo Akademi University.

Renascor Resources. (2021). *Siviour Graphite Project.* Retrieved from https://renascor.com.au/graphite-projects/

Ritoe, A., Patrahau, I., & Rademaker, M. (2022). Graphite: Supply Chain Challenges & Recommendations for a Critical Mineral.

Robinson Jr., G. R., Hammarstrom, J. M., & Olson, W. D. (2017). Graphite, chap J. In K. J. Schulz, J. H. DeYoung Jr, R. R. Seal II, & D. C. Bradley, *Critical mineral resources of the United States—Economic and environmental geology and prospects for future supply.* U.S. Geological Survey Professional Paper 1802, p. J1–J24. doi:https://doi.org/10.3133/pp1802J

Rudisuela, K. (2020). Competitive Technologies to High Nickel Li-ion Batteries – The Pros and Cons. *Nickel Institute.* Retrieved from https://nickelinstitute.org/en/blog/2020/february/competitive-technologies-to-high-nickel-lithium-ion-batteries-the-pros-and-cons/

Runkel, M., & Sturm, P. (2009). Pyrite Roasting, an Alternative to Suplhur Burning. *Journal of the Southern African Institute of Mining and Metallurgy.*

Sajn, R., Ristovic, I., & Ceplak, B. (2022). Mining and Metallurgical Waste as Potential Secondary Sources. *Minerals 2022, 12, 547.* doi:https://doi.org/10.3390/min12050547

Samsung SDI. (2022). *The Four Components of a Li-ion Battery.* Retrieved from https://www.samsungsdi.com/column/technology/detail/55272.html

Shaw, S. (2005). Case Studies and Subsequent Guidelines for the Use of the Static NAG Procedure. Retrieved from https://bc-mlard.ca/files/presentations/2005-4-SHAW-case-studies-guidelines-static-nag.pdf

Soininen, N., & Belinskij, A. (2020). EU Water Framework Directive from a Finnish Perspective: Evolution from a Paper Tiger to a Beast with Transformative Potential. Retrieved from https://blogs.helsinki.fi/voices-for-sustainability/eu-water-framework-directive-from-a-finnish-perspective-evolution-from-a-paper-tiger-to-a-beast-with-transformative-potential/

Sokli , KHO:2022:38 (The Supreme Administrative Court of Finland 2022).

Su, Y. S., Hsiao, K. C., Sireesha, p., & Huang, J. Y. (2022). Lithium Silicates in Anode Materials for Li-Ion and Li Metal Batteries. *Batteries, 8(1), 2*. doi:https://doi.org/10.3390/batteries8010002

Suomen Nikkeli Oy, ISY-2004-Y-210 (Itä-Suomen Ympäristölupavirasto 2005).

Tamashausky, A. V. (2006). *An Introduction to Synthetic Graphite*. Retrieved from https://asbury.com/media/1225/syntheticgraphiteparti.pdf

Tayebi-Khorami, M., Edraki, M., Corder, G., & Golev, A. (2019). Re-Thinking Mining Waste through an Integrative Approach Led by Circular Economy Aspirations. Retrieved from https://doi.org/10.3390/min9050286

Taylor, H. A. (2006). Graphite. In J. E. Kogel, N. C. Tirvedi, J. M. Barker, & W. T. Krukowski, *Industrial Minerals and Rocks* (pp. 507-518). Colorado: Society for Mining, Metallurgy, and Exploration.

ThermoFisher. (2020). *What is XRF (X-ray Fluorescence) and How Does it Work?* Retrieved from https://www.thermofisher.com/blog/ask-a-scientist/what-is-xrf-x-ray-fluorescence-and-how-does-it-work/

Tornivaara, A., Turunen, K., Lahtinen, T., Heino, N., Pasanen, A., Reinikainen, J., . . . Viitasalo, M. (2020). *Suljettujen ja Hylättyjen Kaivannaisjätealueiden Kunnostustarpeen Arviointi*. Ympäristöministeriö.

Turunen, K., & Pasanen, A. (2019). *Water Management*. Retrieved from https://mineclosure.gtk.fi/water-management/.

Törmänen, T., & Tuomela, P. (2021). Analysis of Finnish Battery Mineral Deposits. *GTK*.

Ulukkulama, G. V., Jaliya, R. C., & Rohitha, L. P. (2018). Increasing the Purity of Graphite Samples Taken from the Under Flow of the Froth Flotaiton Process Using a Gravity Separation Method. Retrieved from https://www.researchgate.net/publication/330661355

UN. (2021). *A Beginner's Guide to Climate Neutrality*. Retrieved from https://unfccc.int/blog/a-beginner-s-guide-to-climate-neutrality

USGS. (2022). *Mineral Commodity Summaries - Graphite (Natural).* Retrieved from https://pubs.usgs.gov/periodicals/mcs2022/mcs2022-graphite.pdf

van den Brink, S., Kleijn, R., Sprecher, B., & Tukker, A. (2020). Identifying Supply Risks by Mapping the Cobalt Supply Chain. *Resources, Conservation and Recycling, 156, 104743.* doi:https://doi.org/10.1016/j.resconrec.2020.104743

Velázquez-Martínez, O., Valio, J., Santasalo-Aarnio, A., Reuter, M., & Serna-Guerrero, R. (2019). Review of Lithium-Ion Battery Recycling Processes from a Circular Economy Perspective. *Batteries, 5(4), 68.* doi:https://doi.org/10.3390/batteries5040068

Vesa, J. (2021). *Kaivosten Sivukivien ja Rikastushiekan Hyödyntämismahdollisuudet : Esiselvitys.* Työ- ja elinkeinoministeriö.

Visual elements. (n.d.). Retrieved November 29, 2019, from Aalto University brand library: https://www.aalto.fi/en/visual-library#/visual-elements/typography

Volt Carbon Technologies. (2022). *Air Classifier Separation of Graphite from Ore.* Retrieved from https://voltcarbontech.com/air-classifier/

Wang, C., Harbottle, D., Liu, Q., & Xu, Z. (2014). Current State of Fine Mineral Tailings Treatment: A Critical Review on Theory and Practice. *Minerals Engineering, 58, 113–131.* doi:https://doi.org/10.1016/j.mineng.2014.01.018

Weber, P. A., Hughes, J. B., Conner, L. B., Lindsay, P., & St. C. Smart, R. (2006). Short Term Acid Rock Drainage Characteristics Determined by Paste pH and Kinetic NAG Testing: Cypress Prospect, New Zealand. *Journal American Society of Mining and Reclamation, 2006(2), 2289-2310.* doi:https://doi.org/10.21000/jasmr06022289

World Bank. (2020). *World Integrated Trade Solutions: Graphite; Artificial Exports by Country in 2020.* Retrieved from https://wits.worldbank.org/trade/comtrade/en/country/ALL/year/2020/tradeflow/Exports/partner/WLD/product/380110

World Bank. (2021). Good Practice Note on Dam Safety – Technical Note 7: Tailings Storage Facilities.

Xiao, W., Li, Y., Zhao, Z., & Liu, X. (2021). Leaching Kinetics of Low Nickel Matte in an Aqueous Solution of Sulfuric Acid Saturated with $FeSO_4$ and $NiSO_4$. *Separation and Purification Technology, 276.* doi:https://doi.org/10.1016/j.seppur.2021.119375

X-Ray Minerals Services Ltd. (2021). *X-ray Diffraction.* Retrieved from https://www.xrayminerals.co.uk/fi/analytical-services/mineralogical-analysis/x-ray-diffraction/

Xu, C., Dai, Q., Gaines, L., Hu, M., Tukker, A., & Steubing, B. (2020). Future Material Demand for Automotive Lithium-based Batteries.

Communications Materials (1), 99. doi:https://doi.org/10.1038/s43246-020-00095-x

Yoshio, M., Wang, H., & Fukuda, K. (2003). Spherical Carbon-Coated Natural Graphite as a Lithium-Ion Battery-Anode Material. *Angewandte Chemie International Edition, 42(35), 4203–4206*. doi:https://doi.org/10.1002/anie.200351203

Yugo, M., & Soler, A. (2019). Outlook for Battery Raw Materials. *Concawe Review, 28(1)*. Retrieved from https://www.concawe.eu/wp-content/uploads/Battery-raw-materials-article.pdf

Zhang, H., Yang, Y., Ren, D., Wang, L., & He, X. (2021). Graphite as Anode Materials: Fundamental Mechanism, Recent Progress and Advances. *Energy Storage Materials, Volume 36, p. 147-170*. Retrieved from https://doi.org/10.1016/j.ensm.2020.12.027

Zhao, L., Ding, B., Qin, X.-Y., Wang, Z., Lv, W., He, Y.-B., . . . Kang, F. (2022). Revisiting the Roles of Natural Graphite in Ongoing Lithium-ion Batteries. *Adv. Mater*. doi:https://doi.org/10.1002/adma.202106704

APPENDIX 1: XRD Diffractograms

ART_E:

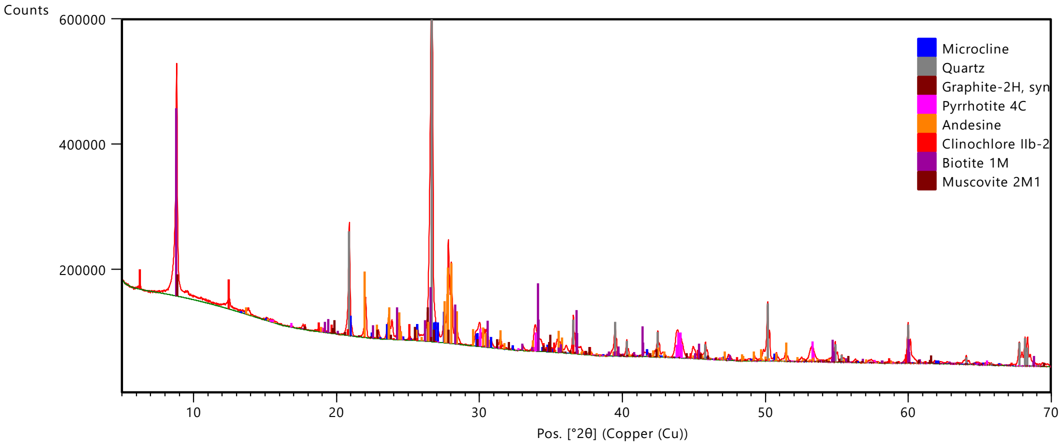

ART_W:

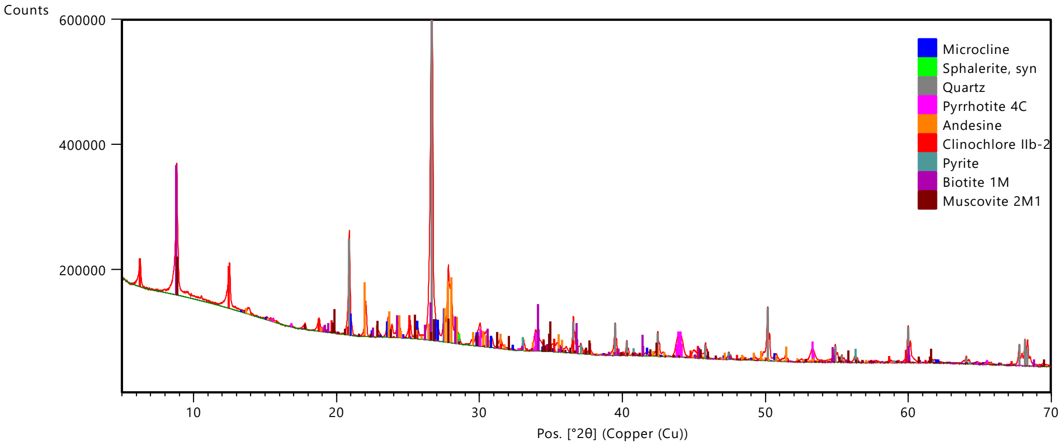

APPENDIX 2: Complete SEM-MLA data (1/2)

ART_E:

ART_E						
Class	**Average density gcm-3**	**Features**	**% Total features**	**Feature area (sq. µm)**	**% Total area**	**% Total mass**
100_Quartz	2.62	4130.00	31.35	1160000.00	34.11	31.37
102_Plagioclase (other than albite)	2.65	3613.00	27.42	954000.00	28.05	26.10
106_Biotite	3.20	1506.00	11.43	368630.00	10.84	12.18
501_Pyrrhotite	4.70	708.00	5.37	212000.00	6.23	10.29
103_K-feldspar	2.54	987.00	7.49	261000.00	7.68	6.84
101_Albite	2.62	762.00	5.78	168000.00	4.94	4.54
107_Muscovite	2.82	378.00	2.87	84200.00	2.48	2.45
104_Feldspar, mixed	2.60	310.00	2.35	51200.00	1.51	1.37
118_Chlorite (clinochlore)	2.65	259.00	1.97	36600.00	1.08	1.00
500_Pyrite	5.01	60.00	0.46	14700.00	0.43	0.76
117_Tremolite	3.05	28.00	0.21	17800.00	0.52	0.56
200_Apatite	3.20	42.00	0.32	12500.00	0.37	0.41
119_Chlorite (chamosite)	2.80	82.00	0.62	12410.00	0.36	0.36
304_Rutile (Ti-oxide)	4.25	27.00	0.20	7450.00	0.22	0.33
504_Sphalerite	4.05	24.00	0.18	6130.00	0.18	0.26
202_Dolomite	2.84	18.00	0.14	6990.00	0.21	0.20
301_Fe-oxide (göthite)	3.80	44.00	0.33	4955.00	0.15	0.19
526_Oxidized Fe-sulphide/Fe-sulphate	4.30	57.00	0.43	2635.00	0.08	0.12
208_Titanite	3.48	13.00	0.10	2610.00	0.08	0.09
217_Cordierite	2.65	14.00	0.11	3090.00	0.09	0.08
224_Kaolinite	2.60	20.00	0.15	2870.00	0.08	0.08
201_Calcite	2.71	11.00	0.08	2670.00	0.08	0.07
218_Almandine	4.10	27.00	0.20	1650.00	0.05	0.07
400_Zircon	4.65	7.00	0.05	1160.00	0.03	0.06
116_Hornblende	3.23	6.00	0.05	1649.00	0.05	0.05
300_Fe-oxide (magnetite/hematite)	5.20	7.00	0.05	597.00	0.02	0.03
225_Glaucophane	3.07	7.00	0.05	949.00	0.03	0.03
209_Tourmaline	3.15	5.00	0.04	472.50	0.01	0.02
220_Grossular	3.57	4.00	0.03	401.00	0.01	0.01
306_Chromite	4.79	4.00	0.03	259.10	0.01	0.01
401_Monazite	5.15	1.00	0.01	231.00	0.01	0.01
207_Epidote	3.45	5.00	0.04	265.00	0.01	0.01
313_Siderite	3.96	3.00	0.02	217.00	0.01	0.01
503_Chalcopyrite	4.19	3.00	0.02	182.00	0.01	0.01
204_Barite	4.48	2.00	0.02	85.60	0.00	0.00
109_Diopside	3.40	1.00	0.01	59.30	0.00	0.00
Total		13175.00	100.00	3400617.50	100.00	100.00

APPENDIX 2: Complete SEM-MLA data (2/2)

ART_W:

ART_W						
Class	**Average density gcm-3**	**Features**	**% Total features**	**Feature area (sq. µm)**	**% Total area**	**% Total mass**
100_Quartz	2.62	3381.00	26.93	1240000.00	33.41	30.23
102_Plagioclase (other than albite)	2.65	1969.00	15.68	612000.00	16.49	15.09
501_Pyrrhotite	4.70	754.00	6.01	294000.00	7.92	12.86
101_Albite	2.62	1271.00	10.12	363000.00	9.78	8.85
103_K-feldspar	2.54	1176.00	9.37	336000.00	9.05	7.94
106_Biotite	3.20	890.00	7.09	229870.00	6.19	6.84
118_Chlorite (clinochlore)	2.65	892.00	7.10	156000.00	4.20	3.85
107_Muscovite	2.82	632.00	5.03	136000.00	3.66	3.57
104_Feldspar, mixed	2.60	441.00	3.51	84600.00	2.28	2.05
500_Pyrite	5.01	158.00	1.26	38500.00	1.04	1.79
117_Tremolite	3.05	128.00	1.02	47700.00	1.29	1.35
119_Chlorite (chamosite)	2.80	201.00	1.60	34120.00	0.92	0.89
304_Rutile (Ti-oxide)	4.25	32.00	0.25	16046.30	0.43	0.63
201_Calcite	2.71	95.00	0.76	23300.00	0.63	0.59
504_Sphalerite	4.05	57.00	0.45	15400.00	0.41	0.58
218_Almandine	4.10	89.00	0.71	8410.00	0.23	0.32
526_Oxidized Fe-sulphide/Fe-sulphate	4.30	66.00	0.53	7303.00	0.20	0.29
300_Fe-oxide (magnetite/hematite)	5.20	9.00	0.07	5924.00	0.16	0.29
200_Apatite	3.20	47.00	0.37	9190.00	0.25	0.27
208_Titanite	3.48	67.00	0.53	7930.00	0.21	0.26
206_Epidote	3.45	14.00	0.11	6425.60	0.17	0.21
401_Monazite	5.15	5.00	0.04	4280.00	0.12	0.21
116_Hornblende	3.23	26.00	0.21	6416.00	0.17	0.19
217_Cordierite	2.65	22.00	0.18	6730.00	0.18	0.17
202_Dolomite	2.84	16.00	0.13	6140.00	0.17	0.16
301_Fe-oxide (göthite)	3.80	26.00	0.21	2430.00	0.07	0.09
111_Ferrosilite	3.95	1.00	0.01	2200.00	0.06	0.08
224_Kaolinite	2.60	24.00	0.19	3340.00	0.09	0.08
109_Diopside	3.40	10.00	0.08	2051.20	0.06	0.06
225_Glaucophane	3.07	8.00	0.06	1320.00	0.04	0.04
503_Chalcopyrite	4.19	12.00	0.10	959.00	0.03	0.04
313_Siderite	3.96	6.00	0.05	959.00	0.03	0.04
220_Grossular	3.57	14.00	0.11	825.00	0.02	0.03
511_Molybdenite	5.50	2.00	0.02	455.00	0.01	0.02
400_Zircon	4.65	2.00	0.02	469.00	0.01	0.02
214_Serpentine	2.53	4.00	0.03	677.00	0.02	0.02
211_Al-silicate	3.61	3.00	0.02	400.00	0.01	0.01
306_Chromite	4.79	3.00	0.02	100.50	0.00	0.00
600_As-Fe sulphate	2.50	1.00	0.01	114.00	0.00	0.00
517_Covellite	4.68	1.00	0.01	29.40	0.00	0.00
209_Tourmaline	3.15	1.00	0.01	27.50	0.00	0.00
Total		12556.00	100.00	3711641.50	100.00	100.00

APPENDIX 3: Complete AMD results (1/2)

ART_E:

Rikki (S)	GQ	Sis. men., Spektrofotometri (IR)	%	4,10
Kokonaishiili (TC)	GQ	Sis. men., Spektrofotometri (IR)	%	0,29
C carb	GQ	Sis. men., Spektrofotometri (IR)	%	0,06
C non-carb	GQ	Sis. men., Spektrofotometri (IR)	%	0,23
AP	GQ	Sis. men., Tekniikka [Laskennallinen]	Kg CaCO3/tonni	130
NP	GQ	Sis. men., Tekniikka [Laskennallinen]	Kg CaCO3/TON	2,6
NNP	GQ	Sis. men., Tekniikka [Laskennallinen]	Kg CaCO3/tonni	<0,3
NPR	GQ	Sis. men., Tekniikka [Laskennallinen]		<0,1
ANC	GQ	Sis. men., Tekniikka [Laskennallinen]	Kg H2SO4/tonni	2,5
MPA	GQ	Sis. men., Tekniikka [Laskennallinen]	Kg H2SO4/tonni	130
NAPP	GQ	Sis. men., Tekniikka [Laskennallinen]	Kg H2SO4/tonni	120
NAG pH 4.5	GQ	ARD Test Handbook, Project P387A, 2002	kg SO4/TON	45
NAG pH 7.0	GQ	ARD Test Handbook, Project P387A, 2002	kg SO4/TON	67
NAG-pH	GQ	ARD Test Handbook, Project P387A, 2002		2,3
Sähkönjohtavuus 25°C	GQ	ARD Test Handbook, Project P387A, 2002	mS/m	305

APPENDIX 3: Complete AMD results (2/2)

ART_W:

Rikki (S)	GQ	Sis. men., Spektrofotometri (IR)	%	4,19
Kokonaishiili (TC)	GQ	Sis. men., Spektrofotometri (IR)	%	0,52
C carb	GQ	Sis. men., Spektrofotometri (IR)	%	0,14
C non-carb	GQ	Sis. men., Spektrofotometri (IR)	%	0,38
AP	GQ	Sis. men., Tekniikka [Laskennallinen]	Kg CaCO3/tonni	130
NP	GQ	Sis. men., Tekniikka [Laskennallinen]	Kg CaCO3/TON	9,9
NNP	GQ	Sis. men., Tekniikka [Laskennallinen]	Kg CaCO3/tonni	<0,3
NPR	GQ	Sis. men., Tekniikka [Laskennallinen]		<0,1
ANC	GQ	Sis. men., Tekniikka [Laskennallinen]	Kg H2SO4/tonni	9,7
MPA	GQ	Sis. men., Tekniikka [Laskennallinen]	Kg H2SO4/tonni	130
NAPP	GQ	Sis. men., Tekniikka [Laskennallinen]	Kg H2SO4/tonni	120
NAG pH 4.5	GQ	ARD Test Handbook, Project P387A, 2002	kg SO4/TON	37
NAG pH 7.0	GQ	ARD Test Handbook, Project P387A, 2002	kg SO4/TON	64
NAG-pH	GQ	ARD Test Handbook, Project P387A, 2002		2,4
Sähkönjohtavuus 25°C	GQ	ARD Test Handbook, Project P387A, 2002	mS/m	278

APPENDIX 4: Magnetic separation results (1/2)

ART_E:

ART_E		M1	NM1	M2	NM2	M3	NM3	Total		
	Mass Flow (g)	131.50	1416.40	68.60	1347.80	426.20	921.60	1547.90		
	Mass flow per element (g)	LIMS	MIMS	HIMS		Recovery				
		M1 (g)	M2 (g)	M3 (g)	NM3 (g)	M1	M2	M3	NM3	Total
Cu	0.19	0.04	0.03	0.05	0.06	22.07 %	15.92 %	28.40 %	33.62 %	100.00 %
Ni	0.38	0.20	0.07	0.06	0.04	53.39 %	19.14 %	15.86 %	11.62 %	100.00 %
Co	0.19	0.02	0.02	0.03	0.12	9.91 %	9.43 %	14.95 %	65.71 %	100.00 %
Zn	1.27	0.04	0.05	0.96	0.22	2.88 %	3.95 %	75.64 %	17.54 %	100.00 %
Pb	0.09	0.00	0.00	0.02	0.06	0.00 %	4.15 %	23.51 %	72.34 %	100.00 %
Ag	0.01	0.00	0.00	0.00	0.00	30.90 %	12.50 %	56.60 %	0.00 %	100.00 %
S	59.60	34.11	12.23	9.42	3.83	57.24 %	20.53 %	15.81 %	6.43 %	100.00 %
As	0.00	0.00	0.00	0.00	0.00	0.00 %	100.00 %	0.00 %	0.00 %	100.00 %
Sb	0.14	0.01	0.01	0.04	0.08	5.64 %	6.51 %	29.49 %	58.36 %	100.00 %
Bi	0.04	0.00	0.00	0.01	0.02	9.46 %	5.10 %	34.65 %	50.79 %	100.00 %
Te	0.01	0.00	0.00	0.00	0.01	0.00 %	0.00 %	31.27 %	68.73 %	100.00 %
Y	0.04	0.00	0.00	0.03	0.02	0.50 %	5.47 %	57.76 %	36.28 %	100.00 %
Nb	0.02	0.00	0.00	0.01	0.02	0.00 %	0.00 %	28.93 %	71.07 %	100.00 %
Mo	0.01	0.00	0.00	0.00	0.01	0.00 %	3.34 %	30.22 %	66.44 %	100.00 %
Sn	0.03	0.00	0.00	0.01	0.02	0.00 %	5.63 %	38.27 %	56.09 %	100.00 %
W	0.01	0.00	0.00	0.00	0.01	7.39 %	5.98 %	27.08 %	59.54 %	100.00 %
Cl	0.10	0.00	0.00	0.06	0.04	4.37 %	4.42 %	56.02 %	35.19 %	100.00 %
Th	0.02	0.00	0.00	0.01	0.01	8.59 %	7.31 %	51.33 %	32.76 %	100.00 %
U	0.01	0.01	0.00	0.00	0.00	94.21 %	5.79 %	0.00 %	0.00 %	100.00 %
Cs	0.04	0.00	0.00	0.01	0.02	9.00 %	9.71 %	32.97 %	48.32 %	100.00 %
La	0.14	0.00	0.00	0.08	0.04	3.24 %	1.96 %	62.23 %	32.57 %	100.00 %
Ce	0.14	0.00	0.01	0.10	0.04	1.58 %	3.82 %	69.24 %	25.37 %	100.00 %
Ta	0.03	0.00	0.00	0.00	0.02	16.83 %	0.00 %	15.41 %	67.76 %	100.00 %
LOI	0.00	0.00	0.00	0.00	0.00	-	-	-	-	-
Ga	0.03	0.00	0.00	0.01	0.01	6.49 %	6.80 %	40.57 %	46.14 %	100.00 %
Si	445.69	4.79	18.22	107.97	314.71	1.08 %	4.09 %	24.23 %	70.61 %	100.00 %
Ti	4.97	0.05	0.17	2.67	2.08	0.98 %	3.47 %	53.70 %	41.85 %	100.00 %
Cr	0.24	0.03	0.01	0.13	0.07	12.32 %	5.17 %	53.49 %	29.03 %	100.00 %
V	0.66	0.01	0.02	0.43	0.20	1.40 %	3.51 %	65.48 %	29.60 %	100.00 %
Fe	102.03	54.10	18.75	21.27	7.91	53.02 %	18.38 %	20.85 %	7.75 %	100.00 %
Mn	0.50	0.01	0.01	0.38	0.11	1.10 %	2.84 %	74.83 %	21.23 %	100.00 %
Mg	27.72	0.40	0.94	19.90	6.49	1.43 %	3.38 %	71.77 %	23.41 %	100.00 %
Ca	25.68	0.37	1.31	6.31	17.69	1.45 %	5.11 %	24.56 %	68.88 %	100.00 %
Ba	0.82	0.01	0.03	0.24	0.53	1.21 %	3.93 %	29.66 %	65.20 %	100.00 %
Leco C	2.17	0.17	0.50	1.20	0.30	7.84 %	23.05 %	55.18 %	13.93 %	100.00 %
Leco S	66.30	38.14	16.23	9.14	2.79	57.53 %	24.48 %	13.78 %	4.21 %	100.00 %

APPENDIX 4: Magnetic separation results (2/2)

ART_W:

ART_W		M1	NM1	M2	Total	M3	NM3	Total		
	Mass Flow (g)	131.50	1416.40	68.60	1347.80	426.20	921.60	1547.90		
	Mass flow per element (g)	LIMS	MIMS	HIMS		Recovery				
		M1 (g)	M2 (g)	M3 (g)	NM3 (g)	M1	M2	M3	NM3	Total
Cu	0.50	0.05	0.05	0.21	0.19	10.19 %	9.00 %	42.35 %	38.46 %	100.00 %
Ni	0.53	0.32	0.05	0.08	0.08	59.71 %	10.21 %	14.45 %	15.63 %	100.00 %
Co	0.12	0.02	0.01	0.03	0.06	19.43 %	6.56 %	25.94 %	48.07 %	100.00 %
Zn	2.30	0.05	0.08	1.62	0.55	2.34 %	3.40 %	70.22 %	24.04 %	100.00 %
Pb	0.10	0.00	0.00	0.03	0.06	0.00 %	2.83 %	30.73 %	66.45 %	100.00 %
Ag	0.02	0.00	0.00	0.01	0.01	12.49 %	3.26 %	40.48 %	43.77 %	100.00 %
S	63.22	38.66	6.65	8.69	9.22	61.15 %	10.51 %	13.75 %	14.58 %	100.00 %
As	0.00	0.00	0.00	0.00	0.00	100.00 %	0.00 %	0.00 %	0.00 %	100.00 %
Sb	0.16	0.01	0.01	0.05	0.09	6.73 %	4.39 %	29.97 %	58.92 %	100.00 %
Bi	0.05	0.00	0.00	0.01	0.03	8.62 %	3.00 %	27.95 %	60.43 %	100.00 %
Te	0.01	0.00	0.00	0.00	0.01	0.00 %	0.00 %	0.00 %	100.00 %	100.00 %
Y	0.06	0.00	0.00	0.03	0.02	2.75 %	3.23 %	50.58 %	43.43 %	100.00 %
Nb	0.02	0.00	0.00	0.01	0.01	0.00 %	0.35 %	30.05 %	69.61 %	100.00 %
Mo	0.08	0.00	0.00	0.02	0.06	0.00 %	4.13 %	24.13 %	71.74 %	100.00 %
Sn	0.03	0.00	0.00	0.01	0.02	0.00 %	4.84 %	30.09 %	65.07 %	100.00 %
W	0.01	0.00	0.00	0.00	0.00	23.58 %	0.00 %	76.42 %	0.00 %	100.00 %
Cl	0.14	0.00	0.00	0.06	0.06	2.88 %	3.50 %	46.60 %	47.02 %	100.00 %
Th	0.03	0.00	0.00	0.01	0.01	1.01 %	2.64 %	57.37 %	38.99 %	100.00 %
U	0.01	0.01	0.00	0.00	0.00	100.00 %	0.00 %	0.00 %	0.00 %	100.00 %
Cs	0.03	0.00	0.00	0.01	0.02	12.49 %	2.17 %	26.99 %	58.35 %	100.00 %
La	0.21	0.01	0.00	0.14	0.06	4.41 %	1.64 %	67.43 %	26.51 %	100.00 %
Ce	0.26	0.01	0.00	0.17	0.07	2.03 %	1.86 %	67.59 %	28.52 %	100.00 %
Ta	0.02	0.00	0.00	0.00	0.02	5.48 %	0.00 %	17.75 %	76.77 %	100.00 %
LOI	0.00	0.00	0.00	0.00	0.00	-	-	-	-	-
Ga	0.03	0.00	0.00	0.01	0.01	8.59 %	5.01 %	47.47 %	38.94 %	100.00 %
Si	448.35	6.71	15.71	111.66	314.27	1.50 %	3.50 %	24.91 %	70.09 %	100.00 %
Ti	5.19	0.07	0.15	2.47	2.49	1.39 %	2.98 %	47.66 %	47.97 %	100.00 %
Cr	0.30	0.04	0.01	0.14	0.10	12.38 %	4.84 %	48.71 %	34.07 %	100.00 %
V	1.12	0.02	0.04	0.61	0.45	2.11 %	3.85 %	53.86 %	40.19 %	100.00 %
Fe	110.62	62.59	10.43	22.76	14.84	56.59 %	9.43 %	20.57 %	13.41 %	100.00 %
Mn	0.53	0.01	0.02	0.36	0.15	1.73 %	3.22 %	67.32 %	27.73 %	100.00 %
Mg	34.02	0.63	1.13	21.01	11.24	1.86 %	3.33 %	61.77 %	33.05 %	100.00 %
Ca	28.80	0.55	1.19	8.99	18.06	1.92 %	4.14 %	31.22 %	62.72 %	100.00 %
Ba	0.83	0.02	0.03	0.22	0.56	2.05 %	4.03 %	26.56 %	67.37 %	100.00 %
Leco C	5.74	0.47	0.72	2.13	2.41	8.21 %	12.56 %	37.15 %	42.09 %	100.00 %
Leco S	66.44	42.55	6.91	9.15	7.82	64.05 %	10.40 %	13.77 %	11.78 %	100.00 %

APPENDIX 5: Gravity separation results (1/2)

ART_E:

ART_E		Concentrate	Middlings	Tailings	Total			
	Mass Flow (g)	244.10	2190.00	568.00	3002.10			
	Mass flow per element (g)	GHS	GSM	GSL	Recovery	GHS	GSM	GSL
		Concentrate	Middlings	Tailings	Concentrate	Middlings	Tailings	Total
Cu	0.34	0.07	0.20	0.07	21.07 %	58.65 %	20.28 %	100.00 %
Ni	0.78	0.33	0.35	0.10	41.95 %	44.94 %	13.11 %	100.00 %
Co	0.49	0.07	0.35	0.07	13.88 %	71.13 %	14.99 %	100.00 %
Zn	2.36	0.55	1.27	0.53	23.42 %	53.92 %	22.66 %	100.00 %
Pb	0.17	0.00	0.13	0.03	1.45 %	78.25 %	20.30 %	100.00 %
Ag	0.03	0.01	0.02	0.01	20.98 %	62.75 %	16.27 %	100.00 %
S	127.45	59.80	54.75	12.89	46.92 %	42.96 %	10.12 %	100.00 %
As	0.00	0.00	0.00	0.00	100.00 %	0.00 %	0.00 %	100.00 %
Sb	0.30	0.02	0.22	0.06	6.61 %	74.15 %	19.23 %	100.00 %
Bi	0.08	0.01	0.04	0.02	19.40 %	58.02 %	22.57 %	100.00 %
Te	0.01	0.00	0.00	0.01	0.00 %	0.00 %	100.00 %	100.00 %
Y	0.07	0.01	0.04	0.02	19.77 %	50.67 %	29.57 %	100.00 %
Nb	0.04	0.01	0.03	0.01	16.09 %	66.63 %	17.28 %	100.00 %
Mo	0.03	0.00	0.02	0.01	0.00 %	81.08 %	18.92 %	100.00 %
Sn	0.08	0.00	0.07	0.01	3.07 %	82.64 %	14.29 %	100.00 %
W	0.00	0.00	0.00	0.00	100.00 %	0.00 %	0.00 %	100.00 %
Cl	0.20	0.02	0.13	0.05	8.56 %	65.83 %	25.61 %	100.00 %
Th	0.04	0.01	0.02	0.01	23.04 %	54.39 %	22.57 %	100.00 %
U	0.02	0.02	0.00	0.00	100.00 %	0.00 %	0.00 %	100.00 %
Cs	0.05	0.00	0.04	0.01	0.00 %	88.52 %	11.48 %	100.00 %
La	0.23	0.07	0.11	0.05	31.36 %	48.51 %	20.13 %	100.00 %
Ce	0.30	0.09	0.15	0.06	30.06 %	51.03 %	18.91 %	100.00 %
Ta	0.01	0.01	0.00	0.00	100.00 %	0.00 %	0.00 %	100.00 %
LOI	0.00	0.00	0.00	0.00	-	-	-	-
Ga	0.05	0.01	0.03	0.01	13.40 %	62.34 %	24.25 %	100.00 %
Si	892.54	29.05	694.23	169.26	3.25 %	77.78 %	18.96 %	100.00 %
Ti	10.02	2.51	5.67	1.83	25.10 %	56.63 %	18.26 %	100.00 %
Cr	0.51	0.02	0.33	0.16	4.77 %	64.17 %	31.07 %	100.00 %
V	1.34	0.06	0.92	0.36	4.19 %	68.67 %	27.14 %	100.00 %
Fe	207.25	89.34	91.32	26.58	43.11 %	44.07 %	12.83 %	100.00 %
Mn	0.96	0.03	0.66	0.28	3.04 %	68.11 %	28.85 %	100.00 %
Mg	54.99	0.88	39.86	14.26	1.60 %	72.48 %	25.92 %	100.00 %
Ca	52.73	2.25	39.86	10.62	4.26 %	75.60 %	20.15 %	100.00 %
Ba	1.59	0.03	1.18	0.38	1.84 %	74.26 %	23.90 %	100.00 %
Leco C	10.31	0.27	9.42	0.62	2.60 %	91.34 %	6.06 %	100.00 %
Leco S	120.65	65.83	43.80	11.02	54.56 %	36.30 %	9.13 %	100.00 %

APPENDIX 5: Gravity separation results (2/2)

ART_W:

ART_W		Concentrate	Middlings	Tailings	Total			
	Mass Flow (g)	231.60	1933.00	885.40	3050.00			
	Mass flow per element (g)	GHS	GSM	GSL	Recovery	GHS	GSM	GSL
		Concentrate	Middlings	Tailings	Concentrate	Middlings	Tailings	Total
Cu	0.99	0.17	0.46	0.36	16.78 %	46.69 %	36.53 %	100.00 %
Ni	1.08	0.34	0.50	0.23	31.87 %	46.73 %	21.40 %	100.00 %
Co	0.44	0.06	0.29	0.10	12.55 %	65.46 %	21.99 %	100.00 %
Zn	4.90	1.16	2.15	1.59	23.65 %	43.81 %	32.54 %	100.00 %
Pb	0.18	0.01	0.12	0.06	3.76 %	62.72 %	33.52 %	100.00 %
Ag	0.04	0.01	0.02	0.01	19.78 %	55.02 %	25.20 %	100.00 %
S	141.74	53.73	66.50	21.52	37.91 %	46.91 %	15.18 %	100.00 %
As	0.00	0.00	0.00	0.00	100.00 %	0.00 %	0.00 %	100.00 %
Sb	0.31	0.02	0.19	0.10	7.38 %	61.59 %	31.03 %	100.00 %
Bi	0.06	0.01	0.04	0.02	10.97 %	61.06 %	27.97 %	100.00 %
Te	0.00	0.00	0.00	0.00	-	-	-	-
Y	0.11	0.02	0.06	0.03	14.51 %	55.37 %	30.12 %	100.00 %
Nb	0.03	0.01	0.02	0.01	17.58 %	52.84 %	29.58 %	100.00 %
Mo	0.16	0.00	0.08	0.08	0.00 %	49.31 %	50.69 %	100.00 %
Sn	0.08	0.00	0.06	0.02	5.77 %	72.19 %	22.04 %	100.00 %
W	0.00	0.00	0.00	0.00	-	-	-	-
Cl	0.27	0.01	0.17	0.08	4.37 %	65.59 %	30.04 %	100.00 %
Th	0.06	0.01	0.04	0.02	16.44 %	59.27 %	24.29 %	100.00 %
U	0.01	0.01	0.00	0.00	100.00 %	0.00 %	0.00 %	100.00 %
Cs	0.05	0.00	0.04	0.01	0.00 %	81.37 %	18.63 %	100.00 %
La	0.43	0.13	0.17	0.13	28.96 %	40.29 %	30.75 %	100.00 %
Ce	0.55	0.15	0.23	0.17	27.64 %	41.94 %	30.42 %	100.00 %
Ta	0.05	0.00	0.04	0.01	4.65 %	77.58 %	17.77 %	100.00 %
LOI	0.00	0.00	0.00	0.00	-	-	-	-
Ga	0.07	0.00	0.05	0.02	5.57 %	65.62 %	28.81 %	100.00 %
Si	873.13	30.34	589.57	253.22	3.47 %	67.52 %	29.00 %	100.00 %
Ti	10.39	2.34	5.01	3.05	22.51 %	48.18 %	29.31 %	100.00 %
Cr	0.60	0.03	0.31	0.27	4.61 %	51.32 %	44.07 %	100.00 %
V	2.23	0.08	1.22	0.93	3.74 %	54.59 %	41.67 %	100.00 %
Fe	231.24	75.50	108.63	47.10	32.65 %	46.98 %	20.37 %	100.00 %
Mn	1.08	0.04	0.58	0.46	3.65 %	53.71 %	42.64 %	100.00 %
Mg	67.77	1.71	38.08	27.98	2.53 %	56.19 %	41.28 %	100.00 %
Ca	55.30	3.08	34.60	17.62	5.57 %	62.57 %	31.86 %	100.00 %
Ba	1.64	0.05	1.02	0.57	2.97 %	62.48 %	34.56 %	100.00 %
Leco C	12.94	0.79	8.70	3.45	6.09 %	67.23 %	26.69 %	100.00 %
Leco S	134.12	57.09	57.02	20.01	42.56 %	42.52 %	14.92 %	100.00 %

APPENDIX 6: Processing scenario results (1/2)

ART_E:

ART_E		M1	NM1	Total		NM1 as feed to Gravity Separation	GSH	GSM	GSL	Total			
	Mass Flow (g)	110.4	1382.7	1493.1			112.4	1008.7	261.6	1382.7			
	Mass pull	7.4 %	92.6 %	100 %			8.1 %	72.9 %	18.9 %	100 %			
XRF	LIMS	Recovery		Grade		Gravity separation	Recovery			Grade			
	Input grade in %	M1	NM1	M1	NM1	NM1 as feed to Gravity Separation	GSH	GSM	GSL	GSH	GSM	GSL	GSM and GSL
Cu	0.01	22.07 %	77.9 %	0.03 %	0.01 %		21.07 %	58.65 %	20.28 %	0.02 %	0.01 %	0.01 %	0.01 %
Ni	0.03	53.39 %	46.6 %	0.20 %	0.01 %		41.95 %	44.94 %	13.11 %	0.07 %	0.01 %	0.01 %	0.01 %
Co	0.02	9.91 %	90.1 %	0.02 %	0.02 %		13.88 %	71.13 %	14.99 %	0.03 %	0.02 %	0.01 %	0.02 %
Zn	0.1	2.88 %	97.1 %	0.03 %	0.08 %		23.42 %	53.92 %	22.66 %	0.23 %	0.06 %	0.09 %	0.07 %
Pb	0.01	0.00 %	100.0 %	0.00 %	0.01 %		1.45 %	78.25 %	20.30 %	0.00 %	0.01 %	0.01 %	0.01 %
Ag	0.001	30.90 %	69.1 %	0.00 %	0.00 %		20.98 %	62.75 %	16.27 %	0.00 %	0.00 %	0.00 %	0.00 %
S	4.6	57.24 %	42.8 %	35.61 %	2.12 %		46.92 %	42.96 %	10.12 %	12.26 %	1.25 %	1.14 %	1.23 %
As	0.00	0.00 %	100.0 %	0.00 %	0.00 %		100.00 %	0.00 %	0.00 %	0.00 %	0.00 %	0.00 %	0.00 %
Sb	0.01	5.64 %	94.4 %	0.01 %	0.01 %		6.61 %	74.15 %	19.23 %	0.01 %	0.01 %	0.01 %	0.01 %
Bi	0.002	9.46 %	90.5 %	0.00 %	0.00 %		19.40 %	58.02 %	22.57 %	0.00 %	0.00 %	0.00 %	0.00 %
Te	0.000	0.00 %	100.0 %	0.00 %	0.00 %		0.00 %	0.00 %	100.00 %	0.00 %	0.00 %	0.00 %	0.00 %
Y	0.003	0.50 %	99.5 %	0.00 %	0.00 %		19.77 %	50.67 %	29.57 %	0.01 %	0.00 %	0.01 %	0.00 %
Nb	0.001	0.00 %	100.0 %	0.00 %	0.00 %		16.09 %	66.63 %	17.28 %	0.00 %	0.00 %	0.00 %	0.00 %
Mo	0.001	0.00 %	100.0 %	0.00 %	0.00 %		0.00 %	81.08 %	18.92 %	0.00 %	0.00 %	0.00 %	0.00 %
Sn	0.003	0.00 %	100.0 %	0.00 %	0.00 %		3.07 %	82.64 %	14.29 %	0.00 %	0.00 %	0.00 %	0.00 %
W	0.000	7.39 %	92.6 %	0.00 %	0.00 %		100.00 %	0.00 %	0.00 %	0.00 %	0.00 %	0.00 %	0.00 %
Cl	0.01	4.37 %	95.6 %	0.01 %	0.01 %		8.56 %	65.83 %	25.61 %	0.01 %	0.01 %	0.02 %	0.01 %
Th	0.002	8.59 %	91.4 %	0.00 %	0.00 %		23.04 %	54.39 %	22.57 %	0.00 %	0.00 %	0.00 %	0.00 %
U	0.0	94.21 %	5.8 %	0.00 %	0.00 %		100.00 %	0.00 %	0.00 %	0.00 %	0.00 %	0.00 %	0.00 %
Cs	0.001	9.00 %	91.0 %	0.00 %	0.00 %		0.00 %	88.52 %	11.48 %	0.00 %	0.00 %	0.00 %	0.00 %
La	0.01	3.24 %	96.8 %	0.00 %	0.01 %		31.36 %	48.51 %	20.13 %	0.04 %	0.01 %	0.01 %	0.01 %
Ce	0.01	1.58 %	98.4 %	0.00 %	0.01 %		30.06 %	51.03 %	18.91 %	0.05 %	0.01 %	0.01 %	0.01 %
Ta	0.0	16.83 %	83.2 %	0.00 %	0.00 %		100.00 %	0.00 %	0.00 %	0.00 %	0.00 %	0.00 %	0.00 %
LOI													
Ga	0.002	6.49 %	93.5 %	0.00 %	0.00 %		13.40 %	62.34 %	24.25 %	0.00 %	0.00 %	0.00 %	0.00 %
Si	29.5	1.08 %	98.9 %	4.29 %	31.51 %		3.25 %	77.78 %	18.96 %	12.61 %	33.60 %	31.59 %	33.19 %
Ti	0.3	0.98 %	99.0 %	0.04 %	0.35 %		25.10 %	56.63 %	18.26 %	1.07 %	0.27 %	0.33 %	0.28 %
Cr	0.02	12.32 %	87.7 %	0.02 %	0.01 %		4.77 %	64.17 %	31.07 %	0.01 %	0.01 %	0.02 %	0.01 %
V	0.04	1.40 %	98.6 %	0.01 %	0.05 %		4.19 %	68.67 %	27.14 %	0.02 %	0.04 %	0.07 %	0.05 %
Fe	7.1	53.02 %	47.0 %	50.91 %	3.60 %		43.11 %	44.07 %	12.83 %	19.10 %	2.18 %	2.44 %	2.23 %
Mn	0.03	1.10 %	98.9 %	0.00 %	0.03 %		3.04 %	68.11 %	28.85 %	0.01 %	0.03 %	0.05 %	0.04 %
Mg	1.9	1.43 %	98.6 %	0.36 %	1.98 %		1.60 %	72.48 %	25.92 %	0.39 %	1.97 %	2.71 %	2.12 %
Ca	1.8	1.45 %	98.6 %	0.35 %	1.88 %		4.26 %	75.60 %	20.15 %	0.99 %	1.95 %	2.01 %	1.96 %
Ba	0.1	1.21 %	98.8 %	0.01 %	0.06 %		1.84 %	74.26 %	23.90 %	0.01 %	0.06 %	0.08 %	0.06 %
Leco C	0.3	7.84 %	92.2 %	0.36 %	0.34 %		2.60 %	91.34 %	6.06 %	0.11 %	0.42 %	0.11 %	0.36 %
Leco S	4.2	57.53 %	42.5 %	32.60 %	1.92 %		54.56 %	36.30 %	9.13 %	12.90 %	0.96 %	0.93 %	0.95 %
SiO2	63.0	1.07 %	98.9 %	9.15 %	67.30 %		3.26 %	77.76 %	18.98 %	27.02 %	71.74 %	67.50 %	70.86 %
TiO2	0.5	0.99 %	99.0 %	0.07 %	0.58 %		25.10 %	56.56 %	18.34 %	1.78 %	0.45 %	0.56 %	0.47 %
Al2O3	12.7	1.49 %	98.5 %	2.57 %	13.51 %		2.46 %	75.45 %	22.09 %	4.09 %	13.97 %	15.77 %	14.34 %
Cr2O3	0.02	12.15 %	87.9 %	0.03 %	0.02 %		4.87 %	64.13 %	31.00 %	0.01 %	0.02 %	0.03 %	0.02 %
V2O3	0.1	1.36 %	98.6 %	0.01 %	0.07 %		4.26 %	68.61 %	27.13 %	0.04 %	0.06 %	0.10 %	0.07 %
FeO	9.1	53.04 %	47.0 %	65.49 %	4.63 %		43.05 %	44.12 %	12.83 %	24.51 %	2.80 %	3.14 %	2.87 %
MnO	0.04	1.20 %	98.8 %	0.01 %	0.04 %		2.93 %	68.41 %	28.66 %	0.02 %	0.04 %	0.07 %	0.05 %
MgO	3.1	1.44 %	98.6 %	0.60 %	3.28 %		1.58 %	72.51 %	25.91 %	0.64 %	3.26 %	4.49 %	3.51 %
CaO	2.5	1.45 %	98.5 %	0.49 %	2.63 %		4.26 %	75.59 %	20.14 %	1.38 %	2.72 %	2.80 %	2.74 %
Rb2O	0.01	12.05 %	88.0 %	0.01 %	0.01 %		9.78 %	65.83 %	24.39 %	0.01 %	0.01 %	0.01 %	0.01 %
SrO	0.02	0.00 %	100.0 %	0.00 %	0.02 %		0.99 %	77.85 %	21.15 %	0.00 %	0.02 %	0.02 %	0.02 %
BaO	0.1	1.33 %	98.7 %	0.01 %	0.07 %		1.80 %	74.40 %	23.80 %	0.01 %	0.07 %	0.08 %	0.07 %
Na2O	2.5	1.88 %	98.1 %	0.64 %	2.67 %		3.28 %	76.92 %	19.80 %	1.08 %	2.82 %	2.79 %	2.81 %
K2O	2.2	0.91 %	99.1 %	0.27 %	2.31 %		1.33 %	74.70 %	23.98 %	0.38 %	2.37 %	2.93 %	2.48 %
ZrO2	0.0	2.07 %	97.9 %	0.01 %	0.02 %		11.44 %	66.23 %	22.33 %	0.03 %	0.02 %	0.03 %	0.02 %
P2O5	0.2	0.83 %	99.2 %	0.02 %	0.20 %		19.61 %	60.46 %	19.93 %	0.47 %	0.16 %	0.21 %	0.17 %
CO2	1.2	7.71 %	92.3 %	1.29 %	1.24 %		2.58 %	91.42 %	6.00 %	0.39 %	1.55 %	0.39 %	1.31 %
ICP_MS													
Ag	0.001	10.48 %	89.5 %	0.00 %	0.00 %		7.28 %	65.33 %	27.38 %	0.00 %	0.00 %	0.00 %	0.00 %
Al	6.70	1.37 %	98.6 %	1.24 %	7.13 %		2.26 %	75.64 %	22.10 %	1.98 %	7.40 %	8.33 %	7.59 %
As	0.001	7.39 %	92.6 %	0.00 %	0.00 %		18.02 %	65.10 %	16.88 %	0.00 %	0.00 %	0.00 %	0.00 %
Ca	1.72	1.41 %	98.6 %	0.33 %	1.83 %		4.53 %	75.08 %	20.40 %	1.02 %	1.89 %	1.98 %	1.91 %
Cd	0.001	2.63 %	97.4 %	0.00 %	0.00 %		28.71 %	47.02 %	24.27 %	0.00 %	0.00 %	0.00 %	0.00 %
Co	0.004	46.63 %	53.4 %	0.02 %	0.00 %		44.12 %	42.41 %	13.47 %	0.01 %	0.00 %	0.00 %	0.00 %
Cr	0.01	31.85 %	68.1 %	0.05 %	0.01 %		3.42 %	64.34 %	32.24 %	0.00 %	0.01 %	0.02 %	0.01 %
Cu	0.01	20.29 %	79.7 %	0.03 %	0.01 %		20.76 %	62.76 %	16.48 %	0.02 %	0.01 %	0.01 %	0.01 %
Fe	6.97	60.75 %	39.3 %	57.23 %	2.95 %		43.77 %	43.32 %	12.91 %	15.90 %	1.75 %	2.01 %	1.81 %
K	1.98	1.28 %	98.7 %	0.34 %	2.11 %		1.40 %	75.07 %	23.53 %	0.36 %	2.17 %	2.62 %	2.26 %
Li	0.002	5.30 %	94.7 %	0.00 %	0.00 %		1.98 %	72.87 %	25.15 %	0.00 %	0.00 %	0.00 %	0.00 %
Mg	1.62	2.46 %	97.5 %	0.54 %	1.70 %		1.40 %	73.46 %	25.14 %	0.29 %	1.71 %	2.26 %	1.83 %
Mn	0.04	3.45 %	96.5 %	0.02 %	0.05 %		3.64 %	69.79 %	26.58 %	0.02 %	0.04 %	0.06 %	0.05 %
Ni	0.02	60.60 %	39.4 %	0.19 %	0.01 %		48.03 %	39.62 %	12.35 %	0.06 %	0.01 %	0.01 %	0.01 %
P	0.06	0.55 %	99.4 %	0.00 %	0.07 %		19.82 %	60.01 %	20.16 %	0.16 %	0.05 %	0.07 %	0.06 %
Pb	0.003	9.40 %	90.6 %	0.00 %	0.00 %		10.32 %	65.63 %	24.05 %	0.00 %	0.00 %	0.00 %	0.00 %
S	2.84	64.21 %	35.8 %	24.64 %	1.10 %		51.63 %	37.16 %	11.21 %	6.96 %	0.56 %	0.65 %	0.58 %
Ti	0.16	1.88 %	98.1 %	0.04 %	0.17 %		1.95 %	71.85 %	26.20 %	0.04 %	0.17 %	0.24 %	0.19 %
Zn	0.09	3.67 %	96.3 %	0.05 %	0.10 %		25.68 %	50.73 %	23.59 %	0.30 %	0.07 %	0.12 %	0.08 %

APPENDIX 6: Processing scenario results (2/2)

ART_W:

ART_W		M1	NM1	Total		NM1 as feed to	GSH	GSM	GSL	Total			
	Mass Flow (g)	131.5	1416.4	1547.9		Gravity	107.6	897.7	411.2	1416.4			
	Mass pull	8.5 %	91.5 %	100 %		Separation	7.6 %	63.4 %	29.0 %	100 %			
XRF	LIMS	Recovery		Grade		Gravity separatior	Recovery			Grade			
	Input grade in %	M1	NM1	M1	NM1	NM1 as feed to	GSH	GSM	GSL	GSH	GSM	GSL	GSM and GSL
Cu	0.03	10.19 %	89.8 %	0.04 %	0.03 %	Gravity	16.78 %	46.69 %	36.53 %	0.07 %	0.02 %	0.04 %	0.03 %
Ni	0.03	59.71 %	40.3 %	0.24 %	0.01 %	Separation	31.87 %	46.73 %	21.40 %	0.06 %	0.01 %	0.01 %	0.01 %
Co	0.01	19.43 %	80.6 %	0.03 %	0.01 %		12.55 %	65.46 %	21.99 %	0.02 %	0.01 %	0.01 %	0.01 %
Zn	0.2	2.34 %	97.7 %	0.04 %	0.16 %		23.65 %	43.81 %	32.54 %	0.51 %	0.11 %	0.18 %	0.14 %
Pb	0.01	0.00 %	100.0 %	0.00 %	0.01 %		3.76 %	62.72 %	33.52 %	0.00 %	0.01 %	0.01 %	0.01 %
Ag	0.001	12.49 %	87.5 %	0.00 %	0.00 %		19.78 %	55.02 %	25.20 %	0.00 %	0.00 %	0.00 %	0.00 %
S	4.5	61.15 %	38.8 %	32.39 %	1.91 %		37.91 %	46.91 %	15.18 %	9.54 %	1.41 %	1.00 %	1.28 %
As	0.00	100.00 %	0.0 %	0.00 %	0.00 %		100.00 %	0.00 %	0.00 %	0.00 %	0.00 %	0.00 %	0.00 %
Sb	0.01	6.73 %	93.3 %	0.01 %	0.01 %		7.38 %	61.59 %	31.03 %	0.01 %	0.01 %	0.01 %	0.01 %
Bi	0.002	8.62 %	91.4 %	0.00 %	0.00 %		10.97 %	61.06 %	27.97 %	0.00 %	0.00 %	0.00 %	0.00 %
Te	0.000	0.00 %	100.0 %	0.00 %	0.00 %								
Y	0.003	2.75 %	97.2 %	0.00 %	0.00 %		14.51 %	55.37 %	30.12 %	0.01 %	0.00 %	0.00 %	0.00 %
Nb	0.001	0.00 %	100.0 %	0.00 %	0.00 %		17.58 %	52.84 %	29.58 %	0.00 %	0.00 %	0.00 %	0.00 %
Mo	0.006	0.00 %	100.0 %	0.00 %	0.01 %		0.00 %	49.31 %	50.69 %	0.00 %	0.00 %	0.01 %	0.01 %
Sn	0.002	0.00 %	100.0 %	0.00 %	0.00 %		5.77 %	72.19 %	22.04 %	0.00 %	0.00 %	0.00 %	0.00 %
W	0.000	23.58 %	76.4 %	0.00 %	0.00 %								
Cl	0.01	2.88 %	97.1 %	0.00 %	0.01 %		4.37 %	65.59 %	30.04 %	0.01 %	0.01 %	0.01 %	0.01 %
Th	0.002	1.01 %	99.0 %	0.00 %	0.00 %		16.44 %	59.27 %	24.29 %	0.00 %	0.00 %	0.00 %	0.00 %
U	0.0	100.00 %	0.0 %	0.00 %	0.00 %		100.00 %	0.00 %	0.00 %	0.00 %	0.00 %	0.00 %	0.00 %
Cs	0.003	12.49 %	87.5 %	0.00 %	0.00 %		0.00 %	81.37 %	18.63 %	0.00 %	0.00 %	0.00 %	0.00 %
La	0.01	4.41 %	95.6 %	0.01 %	0.01 %		28.96 %	40.29 %	30.75 %	0.05 %	0.01 %	0.01 %	0.01 %
Ce	0.02	2.03 %	98.0 %	0.00 %	0.02 %		27.64 %	41.94 %	30.42 %	0.07 %	0.01 %	0.02 %	0.01 %
Ta	0.0	5.48 %	94.5 %	0.00 %	0.00 %		4.65 %	77.58 %	17.77 %	0.00 %	0.00 %	0.00 %	0.00 %
LOI													
Ga	0.002	8.59 %	91.4 %	0.00 %	0.00 %		5.57 %	65.62 %	28.81 %	0.00 %	0.00 %	0.00 %	0.00 %
Si	28.6	1.50 %	98.5 %	5.04 %	30.79 %		3.47 %	67.52 %	29.00 %	14.09 %	32.80 %	30.76 %	32.16 %
Ti	0.3	1.39 %	98.6 %	0.06 %	0.36 %		22.51 %	48.18 %	29.31 %	1.08 %	0.28 %	0.37 %	0.31 %
Cr	0.02	12.38 %	87.6 %	0.03 %	0.02 %		4.61 %	51.32 %	44.07 %	0.01 %	0.01 %	0.03 %	0.02 %
V	0.07	2.11 %	97.9 %	0.02 %	0.08 %		3.74 %	54.59 %	41.67 %	0.04 %	0.07 %	0.11 %	0.08 %
Fe	7.3	56.59 %	43.4 %	48.49 %	3.45 %		32.65 %	46.98 %	20.37 %	14.85 %	2.56 %	2.42 %	2.52 %
Mn	0.03	1.73 %	98.3 %	0.01 %	0.04 %		3.65 %	53.71 %	42.64 %	0.02 %	0.03 %	0.05 %	0.04 %
Mg	2.3	1.86 %	98.1 %	0.50 %	2.45 %		2.53 %	56.19 %	41.28 %	0.81 %	2.17 %	3.48 %	2.58 %
Ca	1.9	1.92 %	98.1 %	0.42 %	2.00 %		5.57 %	62.57 %	31.86 %	1.47 %	1.98 %	2.20 %	2.05 %
Ba	0.1	2.05 %	98.0 %	0.01 %	0.06 %		2.97 %	62.48 %	34.56 %	0.02 %	0.06 %	0.07 %	0.06 %
Leco C	0.4	8.21 %	91.8 %	0.43 %	0.44 %		6.09 %	67.23 %	26.69 %	0.35 %	0.47 %	0.41 %	0.45 %
Leco S	4.5	64.05 %	35.9 %	33.55 %	1.75 %		42.56 %	42.52 %	14.92 %	9.80 %	1.17 %	0.90 %	1.09 %
SiO2	61.3	1.49 %	98.5 %	10.79 %	65.99 %		3.48 %	67.46 %	29.05 %	30.27 %	70.24 %	66.04 %	68.92 %
TiO2	0.6	1.39 %	98.6 %	0.09 %	0.60 %		22.51 %	48.30 %	29.19 %	1.79 %	0.46 %	0.61 %	0.51 %
Al2O3	13.0	1.95 %	98.1 %	2.98 %	13.93 %		3.08 %	63.51 %	33.41 %	5.65 %	13.96 %	16.03 %	14.61 %
Cr2O3	0.03	12.37 %	87.6 %	0.04 %	0.03 %		4.41 %	51.96 %	43.63 %	0.02 %	0.02 %	0.04 %	0.03 %
V2O3	0.1	2.08 %	97.9 %	0.03 %	0.12 %		3.74 %	54.74 %	41.52 %	0.06 %	0.10 %	0.17 %	0.12 %
FeO	9.4	56.59 %	43.4 %	62.35 %	4.44 %		32.62 %	46.99 %	20.39 %	19.08 %	3.29 %	3.12 %	3.24 %
MnO	0.04	1.71 %	98.3 %	0.01 %	0.05 %		3.64 %	53.92 %	42.43 %	0.02 %	0.04 %	0.07 %	0.05 %
MgO	3.8	1.84 %	98.2 %	0.82 %	4.04 %		2.54 %	56.09 %	41.37 %	1.35 %	3.58 %	5.76 %	4.27 %
CaO	2.6	1.92 %	98.1 %	0.59 %	2.80 %		5.56 %	62.58 %	31.86 %	2.05 %	2.76 %	3.07 %	2.86 %
Rb2O	0.01	12.36 %	87.6 %	0.01 %	0.01 %		6.56 %	54.00 %	39.43 %	0.01 %	0.01 %	0.01 %	0.01 %
SrO	0.02	0.00 %	100.0 %	0.00 %	0.02 %		2.01 %	68.18 %	29.81 %	0.01 %	0.03 %	0.02 %	0.03 %
BaO	0.1	2.10 %	97.9 %	0.02 %	0.07 %		3.03 %	62.20 %	34.77 %	0.03 %	0.07 %	0.08 %	0.07 %
Na2O	2.4	2.40 %	97.6 %	0.68 %	2.57 %		4.02 %	67.94 %	28.04 %	1.36 %	2.76 %	2.48 %	2.67 %
K2O	2.4	1.45 %	98.6 %	0.41 %	2.56 %		1.94 %	62.75 %	35.31 %	0.66 %	2.54 %	3.12 %	2.72 %
ZrO2	0.0	1.83 %	98.2 %	0.01 %	0.03 %		8.74 %	57.85 %	33.41 %	0.03 %	0.02 %	0.03 %	0.03 %
P2O5	0.2	1.02 %	99.0 %	0.02 %	0.19 %		13.27 %	56.47 %	30.26 %	0.34 %	0.17 %	0.20 %	0.18 %
CO2	1.6	8.18 %	91.8 %	1.56 %	1.63 %		6.10 %	67.22 %	26.68 %	1.31 %	1.72 %	1.49 %	1.65 %
ICP_MS													
Ag	0.000	13.67 %	86.3 %	0.00 %	0.00 %		6.35 %	56.89 %	36.76 %	0.00 %	0.00 %	0.00 %	0.00 %
Al	6.92	1.40 %	98.6 %	1.14 %	7.45 %		2.89 %	64.10 %	33.01 %	2.84 %	7.54 %	8.48 %	7.83 %
As	0.001	3.22 %	96.8 %	0.00 %	0.00 %		34.69 %	41.92 %	23.39 %	0.00 %	0.00 %	0.00 %	0.00 %
Ca	1.87	2.10 %	97.9 %	0.46 %	2.00 %		5.82 %	62.82 %	31.36 %	1.53 %	1.98 %	2.16 %	2.04 %
Cd	0.002	1.01 %	99.0 %	0.00 %	0.00 %		26.50 %	42.69 %	30.81 %	0.01 %	0.00 %	0.00 %	0.00 %
Co	0.006	34.99 %	65.0 %	0.02 %	0.00 %		37.50 %	41.63 %	20.87 %	0.02 %	0.00 %	0.00 %	0.00 %
Cr	0.01	5.20 %	94.8 %	0.01 %	0.01 %		2.71 %	55.06 %	42.23 %	0.01 %	0.01 %	0.02 %	0.02 %
Cu	0.04	13.79 %	86.2 %	0.06 %	0.03 %		16.39 %	49.32 %	34.29 %	0.07 %	0.03 %	0.04 %	0.03 %
Fe	7.37	41.41 %	58.6 %	35.90 %	4.72 %		33.23 %	46.15 %	20.62 %	20.64 %	3.43 %	3.35 %	3.41 %
K	2.20	1.02 %	99.0 %	0.27 %	2.38 %		2.03 %	62.90 %	35.06 %	0.64 %	2.37 %	2.88 %	2.53 %
Li	0.003	1.06 %	98.9 %	0.00 %	0.00 %		4.22 %	58.45 %	37.32 %	0.00 %	0.00 %	0.00 %	0.00 %
Mg	1.99	0.77 %	99.2 %	0.18 %	2.16 %		2.58 %	56.29 %	41.13 %	0.73 %	1.91 %	3.05 %	2.27 %
Mn	0.05	1.04 %	99.0 %	0.01 %	0.05 %		5.01 %	54.71 %	40.28 %	0.03 %	0.04 %	0.07 %	0.05 %
Ni	0.03	63.48 %	36.5 %	0.25 %	0.01 %		34.46 %	45.22 %	20.32 %	0.06 %	0.01 %	0.01 %	0.01 %
P	0.07	1.36 %	98.6 %	0.01 %	0.07 %		15.30 %	55.24 %	29.46 %	0.14 %	0.06 %	0.07 %	0.06 %
Pb	0.003	15.31 %	84.7 %	0.01 %	0.00 %		12.93 %	55.10 %	31.97 %	0.00 %	0.00 %	0.00 %	0.00 %
S	3.29	42.60 %	57.4 %	16.51 %	2.07 %		38.91 %	43.79 %	17.30 %	10.58 %	1.43 %	1.23 %	1.37 %
Ti	0.20	0.89 %	99.1 %	0.02 %	0.22 %		3.90 %	55.74 %	40.35 %	0.11 %	0.19 %	0.31 %	0.23 %
Zn	0.18	1.05 %	99.0 %	0.02 %	0.19 %		24.39 %	43.32 %	32.29 %	0.61 %	0.13 %	0.21 %	0.16 %